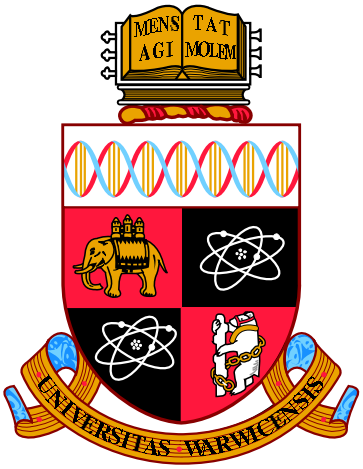

The reciprocal theorem and swimmer interactions

by

Dario Papavassiliou

Thesis

Submitted to the University of Warwick

for the degree of

Doctor of Philosophy in Physics and

Complexity Science

Department of Physics and Centre for Complexity Science

July 2016

Contents

List of Figures

Acknowledgments

It has been a pleasure and a privilege to work with Gareth Alexander, without whose enthusiasm, depth of knowledge and creativity much of this work would not have been possible. I am also grateful to Matthew Turner and Marco Polin, who have always offered encouragement and good advice.

The four years that have resulted in this thesis has been of great importance to me not only academically, but also personally, and the people who have guided and inspired me are many: Charlie, Hugo, Leo, the SOAS Rebetiko Band, and everyone else who has provided most welcome musical distractions; Tom, Davide, Mike, Pete, Ben and my other colleagues in Complexity for the entertainment; Cyril and Te-Anne for the hospitality; El for the endless supply of tea; and above all Viki for your love and company.

Finally I wish to thank my parents, Beatrice and Christos, for their unconditional support, and my siblings, Irene, Andreas and Eilidh, to whom this thesis is dedicated.

Declarations

This Thesis is submitted to the University of Warwick in support of my application for the degree of Doctor of Philosophy. I have read and understood the rules on cheating, plagiarism and appropriate referencing as outlined in my handbook and I declare that the work contained in this assignment is my own. No substantial part of the work submitted here has also been submitted by me in other assessments for this or previous degree courses, and I acknowledge that if this has been done an appropriate reduction in the mark I might otherwise have received will be made.

Work contributing to this thesis has appeared in the peer-reviewed publication:

- D. Papavassiliou & G. P. Alexander. The many-body reciprocal theorem and swimmer hydrodynamics. *Europhys. Lett.*, 110(4):44001, (2015).

Further work contained herein has been submitted for publication and is currently under review:

- D. Papavassiliou & G. P. Alexander. Exact solutions for the hydrodynamic interactions for two squirming spheres. Submitted to *J. Fluid Mech.* Pre-print: arXiv:1602.06912, (2016).

Abstract

We present a number of solutions for the hydrodynamic interaction between microscopic swimmers in a viscous fluid and confining geometries. The reciprocal theorem is adapted for this use, allowing existing solutions for Stokes drag problems to be used to calculate the motion and rotation of force-free swimmers as well as other aspects of the hydrodynamics, such as flow fields. We outline the general procedure for approximating the reciprocal theorem to calculate motion for an arbitrary slip velocity by exploiting existing solutions for point forces and point torques in Stokes flows. This is demonstrated with two examples: firstly, the commonly studied case of a swimmer in the presence of an infinite wall, where we find the reported circling of certain bacteria near a surface, and reproduce the equations of motion for a swimmer in the presence of a wall found by other means; and secondly, a calculation giving the leading contributions to the motion of a swimmer between two infinite parallel plates, representing a strongly confining geometry, and relying upon the derivation of the flow due to a point torque in this geometry, a new result. We then derive exact solutions in two and three dimensions. In two dimensions we find the equations of motion for a circular squirmer with arbitrary axisymmetric slip velocity near a plane wall or inside a circular cavity, and discuss the extension to the case of two squirmers interacting with each other, which presents some additional mathematical difficulties. In three dimensions we provide exact solutions for the axisymmetric motion of a squirming sphere close to a no-slip surface, both planar and spherical. These allow the hydrodynamic interactions of swimming microscopic organisms with confining boundaries, or each other, to be determined for arbitrary separation and, in particular, in the close proximity regime where approximate methods based on point singularity descriptions cease to be valid. We find that the circling motion of flagellated bacteria generically has opposite sense at free surfaces and at solid boundaries, as seen experimentally. By comparing these to asymptotic approximations of the interaction we find that the transition from near- to far-field behaviour occurs at a separation of about two swimmer diameters. Finally we discuss possible extensions to this work, and limitations of the approach used.

Every man should be capable of
all ideas and I understand that
in the future this will be the case

J. L. Borges

1 Introduction

Motion through a fluid is a ubiquitous phenomenon in nature, occuring at all length scales, from the largest animal to have ever lived, the blue whale, to unicellular organisms, single cells within larger organisms and sub-cellular organelles [1, 2]. However, the physics of locomotion changes dramatically with size, and the microscopic regime must be considered separately. At the small length scales we will consider here the inertial forces acting on an object moving through a fluid, whether it be a bacterium, a cell or an organelle within a cell, are negligible compared to the viscous forces; the ratio between them, known as the Reynolds number (Re), can be as low as $10^{-4} - 10^{-5}$ for small bacteria such as *Escherichia coli*, and even larger flagellates such as *Paramecium* and *Opalina* (with a length of up to 0.2mm) have Re ≈ 0.1 [3, 4]. Hence the motion is effectively time-independent; indeed, Purcell [3] estimates that a bacterium one micron long will, if it stops swimming, coast for one-hundred-thousandth of its body length before stopping as a result of viscosity. In contrast, when I swim I am able to coast for at least one body length, helping me to control my approach to the edge of the pool and avoid crashing. My Reynolds number is high, and inertia is important.

The governing equations of fluid flow in this regime are obtained by neglecting the advective term in the Navier-Stokes equations, giving the Stokes equations. For

a distribution of point forces $\boldsymbol{f}$ the flow $\boldsymbol{u}$ and pressure p at a point $\boldsymbol{x}$ must satisfy

$$-\boldsymbol{\nabla} p(\boldsymbol{x}) + \mu \nabla^2 \boldsymbol{u}(\boldsymbol{x}) + \boldsymbol{f} \equiv \boldsymbol{\nabla} \cdot \boldsymbol{\sigma} + \boldsymbol{f} = \boldsymbol{0}, \tag{1.1}$$

where μ is the viscosity and $\boldsymbol{\sigma}$ is the stress tensor, defined as

$$\boldsymbol{\sigma} = -p\, \boldsymbol{I} + \mu(\boldsymbol{\nabla u} + (\boldsymbol{\nabla u})^T). \tag{1.2}$$

If the fluid is incompressible, the flow must also satisfy the continuity equation,

$$\boldsymbol{\nabla} \cdot \boldsymbol{u} = 0. \tag{1.3}$$

The time-independence of viscous flows was vividly demonstrated by Taylor [5]. A drop of dye suspended in glycerine between two concentric cylinders was stirred four times clockwise. When subsequently stirred four revolutions anticlockwise the smeared-out dye returned to a concentrated drop. The time-independence of low Reynolds number flows has important consequences for swimming, since it means that any propulsive stroke must be non-reciprocal in time. This phenomenon has entered the active-matter jargon as the 'scallop theorem' after its most celebrated victim, a single-hinged scallop which over the course of one open-and-close cycle returns exactly to its starting place [3]. Note, however, that the scallop theorem may be overcome by breaking spatial symmetry, allowing otherwise immobile organisms to swim in the presence of surfaces, boundaries or other swimmers [6–8]. A formalisation of the calculation of propulsion as a result of a sequence of shapes was given by Shapere and Wilczek [9], and used to calculate the swimming efficiency of a number of swimming strategies [10].

A natural question to ask is how to optimise swimming with respect to energetic cost. The time-independence of Stokes flows means the theoretical optimal swimming strategy is a 'treadmilling' of material on the swimmer's surface [11, 12], having a maximum energetic efficiency of 50% [13]. In effect the boundary is kept stationary with respect to the surrounding fluid while the swimmer's interior slides forward, somewhat like a sausage being squeezed out of its casing. This is similar to the amoeboid movement widely seen in eukaryotic cells, from protist organisms such as *Euglena* [14] to cells in higher organisms such as human leukocytes and in tumour cells, contributing to the rapid metastasis of sarcomas [15]. In lower orders of life propulsion by flagella is common (although there exist creatures in between: the protist *Naegleria gruberi* has in its life cycle both an amoeboid stage and a flagellated stage [16]). Bacteria such as *Escherichia* and *Vibrio* overcome the lim-

itations of high viscosity by rotating flagella in a corkscrew-type motion [17]. The alga *Chlamydomonas* possesses a pair of flagella which it beats in an oar-like fashion to pull itself through a fluid; time asymmetry here is achieved by flexibility of the flagella causing the power stroke and rest stroke to assume different shapes [18]. Other organisms still, such as *Paramecium* and *Opalina*, are covered by a 'carpet' of flagella of very short length compared to their body size, which through hydrodynamics synchronise their beating [19] to achieve a stroke very close to the theoretical optimum [20], despite only $\sim 1\%$ energetic efficiency. Due to its central role in locomotion flagellar beating was one of the earliest active propulsion problems to be studied in depth [21–23], and continues to be a central problem in the field [24–27].

Recent years have seen a proliferation of methods for producing artificial self-propelled particles or swimmers with a variety of propulsion mechanisms, including explicitly mechanical, floating swimmers powered by rolling cylinders [28] or colloidal beads propelled by magnetically-controlled waving tails [29], and more commonly exploiting surface processes which generate flows in response to gradients of some externally imposed or self-generated field [30] of chemical concentration [31, 32], electric potential [33, 34] or temperature [35]. These *phoretic* processes enable miniaturisation, allowing for experiments with a great number of interacting particles [36, 37]. There is hope that these biomimetic swimmers may fulfil a number of nanotechnological and medical roles.

Swimming microorganisms do not live in an infinite, unbounded fluid domain, but instead inhabit complex geometries confined by fluid interfaces and solid boundaries, and populated by other organisms and passive particles. Much, if not most, of the rich variety of behaviour that is seen [1, 38] cannot be explained outside of the context of confinement. The most basic interaction is of a single swimmer with a boundary or object; even in such cases we see striking behaviour, such as the 'waltzing' of a pair of *Volvox* colonies [39]. Flagellated bacteria are known to trace out circles [40–42] near solid boundaries and, remarkably, if the boundary is replaced by a free surface the direction of rotation changes [43, 44]. An important effect is the attraction of swimmers to boundaries, noted by Rothschild [45] for bull spermatozoa but subsequently also seen in bacteria [46, 47], which is thought to contribute to the navigation of sperm cells in the female reproductive system [48] and plays a fundamental role in biofilm formation at surfaces [49]. Swimmers adhere to surfaces due to strong lubrication forces, causing catalytic self-propelled rods to orbit colloidal spheres [50] and the microalga *Chlamydomonas reinhardtii* to orbit cylindrical posts until flagellar beating detaches it [51]. As the number of interacting components increases so does the complexity of the behaviour, resulting in the phase

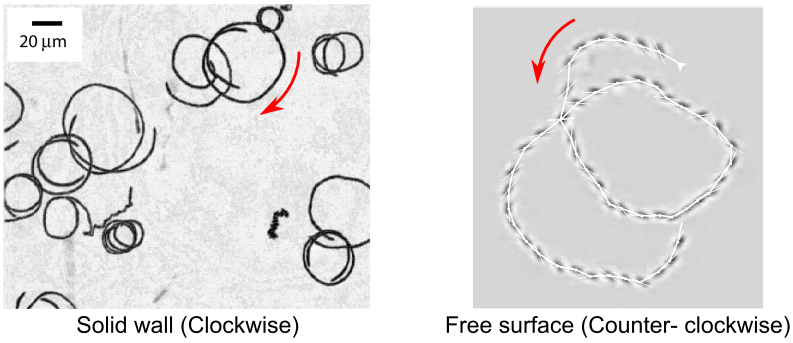

Figure 1.1: Circling of *Escherichia coli* near a solid and free boundary. Reproduced from reference [4].

behaviours seen in dense suspensions of bacteria, including long-range orientational order [52], and the formation of large-scale turbulent structures [53, 54] and stable spiral vortices [55]. The latter can only occur in confinement. An understanding of these phenomena is important for the design of microfluidic systems, such as devices to direct swimmers [48, 56] and harness them for mass transport [57, 58], and to extract mechanical work from their activity [59].

The interaction of swimming microorganisms with each other and their environment is a complex combination of several factors, including biology, such as the taxis which allows them to move in search of food and tolerable living conditions, and to aggregate and form patterns through chemical signalling and quorum sensing [60, 61]; and hydrodynamics and physical contact. It has been shown that the scattering of swimmers from planes [62] and posts [51] arises from physical contact of the flagellae with the surface, so that hydrodynamics is not the dominant contributor to the phenomena in these cases. Nonetheless, the fact that there is physical contact with the surface emphasises that any hydrodynamic effects have to be considered in this contact regime. Other cases are less clear-cut; for instance, the typical density profile of a suspension of swimmers close to a wall has been reproduced both by considering hydrodynamics [47] and Brownian motion combined with collisions [63].

Here we look only at the effect of hydrodynamics on interactions. The simplest mathematical models use point-singularity approximations, and in particular to treat swimmers as force dipoles, since this is the slowest-decaying flow field that a moving force-free object may produce [38]. Nevertheless this characterisation is enough to reproduce the attraction to walls seen in several real organisms [47, 64, 65]. Including faster-decaying singularities additional effects may be explained, in par-

ticular the rotation of flagellated bacteria near solid boundaries [43, 66] and free surfaces [4, 44], shown in fig. 1.1. The sign of a swimmer's dipole moment relative to its swimming direction characterises it as *extensile* or *contractile*, referring to whether it expels or draws fluid along its head-tail axis. The behaviour of extensile and contractive swimmers was studied in some depth by Ishikawa et al. [67], who found the far-field interactions by considering multipole expansions of stresslets, and the near-contact interactions using lubrication theory. Also relevant to microscopic swimming is slender-body theory [68, 69] which is commonly used to model the flows generated by beating flagella [25, 70]. Point-singularity approximations have been used to contruct continuum models describing behaviour of suspensions [1], by extension to standard models of liquid crystal hydrodynamics [71] or 'boids' [72]. These models predict distinct behaviour for extensile and contractile matter, with the nematic phase being stable in the former and unstable in the latter as a result of activity [73, 74].

The short-ranged nature of the flows associated to swimming [21] means the near-field interactions are particularly important, and so exact solutions to the Stokes equations are desirable. In the case of a single swimmer in an unbounded domain several such solutions exist, notably for the motion of a single axisymmetric squirmer [75, 76], later generalised to non-axisymmetric slip velocities [77], and for the motion of a 'treadmilling' spheroidal [11] or toroidal swimmer [3, 12, 22], as well as a two-dimensional analogue for a squirming cylinder [78]. The squirmer solutions have been used to find the advection of tracer particles by a passing swimmer [79], and the capture of swimmers into orbits by spherical obstacles [80]. Dropping instead to two dimensions a number of additional solutions in confinement become available using conformal mapping techniques, such as the motion of an active cylinder near a planar or concave boundary [66, 81, 82], or under a free surface [83].

The approach followed in this thesis will be to specify a *slip velocity* on the surface of a swimmer, which shall usually be taken to be spherical (or circular in two dimensions). Slip velocity has several interpretations. Lighthill [75] and Blake [76] refer to a 'boundary envelope' on the surface of an organism covered in a carpet of flagellae, which propagates as a metachronal wave, as seen in *Paramecium* and *Opalina*. Therefore the slip velocity refers to the local speed of deformation of an effective boundary. Slip velocity has a very different physical interpretation in the case of artificial particles propelled by phoretic mechanisms [30]. The typical strategy in solving for the motion is to separate the fluid dynamics into an inner solution inside a thin boundary layer, determined by the range of the interaction of the phoretic process, and an outer solution [84, 85]. The slip velocity is the boundary

condition for solving the outer problem, while the inner problem is usually taken to be non-slip.

The slip-velocity approach can only be approximate, particularly near the limit of physical contact with another object. To give a concrete example, a helical flagellum spins as a result of a torque exerted upon it by a molecular motor. Since the resistance to motion in general will change near a boundary, the rotation sustained by the constant torque generated by the flagellar motor will also change. Hence more accurately we should specify a stress distribution on the surface, as done computationally in boundary-element simulations [86, 87]. Nevertheless the computational tractability of Dirichlet boundary conditions means using a slip velocity is a valuable mathematical model.

This thesis is structured as follows. In Chapter 2 we present the Lorentz reciprocal theorem [88] in a form which enables the calculation of the hydrodynamics of interactions, represents the key methodology of this study. While this is a minor extension to previous work [89] the possibilities it offers for calculation of swimmer interactions appears under-explored in the literature. We then present the mathematical models of swimming used herein, particularly the squirmer model of Lighthill [75] and Blake [76, 78]. The following chapters demonstrate different applications of the reciprocal theorem to swimmer problems. Chapter 3 shows how simple singularity solutions to the Stokes equations may be used to develop versatile approximate models in a variety of geometries and for a variety of swimmer shapes and swimming strategies, and gives as explicit examples a spherical squirmer interacting with a passive and active wall, and a squirmer in the channel between two plates. Chapter 4 demonstrates exact results for interactions in two dimensions, obtained using conformal mapping techniques. These compare with the approximate results found previously to good qualitative agreement. Chapter 5 is concerned with exact solutions in three dimensions. While these solutions are incomplete, giving only the axisymmetric components of motion, they give valuable information about the near-field behaviour missing from the approximate models of Chapter 3. Finally in Chapter 6 we discuss possible extensions to this work, while assessing the limitations of the approach used.

2

The reciprocal theorem and swimmer hydrodynamics

2.1 The Lorentz reciprocal theorem

Any two solutions of the Stokes equations, say $(\boldsymbol{u}, p, \boldsymbol{\sigma})$ and $(\tilde{\boldsymbol{u}}, \tilde{p}, \tilde{\boldsymbol{\sigma}})$, in the same fluid region S with boundary ∂S and outward normal $\hat{\boldsymbol{n}}$ are related by the Lorentz reciprocal theorem [88, 90–92],

$$\int_{\partial S} \boldsymbol{u} \cdot \tilde{\boldsymbol{\sigma}} \cdot \hat{\boldsymbol{n}} = \int_{\partial S} \tilde{\boldsymbol{u}} \cdot \boldsymbol{\sigma} \cdot \hat{\boldsymbol{n}}. \tag{2.1}$$

Eq. (2.1) is an invaluable tool in fluid mechanics (and linear elasticity, which is governed by similar equations [93]), since it allows the boundary conditions of an unknown problem to be transformed to those of a conjugate problem to which a solution is known; for instance, it has been used to derive Faxén's laws [92] and formulate the boundary element method [91], and to prove that the resistance and mobility matrices of objects in Stokes flow must be symmetric [88].

Eq. (2.1) follows directly from the Stokes equations: consider two stress tensors $\boldsymbol{\sigma}$ and $\tilde{\boldsymbol{\sigma}}$, defined as in eq. (1.2). Contracting these against each other gives

$$\sigma_{ij}\tilde{\sigma}_{ij} = -\tilde{p}\,\mathrm{Tr}\boldsymbol{\sigma} + 2\mu\sigma_{ij}\partial_i\tilde{u}_j = -p\,\mathrm{Tr}\tilde{\boldsymbol{\sigma}} + 2\mu\tilde{\sigma}_{ij}\partial_i u_j, \tag{2.2}$$

where Einstein notation has been assumed. Then, since $\mathrm{Tr}\boldsymbol{\sigma} = -3p$ and $\mathrm{Tr}\tilde{\boldsymbol{\sigma}} = -3\tilde{p}$, the flows are related by the identity

$$\sigma_{ij}\partial_i\tilde{u}_j = \tilde{\sigma}_{ij}\partial_i u_j. \tag{2.3}$$

Now integrating by parts over S gives

$$\int_S \sigma_{ij}\partial_i\tilde{u}_j \mathrm{d}V = \int_S \tilde{\sigma}_{ij}\partial_i u_j \mathrm{d}V \implies \int_S \partial_i(\sigma_{ij}\tilde{u}_j)\mathrm{d}V = \int_S \partial_i(\tilde{\sigma}_{ij}u_j)\mathrm{d}V. \tag{2.4}$$

The omitted term on the right-hand side, which involves the divergence of the stress, vanishes point-wise in the fluid domain as the Stokes equations, (1.1), are assumed to hold there. Finally, the Stokes theorem converts the volume integrals to integrals over the boundary of the fluid to give eq. (2.1).

An elegant application of the reciprocal theorem is to the determination of swimmer motion. Swimmer problems have complicated boundary conditions, which can vary greatly between different types of organisms [38] and active particles [30], both in the mechanisms by which propulsion is achieved and in the local hydrodynamics generated. As first recognised by Stone and Samuel [89], the reciprocal theorem provides a route to bypass explicit solution of the Stokes equations in these cases by instead solving the Stokes equations for a conjugate problem, the Stokes drag with force $\tilde{\boldsymbol{F}}$ and torque $\tilde{\boldsymbol{T}}$ on a no-slip object of the same shape as the swimmer. The translational and rotational speeds $\boldsymbol{U}$ and $\boldsymbol{\Omega}$ are extracted from an arbitrary slip velocity $\boldsymbol{u}_s$ by the relation

$$\boldsymbol{U}\cdot\tilde{\boldsymbol{F}} + \boldsymbol{\Omega}\cdot\tilde{\boldsymbol{T}} = -\int_{\partial S} \boldsymbol{u}_s\cdot\tilde{\boldsymbol{\sigma}}\cdot\hat{\boldsymbol{n}}. \tag{2.5}$$

The integration kernel, $\tilde{\boldsymbol{\sigma}}\cdot\hat{\boldsymbol{n}}$, is the force per unit area on the boundaries of the fluid in the conjugate problem.

For a single sedimenting sphere the stress tensor is constant, so the integration kernel in eq. (2.5) is proportional to the drag force. This means that for a single spherical microorganism this calculation is particularly simple: using the reciprocal theorem, Stone and Samuel [89] found that the propulsion speed is just the slip velocity averaged over the organism, and the rotational speed is the averaged tangential slip velocity; explicitly,

$$\boldsymbol{U} = -\frac{1}{4\pi}\int_0^{2\pi}\mathrm{d}\phi_s\int_0^{\pi}\sin\theta_s\mathrm{d}\theta_s\,\boldsymbol{u}_s, \tag{2.6}$$

$$\boldsymbol{\Omega} = -\frac{3}{8\pi a}\int_0^{2\pi}\mathrm{d}\phi_s\int_0^{\pi}\sin\theta_s\mathrm{d}\theta_s\,\boldsymbol{s}_r\times\boldsymbol{u}_s, \tag{2.7}$$

where $\boldsymbol{s}_r$ is the outward normal to the sphere and (θ_s, ϕ_s) are the surface coordinates on the sphere. Where the swimming stroke has a periodic dependence on time the expressions (2.6) and (2.7) may be further averaged over one cycle to give the average swimming speed.

Eqs. (2.6) and (2.7) suggest a decomposition of a general $\boldsymbol{u}_s$ in spherical harmonics; the reciprocal theorem then identifies the propulsive contributions of slip velocity. In particular it is immediate that self-propulsion can only result from slip velocity components symmetric about the direction of travel, justifying the common practice (continued here) of considering axisymmetric slip velocity profiles.

The simplicity of this calculation means it has become a standard tool in the active matter literature [38, 94–96], although in this particular case of a spherical swimmer Lamb's general solution [97] of the Stokes equations exterior to a sphere allows direct calculation of the swimming speed, giving additionally the full flow field. Indeed, the swimming speed found for an active sphere self-propelling by means of a metachronal wave on its surface by Stone and Samuel [89], given as an illustrative example of this use of the reciprocal theorem, had been derived by other means at around the same time by Ehlers et al. [98].

Perhaps slightly surprisingly, the reciprocal theorem also finds use in two dimensions [81, 94, 99]. This is suprising because the conjugate solution is ill defined – the celebrated Stokes paradox [100]. Nevertheless, the reciprocal theorem depends only on the stress tensor, which decays sufficiently fast for eq. (2.5) to be well-defined. Furthermore, since swimmer problems are force- and torque-free [22] a physically realistic solution exists [78]. For a single active disc the two-dimensional analogues of Stone and Samuel's formulae, eq. (2.6) and (2.7), are

$$\boldsymbol{U} = -\frac{1}{2\pi}\oint_{r=a} \mathrm{d}\theta\, \boldsymbol{u}_s, \qquad \Omega = -\frac{1}{2\pi a}\oint_{r=a} \mathrm{d}\theta\, \boldsymbol{s}_\theta \cdot \boldsymbol{u}_s, \tag{2.8}$$

where $\boldsymbol{s}_\theta$ is the unit tangent to the disc; these expressions can be seen to have the same structure as eqs. (2.6) and (2.7).

More recently there have been interesting extensions of the reciprocal theorem and other related integral theorems to cases where direct solutions are not so readily available, such as propulsion by the Marangoni effect [101], self-propulsion through viscoelastic and non-Newtonian fluids [102], motion of catalytic colloidal dimers [103, 104], and active pumping in a channel [105].

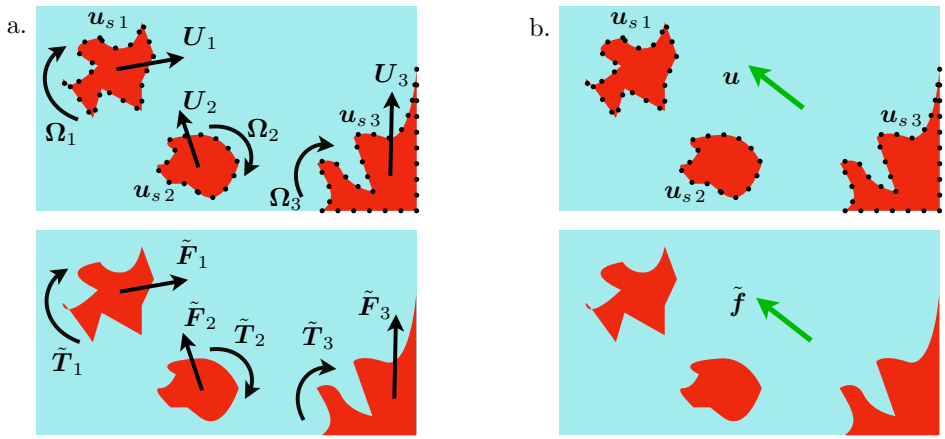

Figure 2.1: A cartoon representation of the many-body reciprocal theorem. The stress tensor from a known conjugate solution (bottom) allows the swimmer problem in the same geometry (top) to be examined. (a) Translation $\boldsymbol{U}_i$ and rotation $\boldsymbol{\Omega}_i$ of swimmers driven by slip velocities $\boldsymbol{u}_{i\,s}$ by relation to Stokes drag on no-slip objects of the same shape. (b) Flow $\boldsymbol{u}$ and vorticity $\boldsymbol{\omega}$ found with point-force and point-torque as the conjugate solution.

2.2 The reciprocal theorem and interactions

The reciprocal theorem is immediately applicable to find the motion of swimmers in the presence of boundaries or other swimmers [66]. As the classic form of the reciprocal theorem, eq. (2.1), does not specify the shape of the fluid boundary, the boundary my be taken to be composed of several disjoint components. If the boundary elements are labelled by an index i, so that $\partial S = \bigcup_i \partial S_i$, then eq. (2.5) takes the form

$$\sum_i \left[\boldsymbol{U}_i \cdot \tilde{\boldsymbol{F}}_i + \boldsymbol{\Omega}_i \cdot \tilde{\boldsymbol{T}}_i \right] = -\sum_i \int_{\partial S_i} \boldsymbol{u}_{s\,i} \cdot \tilde{\boldsymbol{\sigma}} \cdot \hat{\boldsymbol{n}}, \tag{2.9}$$

where $\boldsymbol{u}_{s\,i}$ are the slip velocities of each of the swimmers. This is illustrated schematically in fig. 2.1.

Eq. (2.9) is enormously general and allows essentially any aspect of swimmer hydrodynamics to be calculated. To isolate the motion or rotation of any one swimmer the linearity of the Stokes equations permits the use of a conjugate solution with a force or torque acting on the corresponding passive object, with all other objects force- and torque-free.

As the size of the measured object is shrunk to zero we find that the reciprocal theorem may be used to find flow fields, $\boldsymbol{u}(\boldsymbol{x})$. The object may be thought of as a

tracer particle which samples the fluid velocity. Explicitly,

$$\boldsymbol{u}(\boldsymbol{x}) \cdot \tilde{\boldsymbol{f}}(\boldsymbol{x}) = -\sum_i \int_{\partial S_i} \boldsymbol{u}_{s\,i} \cdot \tilde{\boldsymbol{\sigma}} \cdot \hat{\boldsymbol{n}}, \tag{2.10}$$

where in the conjugate solution the stress tensor $\tilde{\boldsymbol{\sigma}}$ corresponds to a point force $\tilde{\boldsymbol{f}}(\boldsymbol{x})$ at $\boldsymbol{x}$, in the fluid exterior to the no-slip objects with boundaries ∂S_i. The vorticity is then the curl of the flow, but may also be found analogously to eq. (2.10) using a conjugate solution for a point torque $\tilde{\boldsymbol{\tau}}(\boldsymbol{x})$. Eq. (2.10) is reminiscent of the boundary-element method [91], with the conjugate stress tensor acting as the double-layer potential and the slip velocity specifying the stress distribution over the swimmer's surface. The single-layer potential is zero because the swimmer is force-free.

The central object in application of the reciprocal theorem is the stress tensor from the conjugate solution, and if this is known for a particular geometry the motion due to any slip velocity may be found. This is in contrast to direct calculations of swimming speed, where a particular slip velocity is taken to be a boundary condition for solution of the Stokes equations, and must be solved for explicitly. A stress tensor corresponding to a force extracts translational motion, and one corresponding to a torque extracts rotation; if this force-torque pair act on a no-slip immersed object, the reciprocal theorem finds the motion of a swimmer of the same shape given some slip velocity, while if the force-torque pair is in the fluid region the reciprocal theorem gives the flow at that point.

The reciprocal theorem as we have presented it has been independently noted by Elfring and Lauga [106]. Although it is only a mild extension of the original application, its capabilities in solving swimmer problems exactly have been little explored in the literature. One exception is the work of Crowdy, who has found the motion in two dimensions of squirming [81] and self-diffusiophoretic discs close to walls [82], using as a conjugate solution the Stokes drag on a cylinder in the half-space [107].

2.2.1 Exact and approximate solutions using the reciprocal theorem

While conceptually the use of the reciprocal theorem is straightforward, it is contingent on having an explicit conjugate solution available and in practice the number of exact solutions to Stokes drag is small, particularly for flows about multiple objects or in non-trivial geometries. For single objects, as well as the sphere mentioned before, there are solutions available for certain solids of revolution, such as tori [108–110], spherical caps and lenses [111, 112], which could prove useful for modelling novel microswimmers (see, for instance, the 'smoke ring' swimmer hy-

pothesised by Taylor [22] and Purcell [3] and studied in detail by Leshansky and Kenneth [12]). In Chapter 5 we will investigate Stimson & Jeffery's classic solution for the axisymmetric translation of a pair of spheres [113], together with the analogous axisymmetric rotation [114] and with some discussion of behaviour near a free surface [115]. Unfortunately no exact solution for non-axisymmetric translation or rotation is yet available for this geometry [116]. In two dimensions, however, all components of motion of two discs to be found [107, 117, 118], as will be shown in Chapter 4. Furthermore the availability of conformal maps means the solution for two discs may, in principle, be transformed to that for any doubly-connected domain [119], meaning the solutions for a great variety of two-body interactions come within reach.

Greater progress is possible if the reciprocal theorem is used in an approximate sense. Since the leading contribution to the stress due to the dragging on any object is that due to a point force, an appropriate singularity solution may be used as a conjugate solution for use with eq. (2.9) [66]. Such solutions exist for a number of physically relevant confined geometries. In Chapter 3 we will demonstrate as explicit examples the motion near a wall [120] and between two parallel plates [121]. Other available solutions include those for a point force near a fluid-fluid interface [122, 123], which has as a limit a free surface and could help understand processes such as biofilm formation [49]; outside a sphere [70], where artificial microswimmers have been observed to become trapped in orbits [50]; or inside a pipe [124], with particular applicability to modelling somatic processes such as clearing of mucus from the lungs [125] or transport of the ovum in the female reproductive tract [126].

This approach is distinct from but complementary to other approximate solutions of swimmer problems, which model activity by some combination of flow singularities and calculate interactions by means of truncated multipole expansions [65, 67, 127–129]. Davis and Crowdy [129] explicitly calculate the interaction of a swimmer with a wall using both matched asymptotics and the reciprocal theorem with an approximated stress tensor, obtaining the same dynamics and concluding that the latter approach is computationally unwieldy for the calculation of interactions.

Both the reciprocal theorem and truncated multipole expansions rely on having a solution for the flow due to a point force in a given geometry. For the reciprocal theorem this is used to calculate a stress tensor. This then allows the motion due to any slip velocity to be calculated. In a multipole expansion explicit reflections of this point force must be calculated to order depending on the desired

accuracy of the expansion. We take the view that the reciprocal theorem is a versatile tool that provides a straightforward way to adapt the variety of Stokes drag problems to swimmer problems without restricting the boundary conditions; the flexibility in specification of the slip velocity compensates for the inability to resolve flow fields at the same time as finding swimmer motion.

2.3 Swimmer hydrodynamics

We now outline some hydrodynamic models of swimming that will be used in the remainder of this thesis. First we record the singularities of viscous flow which form the basis of asymptotic descriptions or swimmers, and describe a common categorisation of swimmers by their asymptotic flow fields. Then we present the squirmer model of Lighthill [75] which, in the fully generalised form given by Pak and Lauga [77], allows any slip velocity on a spherical or circular swimmer to be written down.

2.3.1 Flow singularities

Since the Stokes equations are linear, solutions may be constructed using the Green's function, also known as the Stokeslet ("for want of a better word" – Hancock [23]), which gives the flow at $\boldsymbol{x}$ due to a point force $\boldsymbol{f}$ of unit strength located at $\boldsymbol{y}$ as

$$\boldsymbol{u}^{\mathrm{Sto}}(\boldsymbol{r};\boldsymbol{f}) = \frac{1}{8\pi\mu}\left[\frac{\boldsymbol{f}}{|\boldsymbol{r}|} + \frac{(\boldsymbol{f}\cdot\boldsymbol{r})\boldsymbol{r}}{|\boldsymbol{r}|^3}\right], \qquad p^{\mathrm{Sto}}(\boldsymbol{r};\boldsymbol{f}) = \frac{\boldsymbol{f}\cdot\boldsymbol{r}}{4\pi|\boldsymbol{r}|^3}, \tag{2.11}$$

where $\boldsymbol{r} \equiv \boldsymbol{x} - \boldsymbol{y}$. A simple example in which the Stokeslet may be used in swimmer problems is given by *Chlamydomonas*, which propels itself by beating a pair of flagella. A very good agreement to the flow field was obtained by Drescher et al. [130], reproduced in fig. 2.2(a)-(b), by imposing two equal Stokeslets acting backwards at the flagella, plus a single Stokeslet in the centre of the body representing the reaction force exerted by the fluid, so that the total force is zero.

Any derivative of eq. (2.11) is also a solution of the Stokes equations. For instance the Stokes-doublet, or force dipole, is the first spatial derivative of the Stokeslet, and is equivalent to a pair of equal and opposite forces in the limit of diverging strength and vanishing separation. While the Stokeslet is quantified by a single unit vector representing the direction of the force, the Stokes-doublet is quantified by two unit vectors representing the direction of the force and the direction of the gradient of the Stokeslet; equally, higher-order derivatives (called the quadrupole, octupole etc. by analogy to potential theory) are quantified by three,

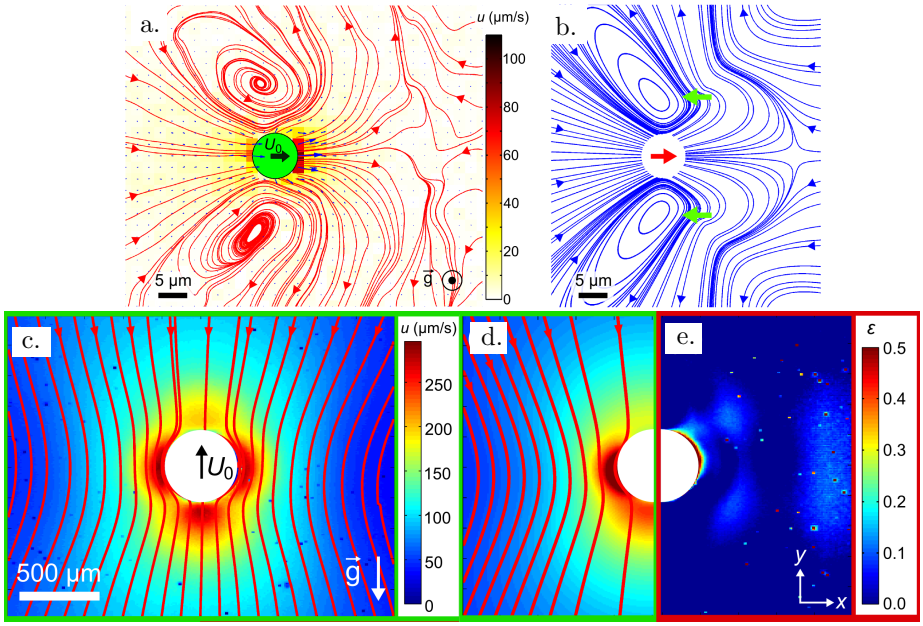

Figure 2.2: Point-singularity models of swimming microorganisms compared to measured flow fields, reproduced from reference [130]. (a) Time-averaged flow field of *Chlamydomonas reinhardtii*. (b) Three-Stokeslet model of *Chlamydomonas reinhardtii*. (c) Time-averaged flow-field of *Volvox carteri*. (d) Model of *Volvox carteri* using Stokeslet, stresslet and source-dipole. (e) Error of model compared to measurement.

four and so on unit vectors. Hence, the Stokes-doublet is given by

$$\boldsymbol{u}^{\mathrm{SD}}(\boldsymbol{r};\boldsymbol{f},\boldsymbol{g}) = -\boldsymbol{g}\cdot\boldsymbol{\nabla}(\boldsymbol{u}^{\mathrm{Sto}}(\boldsymbol{r};\boldsymbol{f})), \qquad p^{\mathrm{SD}}(\boldsymbol{r};\boldsymbol{f},\boldsymbol{g}) = -\boldsymbol{g}\cdot\boldsymbol{\nabla}(p^{\mathrm{Sto}}(\boldsymbol{r};\boldsymbol{f})), \quad (2.12)$$

borrowing notation from Chwang and Wu [131]. A more intuitive physical interpretation of the flow associated with the Stokes-doublet is given by separating it into its symmetric and antisymmetric components (under interchange of $\boldsymbol{f}$ and $\boldsymbol{g}$). The latter is called the rotlet, with a flow field

$$\boldsymbol{u}^{\mathrm{Rot}}(\boldsymbol{r};\boldsymbol{\tau}) = \frac{1}{8\pi\mu}\frac{\boldsymbol{\tau}\times\boldsymbol{r}}{|\boldsymbol{r}|^3}, \qquad p^{\mathrm{Rot}}(\boldsymbol{x};\boldsymbol{\tau}) = 0, \qquad \boldsymbol{\tau} \equiv \boldsymbol{f}\times\boldsymbol{g}. \quad (2.13)$$

The vector strength $\boldsymbol{\tau}$ should be interpreted as a point torque, since the torque on any volume containing $\boldsymbol{y}$ is $\boldsymbol{\tau}$. The symmetric component of the Stokes-doublet is

called the stresslet, with a flow field

$$\boldsymbol{u}^{\mathrm{Str}}(\boldsymbol{r};\boldsymbol{f},\boldsymbol{g}) = \frac{1}{8\pi\mu}\left[-\frac{\boldsymbol{f}\cdot\boldsymbol{g}}{|\boldsymbol{r}|^3} + 3\frac{(\boldsymbol{f}\cdot\boldsymbol{r})(\boldsymbol{g}\cdot\boldsymbol{r})}{|\boldsymbol{r}|^5}\right]\boldsymbol{r}$$
$$p^{\mathrm{Str}}(\boldsymbol{r};\boldsymbol{f},\boldsymbol{g}) = \frac{1}{4\pi}\left[-\frac{\boldsymbol{f}\cdot\boldsymbol{g}}{|\boldsymbol{r}|^3} + 3\frac{(\boldsymbol{f}\cdot\boldsymbol{r})(\boldsymbol{g}\cdot\boldsymbol{r})}{|\boldsymbol{r}|^5}\right]. \tag{2.14}$$

The stresslet gives the leading-order flow of a force-free object and plays an important role in the method of reflection used to calculated disturbance flows [92]. A slightly different definition of the stresslet is used by Batchelor [132] and Spagnolie and Lauga [65], who remove the first term in the flow.

Finally, additional fundamental solutions to the Stokes equations are given by the solutions of

$$\nabla^2\boldsymbol{u} = \boldsymbol{0}, \tag{2.15}$$

corresponding to flows with constant pressure (without loss of generality taken to be zero) and zero forces [65]. The source, representing injection of fluid at $\boldsymbol{y}$ with rate 1, has the flow field

$$\boldsymbol{u}^{\mathrm{Sou}}(\boldsymbol{r}) = \frac{1}{4\pi}\frac{\boldsymbol{r}}{|\boldsymbol{r}|^3}; \tag{2.16}$$

while the source dipole (or potential doublet) is derived from this is in the same way as the Stokes doublet, with a flow

$$\boldsymbol{u}^{\mathrm{PD}}(\boldsymbol{r};\boldsymbol{g}) = \frac{1}{4\pi}\left[-\frac{\boldsymbol{g}}{|\boldsymbol{r}|^3} + 3\frac{(\boldsymbol{g}\cdot\boldsymbol{r})\boldsymbol{r}}{|\boldsymbol{r}|^5}\right] \tag{2.17}$$

Chwang and Wu [131] noted that the source dipole is related to the Stokeslet by

$$\boldsymbol{u}^{\mathrm{PD}}(\boldsymbol{r};\boldsymbol{g}) = -\mu\nabla^2\boldsymbol{u}^{\mathrm{Sto}}(\boldsymbol{r};\boldsymbol{g}), \tag{2.18}$$

and therefore any source-free flow may be described solely in terms of Stokeslets and their derivatives. We shall only use swimmer models with constant volume, at least in a time-averaged sense, although introduction of sources and sinks allows modelling of organisms such as *Euglena*, which self-propels by exchanging material between its head and tail [14].

2.3.2 Pushers and pullers

The absence of external forces on a self-propelled swimmer mean that any forces exerted on the fluid are balanced by an opposite body force. Thus the most slowly decaying contribution to the flow that a swimmer may exhibit is the stresslet,

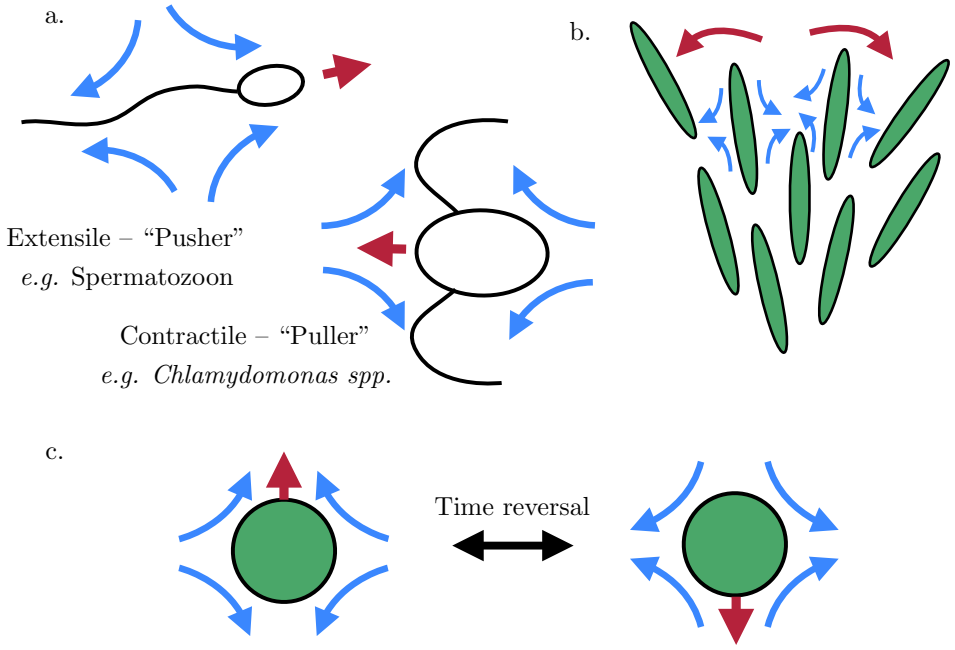

Figure 2.3: (a) Extensile and contractile swimmers as force dipoles with opposite sign. (b) The splay instability in contractile active liquid crystals [73]. (c) Under time-reversal extensile swimmers map to contractile swimmers swimming in the opposite direction.

eq. (2.14), going as r^{-2}, which dominate asymptotic behaviour and far-field interactions. However a stresslet is head-tail symmetric and cannot be motile; the lowest-order self-propulsive, force-free flow singularity is the source dipole, eq. (2.17), which goes as r^{-3}. It is common to model swimmers using just these singularities, to account for the observations that they self-propel and have a far-field straining flow which decays as the inverse distance squared. *Volvox carteri*, which is approximately spherical, is described very well even at small distances by a model composed of a Stokeslet corresponding to gravity, of non-negligible strength despite a very small excess buoyancy, and a stresslet and source dipole describing the swimming [130], as shown in fig. 2.2(c)-(e).

The relative sign of the stresslet compared to the source dipole characterises a swimmer as extensile (*pusher* in the commonly-used jargon), meaning fluid is expelled along the orientation axis and drawn in on the equator, or contractile (*puller*), drawing in fluid along the orientation axis; a cartoon picture of these is shown in fig. 2.3(a). Most prokaryotes, such as flagellated bacteria, and swimming cells such as spermatozoa are pushers, while pullers tend to be higher organisms such

as the flagellated alga *Chlamydomonas*. The change of sense of local flow around pushers and pullers means interactions with geometry and other swimmers can be very different for each [105].

2.4 The squirmer model

Possibly the earliest mathematical model of a microscopic swimming mechanism was G.I. Taylor's waving sheet [21]. The following year James Lighthill (incidentally, a keen open-water swimmer) published his squirmer model [75], based on Lamb's classic solution of the Stokes equations outside a sphere [97], and gives a decomposition of flow on the surface of a sphere in Legendre polynomials. In the original formulation only axisymmetric tangential and radial components of slip velocity were considered, allowing the use of a Stokes streamfunction to solve the problem. A typographical error in Lighthill's manuscript was infamously later corrected by his student, John Blake [76].

The inclusion of 'swirling modes', or azimuthal flow with axisymmetric patterning [66], is straightforward since axisymmetric, azimuthal flows satisfy Laplace's equation [114]; these have been used to model *Volvox*, which rotates about its swimming axis [133]. A full non-axisymmetric generalisation of the squirmer model was, despite the availability of Lamb's solution, only published in 2014 by Pak and Lauga [77]. The flow about a squirmer in non-zero Reynolds number has even more recently been investigated numerically, finding that pushing strokes are stable up to Reynolds numbers ~ 1000 while pulling strokes trap vorticity in the wake of the swimmer which breaks up the flow and causes high inefficiency in swimming [134].

The axisymmetric slip velocity, including swirling components, is expressed in terms of radial, meridional and azimuthal squirming modes, A_l, B_l and C_l. In a spherical basis $\{\boldsymbol{s}_r, \boldsymbol{s}_\theta, \boldsymbol{s}_\phi\}$ centred on a swimmer of radius a the slip velocity is

$$\boldsymbol{u}_s = \sum_l [A_l P_l(\cos\theta_s)\boldsymbol{s}_r + B_l V_l(\cos\theta_s)\boldsymbol{s}_\theta + aC_l V_l(\cos\theta_s)\boldsymbol{s}_\phi], \tag{2.19}$$

where $P_l^m(x)$ are the associated Legendre polynomials, with $P_l \equiv P_l^0$, and V_l is defined by Lighthill [75] as

$$V_l(x) \equiv -\frac{2}{l(l+1)} P_l^1(x). \tag{2.20}$$

The coefficients of the radial and meridional modes have units of speed, and C_l has units of angular frequency. A_0 represents uniform expansion or contraction, while

all other modes are volume-preserving.

The swimming speed of the squirmer may be calculated using the reciprocal theorem, eq. (2.6). Since the slip velocity is axisymmetric the azimuthal integral in (2.6) acts only to average the unit vectors in eq. (2.19). Explicitly, if $\boldsymbol{e}_3$ is the direction of the swimmer's head, using standard relations between Cartesian and spherical coordinates we have

$$\int_0^{2\pi} \mathrm{d}\phi_s \, \boldsymbol{s}_r = 2\pi \cos\theta_s \boldsymbol{x}_3 = 2\pi P_1(\cos\theta_s)\boldsymbol{x}_3, \tag{2.21}$$

$$\int_0^{2\pi} \mathrm{d}\phi_s \, \boldsymbol{s}_\theta = -2\pi \sin\theta_s \boldsymbol{x}_3 = 2\pi P_1^1(\cos\theta_s)\boldsymbol{x}_3, \tag{2.22}$$

$$\int_0^{2\pi} \mathrm{d}\phi_s \, \boldsymbol{s}_\phi = 0. \tag{2.23}$$

Then, using orthogonality of Legendre polynomials to integrate over θ, the swimming is in the direction of the axis of symmetry with a speed

$$U = \frac{1}{3}(2B_1 - A_1). \tag{2.24}$$

This is the same swimming speed as calculated by Lighthill [75], and, while the details of the calculation differ, the condition determining it is the same: that the swimmer should be free of net force. This condition is assumed in the derivation of eq. (2.5). A similar procedure using eq. (2.7) determines that the free rotation speed of a squirmer is proportional to C_1.

In asymptotic approximations it is common to truncate the slip velocity to order $l = 2$ and consider only tangential deformations, giving

$$\boldsymbol{u}_s = [B_1 V_1(\cos\theta_s) + B_2 V_2(\cos\theta_s)]\boldsymbol{s}_\theta. \tag{2.25}$$

The first term then sets the swimming speed and asymptotically gives the r^{-3} dependence of the flow of a source dipole [75, 76]; the second term corresponds to a stresslet [67] as in associated with a flow that decays asymptotically as r^{-2}. The ratio of B_1 and B_2 determines whether a swimmer is a pusher (in which case the ratio is negative) or a puller (positive).

Blake has given a two-dimensional analogue [78] of the squirming set, eq. (2.19), describing small oscillations about an infinite cylinder of radius a. The slip velocity is decomposed into Fourier modes with real coefficients A_n, B_n describing the radial flow, u_r, and the tangential flow, u_θ. Despite the laziness in notation it will hopefully be clear from the context when A_n, B_n are two-dimensional and where they are three-dimensional. The flow on the swimmer's surface is expressed relative to

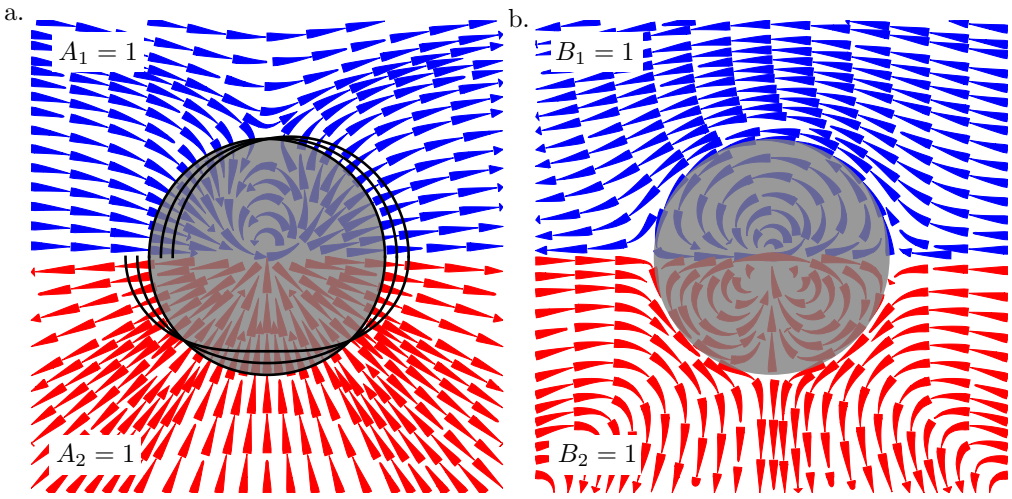

Figure 2.4: Some low order squirming modes according to the Fourier decomposition of Blake [78]. The three-dimensional modes of Lighthill [75] and Blake [76] are analogous. (a) The two lowest-order radial modes visualised as volume-preserving changes of shape about a circle, A_1 (blue) and A_2 (red). (b) The two lowest-order tangential, shape-preserving modes, B_1 (blue) and B_2 (red). Higher-order modes are analogous. A_0 is ignored here, and corresponds to uniform expansion or contraction.

its head's orientation, α, as

$$u_r = \sum_{n=0}^{\infty} A_n \cos n(\theta - \alpha), \qquad u_\theta = \sum_{n=1}^{\infty} B_n \sin n(\theta - \alpha), \tag{2.26}$$

where u_r and u_θ are the radial and tangential components of slip velocity, respectively. With this convention in place it was found that the swimming speed is $\frac{1}{2}(B_1 - A_1)$ [78], which again is easy to derive using the reciprocal theorem, eq. (2.8). The first two radial and tangential modes and the flow field they generate are shown in fig. 2.4.

2.4.1 Time-dependent squirming

The squirmer formulation allows for calculation of swimming behaviour based on an explicit cycle of deformation about a sphere. In this way Lighthill [75] was able to propose a number of different swimming strategies of this type, and calculate their propulsion speed and energetic efficiency. Here we demonstrate the two-dimensional model proposed by Blake [78], but the three-dimensional case is analogous [75, 76].

The swimmer is taken to be a disc of radius a, with points on its surface parametrised by the polar angle θ. The squirming activity results in deformations

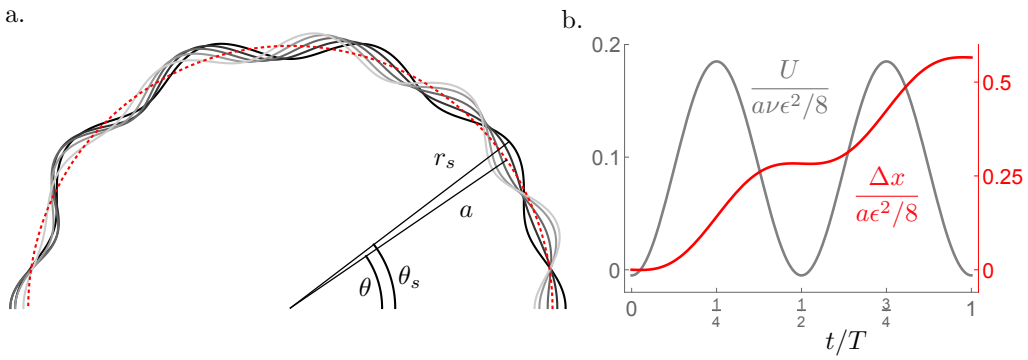

Figure 2.5: (a). A model of a microorganism driven by small oscillations of shape about a circle or sphere. Model and figure after Lighthill [75], Blake [76, 78]. The grey lines show the progression of the metachronal wave on the surface at intervals of one-twelfth the time period. (b) Speed (grey) and displacement (red) of two-dimensional squirmer shown in (a) over one time period. Parameter values used with eq. (2.29) are $\epsilon_1 = \epsilon_4 = -\epsilon_2 = -\epsilon_3 = \epsilon = 0.05$ and $N = 10$. The time-dependent squirming coefficients are given in tables 2.1 and 2.2.

$A_n(t)$		
n	$\mathcal{O}(a\epsilon)$	$\mathcal{O}(a\epsilon^2)$
0	-	$\frac{\nu}{4}(\epsilon_2^2 - \epsilon_1^2 - 2N\epsilon_1\epsilon_3 + 2(N+1)\epsilon_2\epsilon_4)\sin 2\nu t$
1	-	$\frac{\nu}{4}(\epsilon_1\epsilon_4 + \epsilon_3\epsilon_2) + \frac{\nu}{4}(2\epsilon_1\epsilon_2 + (2N+1)(\epsilon_2\epsilon_3 + \epsilon_1\epsilon_4))\cos 2\nu t$
N	$-\nu\epsilon_1 \sin \nu t$	-
$N+1$	$\nu\epsilon_2 \cos \nu t$	-
$2N$	-	$-\frac{\nu}{4}\epsilon_1^2 \sin 2\nu t$
$2N+1$	-	$\frac{\nu}{4}(2N+1)(\epsilon_1\epsilon_4 - \epsilon_3\epsilon_2) + \frac{\nu}{4}(2\epsilon_1\epsilon_2 + \epsilon_1\epsilon_4 - \epsilon_3\epsilon_2)\cos 2\nu t$
$2N+2$	-	$\frac{\nu}{4}\epsilon_2^2 \sin 2\nu t$

Table 2.1: Time-dependent radial squirming modes of the Blake model squirmer.

to the shape, so that the point (a, θ) is mapped to $(r_s(\theta, t), \theta_s(\theta, t))$, as shown in fig. 2.5, where r_s and θ_s are appropriate periodic functions of time, decomposed in coefficients $\mathcal{A}_n(t), \mathcal{B}_n(t)$ as

$$r_s(t) = a\Big[1 + \epsilon \sum_{n\geq 2} \mathcal{A}_n(t) \cos n(\theta - \alpha)\Big], \quad \theta_s(t) = \theta + \epsilon \sum_{n\geq 1} \mathcal{B}_n(t) \sin n(\theta - \alpha). \quad (2.27)$$

The parameter ϵ represents to the typical size of the oscillations. The analogous three-dimensional case is obtained by replacing $\cos n(\theta - \alpha)$ by $P_n(\cos(\theta - \alpha))$ and $\sin n(\theta - \alpha)$ by $V_n(\cos(\theta - \alpha))$ in eq. (2.27).

In order for the surface activity to represent a travelling wave we must have that $\mathcal{A}_n(t)$ and $\mathcal{A}_{n+1}(t)$, and $\mathcal{B}_n(t)$ and $\mathcal{B}_{n+1}(t)$, are approximately one quarter

$B_n(t)$		
n	$\mathcal{O}(a\epsilon)$	$\mathcal{O}(a\epsilon^2)$
1	-	$\frac{\nu}{4}\big(2N(\epsilon_1\epsilon_4+\epsilon_2\epsilon_3-\epsilon_1\epsilon_2+\epsilon_3\epsilon_4)+3\epsilon_1\epsilon_2+2\epsilon_1\epsilon_4+\epsilon_3\epsilon_4\big)$ $+\frac{\nu}{4}\big(2N(\epsilon_1\epsilon_4-\epsilon_2\epsilon_3)-\epsilon_1\epsilon_2+2\epsilon_1\epsilon_4+\epsilon_3\epsilon_4\big)\cos 2\nu t$
N	$-\nu\epsilon_3\sin\nu t$	-
$N+1$	$\nu\epsilon_4\cos\nu t$	-
$2N$	-	$\frac{\nu}{4}\big(N(\epsilon_1-\epsilon_3)^2-2\epsilon_1^2\big)\sin 2\nu t$
$2N+1$	-	$\frac{\nu}{4}\big((2N+1)(\epsilon_1\epsilon_4-\epsilon_2\epsilon_3)-(\epsilon_1-\epsilon_3)(\epsilon_2-\epsilon_4)\big)$ $+\frac{\nu}{4}\big(2\epsilon_1\epsilon_4+3\epsilon_1\epsilon_2-\epsilon_3\epsilon_4-2N(\epsilon_1-\epsilon_3)(\epsilon_2-\epsilon_4)\big)\cos 2\nu t$
$2N+2$	-	$\frac{\nu}{4}\big(2\epsilon_2^2-(N+1)(\epsilon_2-\epsilon_4)^2\big)\sin 2\nu t$

Table 2.2: Time-dependent tangential squirming modes of the Blake model squirmer.

cycle out of phase [76]. Then the time-dependent squirming coefficients $A_n(t), B_n(t)$ may be related to the deformation functions $\mathcal{A}_n(t), \mathcal{B}_n(t)$ by Taylor expansion in the amplitude of the surface oscillations, of order $\epsilon \ll 1$. Thus, for instance, the swimming speed to first order is

$$U = \tfrac{1}{2}a\epsilon\dot{\mathcal{B}}_1. \tag{2.28}$$

Since $\mathcal{B}_1(t)$ is periodic the average speed is zero, and one must go to higher order to see motion in an unbounded fluid.

Consider the explicit model proposed by Blake [78], consisting of the four deformation functions

$$\begin{aligned} \mathcal{A}_N &= \frac{\epsilon_1}{\epsilon}\cos\nu t, \qquad & \mathcal{A}_{N+1} &= \frac{\epsilon_2}{\epsilon}\sin\nu t, \\ \mathcal{B}_N &= \frac{\epsilon_3}{\epsilon}\cos\nu t, \qquad & \mathcal{B}_{N+1} &= \frac{\epsilon_4}{\epsilon}\sin\nu t. \end{aligned} \tag{2.29}$$

for a particular integer $N > 2$ with angular frequency ν, and all other $\mathcal{A}_n, \mathcal{B}_n$ equal to zero. This is the minimal model that exhibits both radial and tangential deformation, and results in motion, since a swimmer with deformation functions of only one order would be constrained to be stationary by symmetry under time reversal. The corresponding time-dependent squirming coefficients are given to second order in the oscillation amplitudes in tables 2.1 and 2.2.

An effective description of the squirming is given by time-averaging the squirming coefficients. It can be seen from tables 2.1 and 2.2 that the only squirming coefficients that are not purely oscillatory are those of order $n = 1$ and $2N + 1$, appearing at second-order in the deformation amplitude ϵ. The average swimming

speed is

$$\langle U\rangle_t = \tfrac{\nu a}{8}\Big[(2N+1)(\epsilon_1\epsilon_4+\epsilon_2\epsilon_3-\epsilon_1\epsilon_2+\epsilon_3\epsilon_4)+4\epsilon_1\epsilon_2-2\epsilon_2\epsilon_3\Big]. \tag{2.30}$$

Just like Taylor's waving sheet, also driven by a travelling wave on the surface [21], the swimming speed is proportional to the wavenumber N, and may be maximised or reversed by appropriate selection of $\epsilon_1, \epsilon_2, \epsilon_3$ and ϵ_4.

It is interesting to note that for $N > 2$ this model has no dipole contribution, having $A_2 = B_2 = 0$. This is sharp contrast with the common treatment of swimmers as stresslets. Instead the leading-order contribution is due the source dipole terms, A_1, B_1. The stresslet terms enter at third order in oscillation amplitude. Of course, different swimming strategies will change the squirming set, and addition of extra contributions to eq. (2.29) will add extra beat frequencies which may include the stresslet modes. Nevertheless, the fact that consecutive modes must be $\pi/2$ out of phase means any even-numbered beats are purely oscillatory at second order in ϵ, so even a more complicated model exhibits no dipole contribution if the swimming stroke is time-averaged; hence, the pusher-puller categorisation breaks down. The consequences of this on interactions are discussed by Pooley et al. [6]. *Volvox carteri* is approximately spherical and thus is apparently an ideal organism to compare to the squirmer model [77]. Hydrodynamic synchronisation between flagella on its surface [135] result in an envelope well-described by a travelling wave [136]. However, modelling *Volvox* as a squirmer results in a significant under-estimate of its self propulsion speed [133]; as the flagella coating its surface are separated by distances comparable to the length of the flagella themselves, the description of *Volvox* by a deforming envelope is inappropriate. Drescher et al. [39], in contrast, find that the experimentally measured flow generated by swimming *Volvox* is very well described by a classic asymptotic model of stresslet-plus-source-dipole, shown in fig. 2.2 (nevertheless some sources still describe *Volvox* as a neutral swimmer [137]).

3

Approximate calculations

In this chapter we investigate the use of point-singularity solutions of the Stokes equations in approximating swimmer problems. While point-singularity models of swimmers are common in the literature in both two [127, 128, 138–140] and three [4, 43, 47, 65] dimensions, the approach we outline here is complementary to these, which model the swimmer itself as a collection of moving singularities and calculate interactions based on reflections of these singularities. Instead, here we approximate the integration kernel used with the reciprocal theorem, while keeping the slip velocity general.

At large distances the flow due to the dragging of any body through a viscous fluid resembles a Stokeslet; therefore, using the Stokeslet (and rotlet, for rotation) as a conjugate solution for the reciprocal theorem allows the motion of a swimmer of any shape to be approximated. In addition to the freedom to specify an arbitrary slip velocity in eq. (2.9), this makes the reciprocal theorem a powerful tool.

The approach shown here was introduced by Papavassiliou and Alexander [66], and also outlined independently by Davis and Crowdy [129] who demonstrate a comparison to a more usual matched-asymptotic calculation for the interaction of a swimmer with a wall.

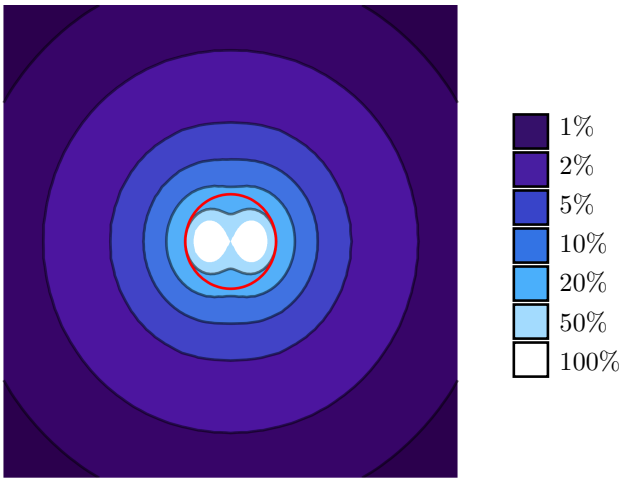

Figure 3.1: Error in the magnitude of the flow about a dragged sphere (red) approximated by a Stokeslet, in the lab frame. Dragging is in the horizontal direction.

3.1 The approximate Stokes drag on a sphere

The flow field due to a sphere at the origin with a no-slip boundary, dragged by a force $\boldsymbol{F}$ is

$$u_i = \frac{F_k}{8\pi\mu}\left(\frac{\delta_{ik}}{|\boldsymbol{r}|} + \frac{r_i r_k}{|\boldsymbol{r}|^3}\right) + \frac{a^2 F_k}{24\pi\mu}\left(\frac{\delta_{ik}}{|\boldsymbol{r}|^3} - 3\frac{r_i r_k}{|\boldsymbol{r}|^5}\right), \qquad p = \frac{F_k r_k}{4\pi|\boldsymbol{r}|^3}. \tag{3.1}$$

In terms of fundamental singularities the first term is the free-space Stokeslet, and the second is a source dipole. As the dipole has constant pressure, the pressure is just that of a Stokeslet.

It can be seen that the flow field to leading order decays as the inverse of distance, with corrections at third order. Thus as long as the distance from the sphere is larger than its radius, just a point force gives a reasonable approximation; fig. 3.1 shows that even on the surface of the sphere the error in the magnitude of the flow field is at most 50% if approximated by a Stokeslet only.

The method here could be improved by including higher-order singularities, starting with the source dipole present in eq. (3.1) and in principle continuing to any order of the multipole expansions calculated by Hicks [141] and Basset [142], among others; however, the rapid decay of these higher-order contributions means the correction to the far field behaviour will be negligible while any truncation is inappropriate in the contact limit. The Stokeslet is common to the dragging of any object, with corrections due to shape entering at higher order.

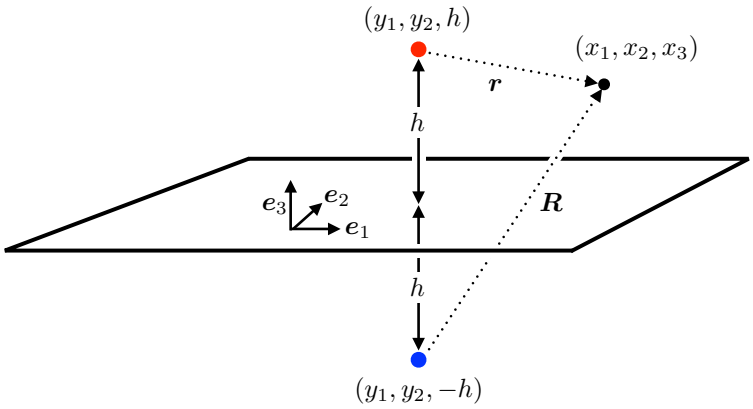

Figure 3.2: The flow at (x_1, x_2, x_3) due to a point force (red) at (y_1, y_2, h) near an infinite planar surface, $x_3 = 0$, is a Stokeslet at this point plus a Stokeslet and higher order singularities at its image (blue) under reflection in the wall. $\boldsymbol{r}$ and $\boldsymbol{R}$ are the respective position vectors of a point in the fluid from these singular points. Adapted from Blake [120].

3.2 Swimming close to a planar surface

Microorganisms near a wall exhibit a variety of interesting behaviour. The attraction to surfaces first reported by Rothschild [45], resulting in a non-uniform distribution of spermatozoa between two microscope slides, has since been confirmed to be a generic hydrodynamic effect [47]. Flagellated bacteria such as *Escherichia coli* and *Vibrio alginolyticus* are known to trace out circles near boundaries, with the direction of the circling depending on the nature of the boundary [4, 42–44, 46] (see fig. 1.1). Ciliated surfaces are ubiquitous in nature, playing, to give one example, a crucial role in the transport of mucus in the lungs, with defects leading to potentially serious respiratory disease [125, 143]; artificial ciliated surfaces have been proposed in microtechnological roles for sorting of particles [144] and influencing flow [145].

The study of interactions with a planar boundary also provides a first approximation to motion in more complicated geometries, of which the wall is a limiting case. While some exact solutions for the Stokes drag of a sphere close to a wall exist [113, 114] these are incomplete, giving only the axisymmetric components of the motion; these will be explored in Chapter 5. Subsequent attempts to include the components of motion parallel to the wall have not managed to give a closed solution [116, 146].

Instead, by the procedure described in § 2.2.1 an approximate solution for the motion of a swimmer near a wall may be found using Blake's solution for a point force and torque in this geometry [120, 147]. This solution allows an integration

kernel to be constructed which, in principle, can be used to calculate the motion of a swimmer of any shape, if the reciprocal theorem integral is performed over the appropriate domain, and any slip velocity, if this can be written down in a closed expression.

3.2.1 Blake's solution

It is well-known that the electric field generated by a point charge near an infinite conducting plate is described by the method of images, with an equal and opposite charge an equal distance on the other side of the wall [148]. Similarly, in solving the flow for a point force close to a no-slip wall a good initial guess is for an equal force pointing in the opposite direction. Since we seek a solution to the Stokes equations rather than the simpler Laplace equation this procedure does not solve the problem, but it simplifies it enough that a solution is straightforward, and leads to a convenient representation of the solution in terms of point-singularities [131]. In this way the flow due to a point force near a no-slip wall was given by Blake in a seminal analysis [120], and has come to be known by some as the Blakelet [149]. Although the result had been known for a long time, having been first derived by Lorentz [90], Blake's was the first representation of the solution as an image system composed purely of flow singularities. Blake's method was subsequently expanded upon to calculate the image systems for higher-order singularities, specifically the rotlet, stresslet and source-doublet, near a wall [147]; a schematic representation of this is shown in fig. 3.3. A two-dimensional analogue was calculated by Crowdy and Or [127].

If we have a Stokeslet of vector strength $\boldsymbol{F}$ at (y_1, y_2, h), with a wall at $x_3 = 0$, then the flow and pressure at (x_1, x_2, x_3) depend only on $\boldsymbol{r} = (x_1 - y_1, x_2 - y_2, x_3 - h)$ and $\boldsymbol{R} = (x_1 - y_1, x_2 - y_2, x_3 + h)$, as illustrated in fig. 3.2. Assuming Einstein notation, where Greek letter indices run over the directions parallel to the wall, $\alpha, \beta, \dots = \{1, 2\}$, and Latin letters run over all three directions, the flow and pressure driven by this point force near a wall is

$$u_i = \frac{F_j}{8\pi\mu}\left[\left(\frac{\delta_{ij}}{r} + \frac{r_i r_j}{r^3}\right) - \left(\frac{\delta_{ij}}{R} + \frac{R_i R_j}{R^3}\right) + 2h(\delta_{j\alpha}\delta_{\alpha k} - \delta_{j3}\delta_{3k})\frac{\partial}{\partial R_k}\left\{\frac{hR_i}{R^3} - \left(\frac{\delta_{i3}}{R} + \frac{R_i R_3}{R^3}\right)\right\}\right], \tag{3.2}$$

$$p = \frac{F_j}{4\pi}\left[\frac{r_j}{r^3} - \frac{R_j}{R^3} - 2h(\delta_{j\alpha}\delta_{\alpha k} - \delta_{j3}\delta_{3k})\frac{\partial}{\partial R_k}\left\{\frac{R_3}{R^3}\right\}\right]. \tag{3.3}$$

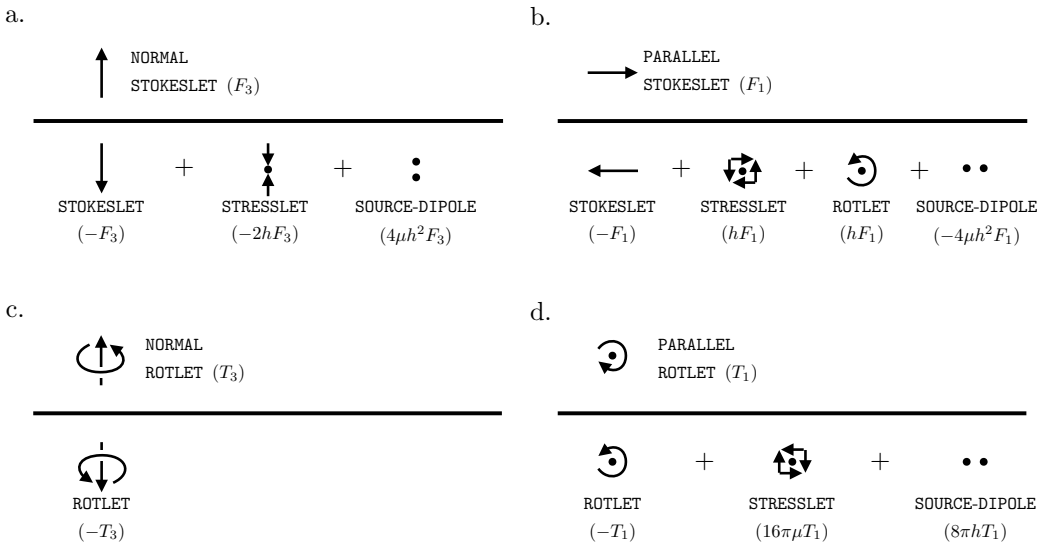

Figure 3.3: Blake & Chwang's representations of the image systems for point forces and torques near a wall. The quantities in brackets indicate the strength of the contribution. The higher-order contributions are obtained by differentiating the Stokeslet and the source. For instance, the dipole in (b) is the derivative in the parallel direction of a normal Stokeslet, while the stresslet in (d) is a symmetrised dipole. Adapted from Blake and Chwang [147].

The first term in these expressions is the free-space Stokeslet, eq. (2.11); the second term can be identified as a Stokeslet of equal and opposite strength at the image point $(y_1, y_2, -h)$, while the remainder is composed of higher-order singularities, illustrated in fig. 3.3. Similarly, the flow and pressure due to a point torque $\boldsymbol{T}$ are

$$u_i = \frac{T_j}{8\pi\mu}\left[\frac{\epsilon_{ijk}r_k}{r^3} - \frac{\epsilon_{ijk}R_k}{R^3} + 2h\epsilon_{kj3}\left(\frac{\delta_{ik}}{R^3} - \frac{3R_iR_k}{R^5}\right) + 6\epsilon_{kj3}\frac{R_iR_kR_3}{R^5}\right], \tag{3.4}$$

$$p = -\frac{T_j}{2\pi}\frac{\partial}{\partial R_k}\left\{\frac{\epsilon_{kj3}R_{3\cdot}}{R^3}\right\}. \tag{3.5}$$

Here, instead, the leading order term is composed of a rotlet, eq. 2.13, and an equal and opposite image rotlet; if the rotlet is aligned with the wall normal, $\boldsymbol{T} = (0, 0, T_3)$, this completes the solution.

3.2.2 Reciprocal theorem

By approximating a swimmer as a point, valid when its size is small compared to h, an approximation of the motion of any swimmer near a passive or active wall may be obtained. If S is the boundary of a swimmer centred on h and W is the surface

of the wall on $x_3 = 0$, the reciprocal theorem takes the form of an integral over the wall and an integral over the swimmer of the slip velocities,

$$\tilde{\boldsymbol{F}} \cdot \boldsymbol{U} + \tilde{\boldsymbol{T}} \cdot \boldsymbol{\Omega} = \int \boldsymbol{u}_s \cdot (\tilde{\boldsymbol{\sigma}}^{\boldsymbol{F}} + \tilde{\boldsymbol{\sigma}}^{\boldsymbol{T}}) \cdot \hat{\boldsymbol{n}} \Big|_{\mathrm{S}} + \int \boldsymbol{u}_s \cdot (\tilde{\boldsymbol{\sigma}}^{\boldsymbol{F}} + \tilde{\boldsymbol{\sigma}}^{\boldsymbol{T}}) \cdot \hat{\boldsymbol{n}} \Big|_{\mathrm{W}}. \tag{3.6}$$

The integration kernels $\tilde{\boldsymbol{\sigma}}^{\boldsymbol{F}}$ and $\tilde{\boldsymbol{\sigma}}^{\boldsymbol{T}}$ are the stress tensors corresponding to a point force and a point torque in this geometry, which may be derived from eqs. (3.2-3.3) and eqs. (3.4-3.5) respectively using the definition of the stress tensor given in eq. (1.2).

The advantage of using the reciprocal theorem is that the slip velocities in eq. (3.6) remain unspecified. Hence the swimming strategy is left completely arbitrary, giving a greater range of results obtainable using these two stress tensors. For example, if the wall has some surface activity the motion of a passive (no-slip) tracer particle is found by the integral

$$\tilde{\boldsymbol{F}} \cdot \boldsymbol{U} + \tilde{\boldsymbol{T}} \cdot \boldsymbol{\Omega} = \int \boldsymbol{u}_s \cdot (\boldsymbol{\sigma}^{\boldsymbol{F}} + \boldsymbol{\sigma}^{\boldsymbol{T}}) \cdot \hat{\boldsymbol{n}} \Big|_{\mathrm{W}}. \tag{3.7}$$

Instead, if the wall has no slip on its surface and we have an active particle, the motion is given by

$$\tilde{\boldsymbol{F}} \cdot \boldsymbol{U} + \tilde{\boldsymbol{T}} \cdot \boldsymbol{\Omega} = \int \boldsymbol{u}_s \cdot (\boldsymbol{\sigma}^{\boldsymbol{F}} + \boldsymbol{\sigma}^{\boldsymbol{T}}) \cdot \hat{\boldsymbol{n}} \Big|_{\mathrm{S}}. \tag{3.8}$$

By the linearity of the Stokes equations and of the reciprocal theorem, summing eqs. (3.7) and (3.8) gives the motion of an active swimmer near an active wall.

3.2.3 Stress tensors for Stokes drag near a wall

The stress tensors that enable evaluation of eq. 3.6 are easily obtained given eqs. (3.2-3.5): one differentiates the flow and symmetrises, multiplies by the viscosity and subtracts the pressure times the identity. This yields the stress tensors

$$\tilde{\sigma}_{ij}^{\tilde{\boldsymbol{F}}} = \frac{3\tilde{F}_k}{4\pi}\Bigg[-\frac{r_i r_j r_k}{|\boldsymbol{r}|^5} + \frac{R_i R_j R_k}{|\boldsymbol{R}|^5} + 2h(\delta_{k\alpha}\delta_{\alpha l} - \delta_{k3}\delta_{3l})\Big(-\frac{h(R_i\delta_{jl} + R_j\delta_{il} + R_l\delta_{ij})}{|\boldsymbol{R}|^5} + \frac{(R_i R_j \delta_{3l} + R_j R_3 \delta_{il} + R_i R_3 \delta_{jl})}{|\boldsymbol{R}|^5} + \frac{5(h - R_3)R_i R_j R_l}{|\boldsymbol{R}|^7}\Big)\Bigg], \tag{3.9}$$

and

$$\tilde{\sigma}_{ij}^{\tilde{\boldsymbol{T}}} = \frac{3\tilde{T}_l}{8\pi}\Bigg[-\frac{(\epsilon_{ilk}r_j+\epsilon_{jlk}r_i)r_k}{|\boldsymbol{r}|^5}+\frac{(\epsilon_{ilk}R_j+\epsilon_{jlk}R_i)R_k}{|\boldsymbol{R}|^5} + \frac{2\epsilon_{kl3}\big(R_k(R_i\delta_{j3}+R_j\delta_{i3})+R_3(R_i\delta_{jk}+R_j\delta_{ik})\big)}{|\boldsymbol{R}|^5} - \frac{4h\epsilon_{kl3}(R_i\delta_{jk}+R_j\delta_{ik}+R_k\delta_{ij})}{|\boldsymbol{R}|^5}+\frac{20\epsilon_{kl3}(h-R_3)R_iR_jR_k}{|\boldsymbol{R}|^7}\Bigg]. \tag{3.10}$$

Both of these expressions contain a singular term depending on $\boldsymbol{r}$, arising from the Stokeslet or rotlet in the fluid. Therefore this term is the stress tensor corresponding to motion in an infinite fluid and, together with the reciprocal theorem, gives the propulsion speed in an unbounded domain. All other terms arise from the image system required to satisfy boundary conditions on the wall, and therefore fully encode the interaction. Here the free swimming speed is assumed known, or in any case is easily determined using the reciprocal theorem of Stone and Samuel [89], so we henceforth remove these terms from eqs. (3.9) and (3.10).

3.3 An active wall

Ciliated walls are a ubiquitous feature of the interior of higher animals, found, for instance, in respiratory [143] and reproductive tracts [126]. Coordination of beating flagella is known to occur in the lining of mammalian lungs, resulting in a metachronal wave [150], and understanding the effect of this beating on the fluid surrounding the ciliated surface, and on objects supsended in this fluid, is important in explaining phenomena such as the clearing of mucus from airways [143] and the transport of the ovum in the fallopian tubes [126].

While there exists a significant literature modelling ciliary arrays [24, 125, 143, 151, 152], much of this work has focused on microstructure, particularly the shape of individual cilia and the optimal beating patterns for locomotion and transport [18, 153], and the mechanisms by which cilia synchronise hydrodynamically [135, 150]. Liron gave models for a planar channel [152] and a pipe [125] coated with cilia. Each cilium is described by a flexible array of Stokeslets undergoing some periodic deformation in time; nevertheless it was found that in the interior of the channel/pipe the flow is time-independent. This indicates that an averaged approach is appropriate for describing the effect of active boundaries on fluid in the bulk. As done by Lighthill [75], we model a covering of cilia by an 'envelope' traced out by their tips, acting as a small deformation of the wall; this assumes that the cil-

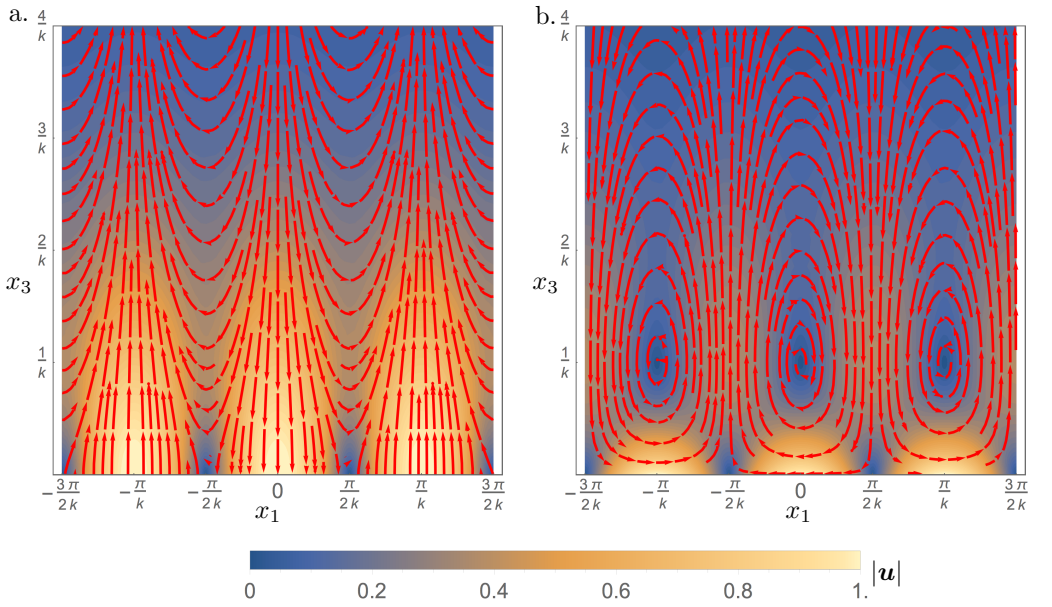

Figure 3.4: The advection of fluid driven by a ciliated wall with slip velocity $\boldsymbol{u}_s$. (a) A transverse wave $\boldsymbol{u}_s = A\cos(kx_1 - \omega t)\boldsymbol{e}_3$. (b) A longitudinal wave $\boldsymbol{u}_s = A\cos(kx_1 - \omega t)\boldsymbol{e}_1$. Up to a phase difference of $\pi/2$ the flow far from the wall is the same. The former gives a flow field identical to that calculated by Taylor [21] for an infinite waving sheet.

iary covering is dense, with the inter-ciliary distance smaller than the length of the cilia [136].

We describe this ciliary envelope by a slip velocity on the wall corresponding to transverse or longitudinal travelling wave,

$$\begin{matrix}\boldsymbol{u}_s^{\text{trans.}} \\ \boldsymbol{u}_s^{\text{long.}}\end{matrix} = A\cos(kx_1 - \omega t) \begin{matrix}\boldsymbol{e}_3 \\ \boldsymbol{e}_1.\end{matrix} \tag{3.11}$$

where k is the wavenumber and ω is the frequency, and t is time. The length of the cilia is assumed to be much shorter than the wavelength of the wave, so that this slip velocity is imposed on the wall. Using this slip velocity together with the stress tensors (3.9) and (3.10), the reciprocal theorem allows the calculation of the advection of a passive, no-slip tracer particle of size $a \ll h$. Faxén's law says that the leading contribution to advection of a spherical particle is the background flow at its centre, with corrections at order radius-squared [92], so as long as this tracer is very small, its motion also gives the flow field; in fact, as we saw in § 2.2, the calculation of the flow field in this way is exact.

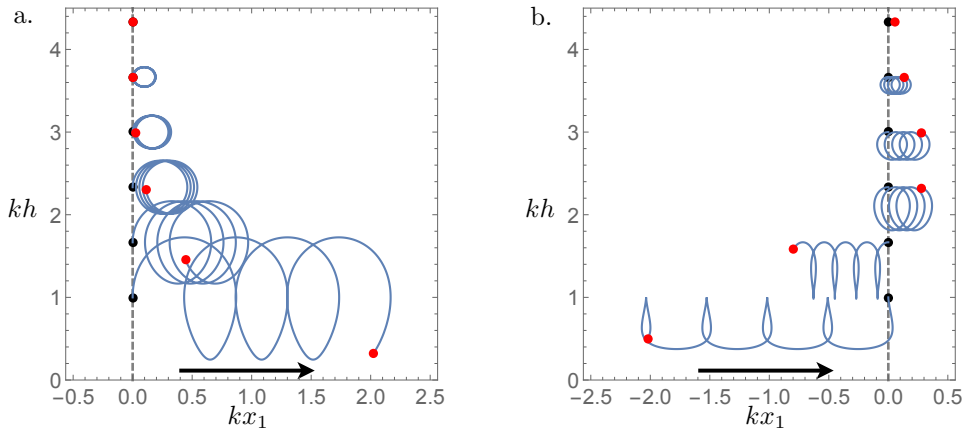

Figure 3.5: Trajectories of a tracer particle near a ciliated wall with (a) transverse actuation and (b) longitudinal actuation. Black dots denote initial location, red dots denote location after four time periods of the beating on the wall and black arrow indicates the direction of wave propagation. Far-field flow is in the same direction as the wave propagation in both cases, while in the near field the longitudinal wave results in a counter-current. This suggests that the transverse travelling wave corresponds to symplectic beating and the longitudinal wave to antiplectic beating. A reversal in flow far from a ciliated surface was also found by Liron [125, 152], and a similar effect occurs in the displaced flow by a passing squirmer [79].

To integrate eq. (3.7) on the wall we set $|\boldsymbol{r}| = |\boldsymbol{R}| = \sqrt{x_1^2 + x_2^2 + h^2} \equiv \sqrt{\rho^2 + h^2}$, $R_3 = h$ and $r_3 = -h$. The wall normal is $\hat{\boldsymbol{n}} = -\boldsymbol{e}_3$ and so the integration kernel is $-\tilde{\sigma}_{i3}$, which has the form

$$\tilde{\sigma}_{i3}^{\tilde{\boldsymbol{F}}} = \frac{3h\tilde{F}_k}{2\pi|\boldsymbol{R}|^5}(h\delta_{i3} - R_\alpha\delta_{i\alpha})(h\delta_{k3} - R_\beta\delta_{k\beta}) \tag{3.12}$$

and

$$\tilde{\sigma}_{33}^{\tilde{\boldsymbol{T}}} = \frac{3h}{4\pi|\boldsymbol{R}|^5}\epsilon_{3lk}\tilde{T}_l R_k, \quad \tilde{\sigma}_{\alpha 3}^{\tilde{\boldsymbol{T}}} = \frac{3\tilde{T}_l}{8\pi|\boldsymbol{R}|^5}\left[\epsilon_{3l\alpha}h^2 + \epsilon_{\alpha l\beta}hR_\beta - \epsilon_{3l\beta}R_\beta R_\alpha\right] \tag{3.13}$$

to determine the translation and rotation of the tracer particle, or, equivalently, the flow and the vorticity.

Insertion of the surface activities, eq. (3.11), into eq. (3.7) with integration

kernels (3.12) and (3.13) and integrating finally gives the flow field and vorticity

$$\begin{aligned} u_1 &= -Akh\mathrm{e}^{-kh}\sin(kx_1-\omega t),\\ u_3 &= A(1+kh)\mathrm{e}^{-kh}\cos(kx_1-\omega t),\\ \omega_2 &= -\frac{A}{2}k\mathrm{e}^{-kh}\sin(kx_1-\omega t). \end{aligned} \tag{3.14}$$

for transverse actuation and

$$\begin{aligned} u_1 &= A(1-kh)\mathrm{e}^{-kh}\cos(kx_1-\omega t),\\ u_3 &= Akh\mathrm{e}^{-kh}\sin(kx_1-\omega t),\\ \omega_2 &= \frac{A}{2}k\mathrm{e}^{-kh}\cos(kx_1-\omega t). \end{aligned} \tag{3.15}$$

for longitudinal actuation. These two flow fields are shown in fig. 3.4. Both exhibit exponential confinement of the flow to the region near the wall, of thickness smaller than the wavelength; within this region the two flow fields differ considerably. Fig. 3.5 shows trajectories of a small tracer particle for a variety of initial conditions for each type of wall activity; it can be seen that the transverse metachronal wave, fig. 3.5(a), advects the tracer in the same direction as the phase velocity, the longitudinal metachronal wave, fig. 3.5(b), does the opposite, indicating *a posteriori* that the former represents a symplectic wave and the latter an antiplectic wave [150].

Far from the wall, $h \gg k^{-1}$, the flow fields due to a transverse and longitudinal metachronal wave have the same behaviour, up to a phase difference which may be eliminated by a suitable redefinition; we expect that this is therefore generic behaviour which does not depend on the microscopic details of the ciliary coating of the wall. The far-field advection in both cases is in the same direction as the propagation of the metachronal wave. This means that it is in the opposite direction to the dragging close to the wall for longitudinal beating, as shown in fig. 3.5(b). This is seen in the much more detailed discrete-cilia models of active pipes [125] and walls [152], and has also been reported in the advection of tracer particles by a passing swimmer [79].

Finally, it is noted that eq. (3.14) is exactly the same flow as that calculated by Taylor for an infinite waving sheet [21] – this is no surprise since the problem is the same, although the details of the calculation differ.

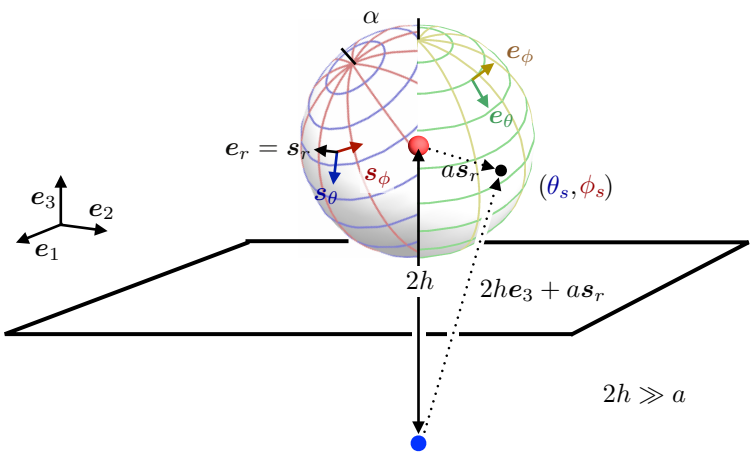

Figure 3.6: Surface coordinate systems on a spherical swimmer of radius a, a distance h above a wall. The swimmer spherical basis $\{\boldsymbol{s}_r, \boldsymbol{s}_\theta, \boldsymbol{s}_\phi\}$ (red and blue) is related to the lab spherical basis $\{\boldsymbol{e}_r, \boldsymbol{e}_\theta, \boldsymbol{e}_\phi\}$ (green and gold) by a rotation of α about $\boldsymbol{e}_2$. The red and blue points are the locations of the singularities and images, as in fig. 3.2.

3.4 A swimmer close to a wall

The presence of a solid boundary has a significant influence on swimmer motion, and can cause organisms to align themselves parallel to the surface and follow circular trajectories [40–42], or be attracted to the surface and aggregate [45, 47]. Much of this behaviour has been explained qualitatively using leading-order multipole expansions [43, 65]. Here we show that a complementary approximate approach using the reciprocal theorem, with the approximation in the integration kernel rather than the slip velocity, produces the same results with relatively little calculational effort, and generalises to arbitrary slip velocities and swimming strategies. Furthermore, despite the level of approximation, a comparison to exact results that will be shown in Chapter 5 reveals that the equations of motion found by this first approximation hold up to separations between the swimmer and the wall of only a few swimmer diameters. By the linearity of the reciprocal theorem (or, equivalently, Faxén's law) the advection of an active particle by an active wall is given by summing the motion of the active particle near a no-slip wall and eqs. (3.14)-(3.15).

We take the swimmer to be a sphere of radius $a \ll h$ and expand in a. The integration kernel is then obtained by setting

$$\boldsymbol{r} = -a\hat{\boldsymbol{n}} = a\boldsymbol{e}_r, \qquad \boldsymbol{R} = 2h\boldsymbol{e}_3 + \mathcal{O}(a), \tag{3.16}$$

and expanding in inverse powers of the separation of the swimmer from the surface,

h. The leading-order part of the stress tensor that determines translation due to wall interactions is

$$\tilde{\sigma}_{ij}^{\tilde{\boldsymbol{F}}} = \frac{3\tilde{F}_k}{4\pi}\left[\frac{\delta_{i3}\delta_{j3}\delta_{k3}}{(2h)^2} + (\delta_{k\alpha}\delta_{\alpha l} - \delta_{k3}\delta_{3l})\Big(-\frac{(\delta_{i3}\delta_{jl} + \delta_{j3}\delta_{il} + \delta_{l3}\delta_{ij})}{2(2h)^2} + \frac{(\delta_{i3}\delta_{j3}\delta_{3l} + \delta_{j3}\delta_{il} + \delta_{i3}\delta_{jl})}{(2h)^2} - \frac{5\delta_{i3}\delta_{j3}\delta_{k3}}{2(2h)^2}\Big)\right] + \mathcal{O}[h^{-3}]. \tag{3.17}$$

Finally, the integration kernel for use with the reciprocal theorem is

$$[\tilde{\boldsymbol{\sigma}}^{\tilde{\boldsymbol{F}}} \cdot \hat{\boldsymbol{n}}]_i = -\frac{3}{8\pi(2h)^2}\Big(\tilde{F}_3\Big(3\delta_{i3}e_{r3} + e_{ri}\Big) + \tilde{F}_\alpha\Big(\delta_{i\alpha}e_{r3} + \delta_{i3}e_{r\alpha}\Big)\Big) + \mathcal{O}[h^{-3}]. \tag{3.18}$$

Similarly, the leading-order part of the stress tensor corresponding to rotation of the sphere arising from to interaction with the boundary is

$$[\tilde{\boldsymbol{\sigma}}^{\tilde{\boldsymbol{T}}} \cdot \hat{\boldsymbol{n}}]_i = -\frac{3\tilde{T}_\alpha}{8\pi(2h)^3}\Big(\epsilon_{3i\alpha}e_{r3} + \epsilon_{3j\alpha}\delta_{i3}e_{rj}\Big) + \mathcal{O}[h^{-4}]. \tag{3.19}$$

The stress tensor for rotation normal to the wall is more rapidly decaying and requires expansion to the next order in h^{-1},

$$[\tilde{\boldsymbol{\sigma}}^{\tilde{T}_3} \cdot \hat{\boldsymbol{n}}]_i = -\frac{3a}{8\pi(2h)^4}\tilde{T}_3\epsilon_{3ki}e_{rk}e_{r3} + \mathcal{O}[h^{-5}]. \tag{3.20}$$

These expressions can be used with any slip velocity that can be written down explicitly. This contrasts with calculations based on multipole expansions [43, 47, 65], for which any distinct slip velocity or swimming stroke must be modelled separately; this flexibility is a significant advantage of using the reciprocal theorem to calculate interactions.

We shall restrict ourselves to axisymmetric slip velocities expanded in squirming modes, so that, in the swimmer basis $\{\boldsymbol{s}_r, \boldsymbol{s}_\theta, \boldsymbol{s}_\phi\}$,

$$\boldsymbol{u}_s = \sum_l A_l P_l(\cos\theta_s)\boldsymbol{s}_r + B_l V_l(\cos\theta_s)\boldsymbol{s}_\theta + aC_l V_l(\cos\theta_s)\boldsymbol{s}_\phi. \tag{3.21}$$

The easiest way to calculate the reciprocal theorem integral is to transform the slip velocity to the lab frame to contract against the stress tensor, then perform the spherical integral in swimmer coordinates. If the swimmer's head is inclined to the

wall normal by an angle α, as in fig. 3.6, the appropriate transformations are

$$\begin{bmatrix} \boldsymbol{s}_r \\ \boldsymbol{s}_\theta \\ \boldsymbol{s}_\phi \end{bmatrix} = \begin{bmatrix} \sin\theta_s\cos\phi_s & \sin\theta_s\sin\phi_s & \cos\theta_s \\ \cos\theta_s\cos\phi_s & \cos\theta_s\sin\phi_s & -\sin\theta_s \\ -\sin\phi_s & \cos\phi_s & 0 \end{bmatrix} \begin{bmatrix} \cos\alpha & 0 & -\sin\alpha \\ 0 & 1 & 0 \\ \sin\alpha & 0 & \cos\alpha \end{bmatrix} \begin{bmatrix} \boldsymbol{e}_1 \\ \boldsymbol{e}_2 \\ \boldsymbol{e}_3 \end{bmatrix} \tag{3.22}$$

The tilt of the head is taken to be in the 1-direction and as a consequence of axisymmetry $U_2 = \Omega_1 = 0$. The remaining components are found to be

$$U_1 = \frac{B_2 - A_2}{5}\left(\frac{a}{2h}\right)^2 P_2^1(\cos\alpha) + \mathcal{O}[h^{-3}], \tag{3.23}$$

$$U_3 = -\frac{3(B_2 - A_2)}{5}\left(\frac{a}{2h}\right)^2 P_2(\cos\alpha) + \mathcal{O}[h^{-3}], \tag{3.24}$$

$$a\Omega_2 = \frac{B_2 - A_2}{5}\left(\frac{a}{2h}\right)^3 P_2^1(\cos\alpha) + \mathcal{O}[h^{-4}], \tag{3.25}$$

$$\Omega_3 = \frac{C_2}{5}\left(\frac{a}{2h}\right)^4 P_2(\cos\alpha) + \mathcal{O}[h^{-5}]. \tag{3.26}$$

Recognising that A_2 and B_2 correspond to a stresslet flow, we note that expressions (3.23), (3.24) and (3.25) are the same as those found by Spagnolie and Lauga [65] for the interaction of a force dipole with a wall. Particularly interesting is the rotation about the wall normal, Ω_3, which leads to circular trajectories of particles swimming parallel to the wall. When $\theta_0 = \pi/2$ this rotation is given by

$$\Omega_3 = \frac{a^4 C_2}{160h^4} + \mathcal{O}(h^{-5}). \tag{3.27}$$

The squirming mode C_2 corresponds to a flow that circulates in an easterly sense in the northern hemisphere but in a westerly sense in the southern hemisphere, so that a swimmer with this squirming mode qualitatively resembles bacteria like *E. coli* which have a counter-rotating head and tail. Indeed, such bacteria are known to swim in circles close to boundaries [42]. The direction of the circling is set by the direction of the head-tail rotation and is left-handed if C_2 is positive. The radius of curvature depends on the free swimming speed U^{free}, and is $160U^{\text{free}}h^4/a^3C_2$, indicating that this effect is strongly localised at boundaries, as reported experimentally [43]. This h^{-4} decay of the rotation was also found by [4] by considering the dynamics of a rotlet dipole – precisely the flow structure of the squirming mode C_2 [133].

An alternative calculational strategy is to decompose the stress tensor in Legendre polynomials directly. This has the advantage of immediately generalising results to arbitrary squirming order, since now integration kernel is expanded in an

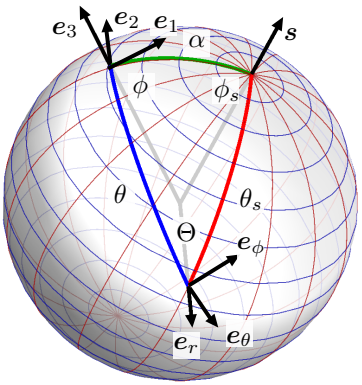

Figure 3.7: Spherical geometry relating swimmer and lab bases. The swimmer spherical basis $\{\boldsymbol{s}_r, \boldsymbol{s}_\theta, \boldsymbol{s}_\phi\}$ is related to the lab spherical basis $\{\boldsymbol{e}_r, \boldsymbol{e}_\theta, \boldsymbol{e}_\phi\}$ by a rotation Θ about $\boldsymbol{e}_r = \boldsymbol{s}_r$.

infinite series in the same basis as the slip velocity. As an example, consider the normal rotation, given to leading order by eq. (3.26). The integrand is

$$\boldsymbol{u}_s \cdot \tilde{\boldsymbol{\sigma}}^{\tilde{T}_3} \cdot \hat{\boldsymbol{n}} = -\frac{3\tilde{T}_3}{8\pi} \frac{a(\boldsymbol{s}_r \cdot \boldsymbol{R})}{|\boldsymbol{R}|^5} [\boldsymbol{e}_3 \cdot (\boldsymbol{s}_r \times \boldsymbol{u}_s)]. \tag{3.28}$$

In the lab spherical basis, $\{\boldsymbol{e}_r, \boldsymbol{e}_\theta, \boldsymbol{e}_\phi\}$, this may be written as

$$\boldsymbol{u}_s \cdot \tilde{\boldsymbol{\sigma}}^{\tilde{T}_3} \cdot \hat{\boldsymbol{n}} = -\frac{3\tilde{T}_3}{8\pi} \frac{\bar{a}^4(\bar{a} + \cos\theta)}{a^3(1 + \bar{a}^2 + 2\bar{a}\cos\theta)^{\frac{5}{2}}} \boldsymbol{e}_3 \cdot (\boldsymbol{e}_r \times \boldsymbol{u}_s), \tag{3.29}$$

where $\bar{a} \equiv a/2h$. From the generating function for Legendre polynomials [154] we obtain the identity

$$\frac{(t-x)}{(1+t^2-2tx)^{\frac{5}{2}}} = \frac{1}{3} \sum_{n=0}^{\infty} \frac{(n-1)t^{n-2}}{(1-x^2)^{\frac{1}{2}}} P_n^1(x), \tag{3.30}$$

so the reciprocal theorem becomes

$$\Omega_3 = \frac{1}{8\pi} \int_{\theta,\phi} a^2 \sin\theta \, \mathrm{d}\theta \, \mathrm{d}\phi \sum_{n=0}^{\infty} \frac{(n-1)\bar{a}^{n+2} P_n^1(-\cos\theta)}{a^3 \sin\theta} \boldsymbol{e}_3 \cdot (\boldsymbol{e}_r \times \boldsymbol{u}_s). \tag{3.31}$$

In order to integrate this some spherical geometry, shown in fig. 3.7, is required to express the slip velocity in terms of the lab spherical basis that the stress tensor is written in. By the spherical cosine law the swimmer polar angle θ_s satisfies

$$\cos\theta_s = \cos\alpha\cos\theta + \sin\alpha\sin\theta\cos\phi, \tag{3.32}$$

while the basis vectors are related by a rotation about the sphere normal,

$$\boldsymbol{s}_\theta = \cos\Theta\,\boldsymbol{e}_\theta - \sin\Theta\,\boldsymbol{e}_\phi, \quad \boldsymbol{s}_\phi = \sin\Theta\,\boldsymbol{e}_\theta + \cos\Theta\,\boldsymbol{e}_\phi, \tag{3.33}$$

where, using the spherical sine law,

$$\sin\Theta \equiv \frac{\sin\alpha\sin\phi}{\sin\theta_s}, \quad \cos\Theta \equiv \sqrt{1-\frac{\sin^2\alpha\sin^2\phi}{\sin^2\theta_s}}. \tag{3.34}$$

Since the stress tensor is axisymmetric in this case the integral over ϕ has the effect of azimuthally averaging the tangential slip velocity, giving

$$\Omega_3 = \frac{1}{4}\int_{\theta,\phi} a^2\sin\theta \mathrm{d}\theta\,\mathrm{d}\phi \sum_{n=0}^{\infty}\frac{(n-1)\bar{a}^{n+2}P_n^1(-\cos\theta)}{a^3\sin\theta}\boldsymbol{e}_3\cdot\langle\boldsymbol{e}_r\times\boldsymbol{u}_s\rangle_\phi. \tag{3.35}$$

where, using the addition theorem for Legendre polynomials [155],

$$\langle\boldsymbol{e}_r\times\boldsymbol{u}_s\rangle_\phi \equiv \frac{1}{2\pi}\int_0^{2\pi}\mathrm{d}\phi\,(\boldsymbol{e}_r\times\boldsymbol{u}_s) = \sum_l P_l(\cos\alpha)V_l(\cos\theta)\Big(B_l\boldsymbol{e}_\phi - aC_l\boldsymbol{e}_\theta\Big). \tag{3.36}$$

This will be explained in more detail in Chapter 5, where a similar procedure will be used to calculate exact three-dimensional solutions for squirming near a wall (compare fig. 5.5 with fig. 3.7); there it will be desirable to include higher-order modes to resolve the near-field behaviour, so the slip velocity will again be re-expressed in a basis coinciding with that of the integration kernel.

Finally, using orthogonality of the Legendre polynomials, the rotation about the wall normal is computed to be

$$\Omega_3 = \sum_{n=2}^{\infty} C_n P_n(\cos\alpha)(-1)^n\frac{(n-1)}{(2n+1)}\Big(\frac{a}{2h}\Big)^{n+2}, \tag{3.37}$$

agreeing with, and generalising, eq. (3.26). Other components of motion follow in much the same way, although the calculations are not shown here. We find that

$$\begin{aligned} U_3 = \sum_{l=0}^{\infty}(-1)^{l+1}P_l(\cos\alpha)\Bigg[&\frac{3(l-1)(l+1)}{2(2l-1)(2l+1)}\Big(\frac{a}{2h}\Big)^l(2B_l - lA_l) \\ &- \frac{(l+3)}{(2l+1)(2l+3)}\Big(\frac{a}{2h}\Big)^{l+2}\Big(2l(l+2)B_l + (l+1)(l^2-l-3)A_l\Big)\Bigg], \end{aligned} \tag{3.38}$$

$$U_1 = \sum_{l=0}^{\infty}(-1)^{l+1}\left[\frac{3(l-1)l}{2(2l-1)(2l+1)}\Big(\frac{a}{2h}\Big)^{l} - \frac{(l+1)(l^2-l-3)}{(2l+1)(2l+3)}\Big(\frac{a}{2h}\Big)^{l+2}\right]A_l P_l^1(\cos\alpha), \tag{3.39}$$

$$a\Omega_2 = \sum_{l=0}^{\infty}(-1)^{l+1}\left[\frac{3(l-1)^2}{(2l-1)(2l+1)}\Big(\frac{a}{2h}\Big)^{l+1} - \frac{2(l+2)(l^2-l-3)}{(2l+1)(2l+3)}\Big(\frac{a}{2h}\Big)^{l+3}\right]A_l P_l^1(\cos\alpha). \tag{3.40}$$

We have so far not succeeded in obtained a closed expression for the components U_1 and Ω_2 driven by tangential slip B_l, although we have reduced both to the expressions

$$\begin{aligned} U_1(B_n) = \sum_l \int_0^{\pi} \mathrm{d}\theta\, \sin\theta \frac{3\bar{a}^2}{4\pi}\Bigg[\Bigg(&\frac{(1+2\bar{a}^2+3\bar{a}\cos\theta)(\cos^2\theta-\sin^2\theta)}{2(1+\bar{a}^2+2\bar{a}\cos\theta)^{5/2}} \\ &+ \frac{5(1+2\bar{a}\cos\theta)(\bar{a}+\cos\theta)\bar{a}\sin^2\theta}{2(1+\bar{a}^2+2\bar{a}\cos\theta)^{7/2}}\Bigg)\langle\cos\phi\cos\Theta V_l(\cos\theta_s)\rangle_\phi \\ &+ \frac{(\bar{a}+\cos\theta)(1+2\bar{a}\cos\theta)}{2(1+\bar{a}^2+2\bar{a}\cos\theta)^{5/2}}\langle\sin\phi\sin\Theta V_l(\cos\theta_s)\rangle_\phi\Bigg] B_l \end{aligned} \tag{3.41}$$

and

$$\begin{aligned} \Omega_2(B_n) = \sum_l \int_0^{\pi} \mathrm{d}\theta\, \sin\theta \frac{3\bar{a}^2}{4\pi}\Bigg[\Bigg(&\frac{(1+2\bar{a}^2+4\bar{a}\cos\theta)\cos^2\theta - \frac{1}{2}(1+\bar{a}^2+4\bar{a}\cos\theta)}{(1+\bar{a}^2+2\bar{a}\cos\theta)^{5/2}} \\ &+ \frac{5(1+2\bar{a}\cos\theta)(\bar{a}+\cos\theta)\bar{a}\sin^2\theta}{2(1+\bar{a}^2+2\bar{a}\cos\theta)^{7/2}}\Bigg)\langle\cos\phi\cos\Theta V_l(\cos\theta_s)\rangle_\phi \\ &+ \frac{(\bar{a}+\cos\theta)(1+3\bar{a}\cos\theta)}{2(1+\bar{a}^2+2\bar{a}\cos\theta)^{5/2}}\langle\sin\phi\sin\Theta V_l(\cos\theta_s)\rangle_\phi\Bigg] B_l. \end{aligned} \tag{3.42}$$

All the azimuthal dependence is contained in the angled braces, which denote an integral over ϕ from 0 to 2π. Just as we have seen in eqs. (2.6) and (2.6), this indicates what contributions to the slip velocity result in motion. The rest of the integrand is axisymmetric and may be expanded in Legendre polynomials as before.

These expansions demonstrate the versatility of the reciprocal theorem: using just the solutions for a point force and torque near a wall we have derived a complete, albeit approximate, description of the interaction of a spherical organism with any axisymmetric slip velocity with a solid boundary.

We emphasise that the above have been calculated for completeness. The fast spatial decay of higher-order behaviour decays means that, while neat, these contributions become influential only as the contact limit is approached, in which case the point-singularity approximation is not valid. Nevertheless some important facts are highlighted. The angular dependence of each squirming mode is described

by a Legendre polynomial of the same order as the squirming mode, of degree zero for motion about or along the wall normal and degree one for motion parallel to the wall. Just as the flow field due to a squirming mode of order l has a contribution decaying as r^{-l} and one as $r^{-(l+2)}$ [75, 76], each squirming mode gives two contributions to the interaction with a wall, with the same spatial decay.

3.5 Squirming in confined geometries

In many real-world cases swimming microorganisms exist in strong confinement. This could be thin films [156–158], channels [48] or porous media [159]; the human gut alone contains up to 500 different species of bacteria, and about ten times as many bacterial cells as there are eukaryotic cells in the entire body [160]. The complexity and diversity of these environments hinders mathematical modelling, particularly if exact solutions are desired; however, the long-standing interest in Green's functions for Stokes flow for a variety of geometries means several solutions exist which enable swimmer problems to be tackled in an approximate fashion, as explained in § 3.2. We now consider one such solution.

Following an approach analogous to that of Blake [120], Liron and Mochon [121] found the solution for a Stokeslet between two infinite parallel plates. This involves an infinite array of reflections of the Stokeslet, as illustrated in 3.8(b), supplemented by an auxiliary solution which satisfies any outstanding boundary conditions. Although the solution has a closed form, the authors have not found a way to express it in terms of fundamental singularities. This solution was then used to model an array of cilia between two plates by modelling each cilium as a distribution of point forces [152], a theoretical approximation of a ciliated tubule such as the male ductus efferentes. The explicit solution for a Stokeslet in a pipe was subsequently also found [124] and applied to biologically-motivated transport problems [125].

Here we will show that this solution may be used to construct a stress tensor to calculate motion in this confined geometry. This allows, for instance, the calculation of flow inside the channel due to activity on the surface, although this has already been investigated in depth by the much more detailed approach of modelling cilia using point forces [152]. However, we may also find the swimming behaviour in a channel, as well as the interaction of a swimmer with an imposed active pumping, and compare the results to those seen for a single wall. Understanding of swimming between parallel plates is of particular relevance to experimental biology, where confinement between a pair of microscope slides is commonplace [45]. *Paramecium*

has been observed to follow an oscillating trajectory when confined to the narrow space between two plates [161]; this has recently been analysed in detail numerically by Shum and Gaffney [162] and de Graaf et al. [163] in studies that provide a central point of comparison for the results that will be shown in this section. In particular it was found that pushers follow unstable oscillating trajectories which grow in amplitude and lead to collisions with the plates, while pullers follow damped oscillatory trajectories which converge to a linear path along the middle of the channel; this is perhaps to be expected as a result of the time-reversal duality between pushers and pullers. The analogous two-dimensional case of a disc swimming in an infinite fluid strip of finite width has been studied by Crowdy and Davis [139], although only for one type of slip velocity corresponding to a stresslet.

Firstly we will compute the Stokes flow due to a point torque in this channel geometry; this is done by analogy to the original calculation of the Stokeslet [121], and completes the solution so that all components of motion may be found. As far as we are aware this is a new result. Then we will present the leading-order components of motion of a spherical squirmer, of very small size compared to the separation of the plates, and discuss the behaviour, in particular comparing with the results for a single wall shown in § 3.4.

3.5.1 A rotlet between two plates

As we have seen before in eq. (2.13), the flow at $\boldsymbol{x}$ due to point torque $\boldsymbol{T}$ at $\boldsymbol{y}$ is given by the rotlet,

$$\boldsymbol{u} = \frac{1}{8\pi\mu}\frac{\boldsymbol{T}\times(\boldsymbol{x}-\boldsymbol{y})}{|\boldsymbol{x}-\boldsymbol{y}|^3}, \qquad p = 0. \tag{3.43}$$

The pressure is constant for any axisymmetric azimuthal flow [114], and in an unbounded fluid any axis is an axis of symmetry so the rotlet has no pressure gradients associated with it.

Now consider a rotlet between two no-slip plates. We know from the well-established results for point-singularities near a single no-slip wall that the leading-order image singularity for a rotlet is a rotlet of equal and opposite strength, located an equal distance from the wall [147]. If the point torque is aligned with the normal to the wall this completes the solution; otherwise there are additional higher-order image singularities. We start with this contribution. For two walls, we have an infinite number of reflections, of alternating sign. Having written this down we will seek to add an auxiliary solution to the flow field which is regular everywhere in the fluid, to satisfy any unresolved boundary conditions.

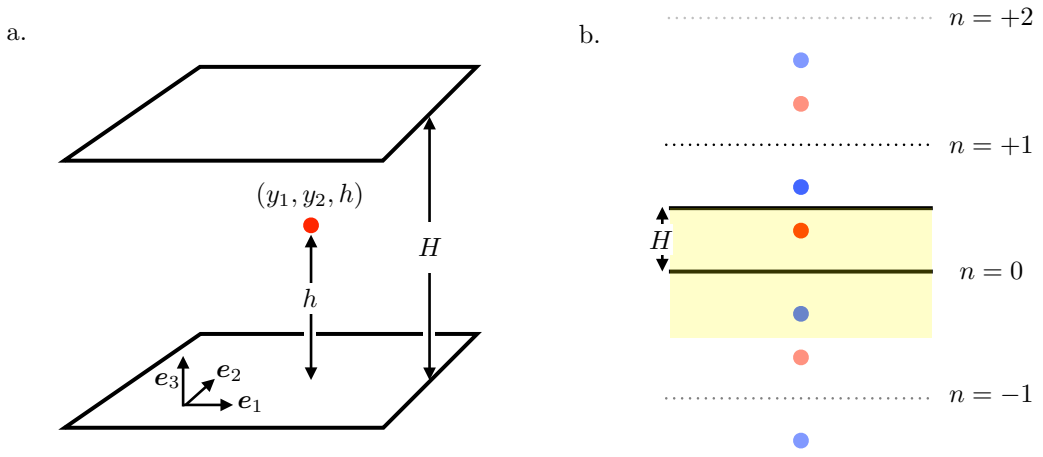

Figure 3.8: Setup for a point singularity between two plates, adapted from Liron and Mochon [121]. (a) A point-singularity is located at the point (y_1, y_2, h) between two plates at which the flow vanishes, at $x_3 = 0$ and $x_3 = H$. (b) The locations of the reflected singularities of order n that form the initial guess of the solution. Red singularities have the same sign as the singularity in the channel, blue singularities have the opposite sign. The $n = 0$ term (yellow region) is the image system at a wall, while the full reflection scheme takes the yellow region to be a unit cell of size $2H$ in the x_3 direction. This periodic structure allows the solutions to be Hankel transformed trivially.

Reflections of the source

Consider a flat wall located at $x_3 = 0$, and another at $x_3 = H$, as shown in fig. 3.8. A point torque of unit strength is located at (y_1, y_2, h), with $0 < h < H$. Reflections of this singularity of opposite strength are located at

$$\boldsymbol{R}_n \equiv (x_1 - y_1, x_2 - y_2, x_3 + h + 2nH), \quad R_n \equiv |\boldsymbol{R}_n|, \tag{3.44}$$

while those of equal strength are at

$$\boldsymbol{r}_n \equiv (x_1 - y_1, x_2 - y_2, x_3 - h + 2nH), \quad r_n \equiv |\boldsymbol{r}_n|, \tag{3.45}$$

where n runs over all integers in both cases. Introducing Einstein notation, where once more Greek letter indices run over $\alpha, \beta, \cdots = \{1, 2\}$ and Latin letters run over all three directions, the flow field, v_i, due to this infinite array is given by

$$v_i = \frac{1}{8\pi\mu}\epsilon_{ijk}T_j \sum_{n=-\infty}^{\infty}\left[\frac{r_{n,k}}{r_n^3} - \frac{R_{n,k}}{R_n^3}\right], \qquad p = 0. \tag{3.46}$$

Since all $\boldsymbol{r}_n$ and $\boldsymbol{R}_n$ lie on a line along $\boldsymbol{e}_3$, the components parallel to the plates are the same, $r_{n,\alpha} = R_{n,\alpha} \equiv r_\alpha \, \forall n$ and eq. (3.46) may be written

$$v_i = \frac{1}{8\pi\mu}\epsilon_{ij\alpha}T_j r_\alpha \sum_{n=-\infty}^{\infty}\left[\frac{1}{(\rho^2 + r_{n,3}^2)^{\frac{3}{2}}} - \frac{1}{(\rho^2 + R_{n,3}^2)^{\frac{3}{2}}}\right] + \frac{1}{8\pi\mu}\epsilon_{ij3}T_j \sum_{n=-\infty}^{\infty}\left[\frac{r_{n,3}}{(\rho^2 + r_{n,3}^2)^{\frac{3}{2}}} - \frac{R_{n,3}}{(\rho^2 + R_{n,3}^2)^{\frac{3}{2}}}\right] \tag{3.47}$$

where $\rho = \left((x_1 - y_1)^2 + (x_2 - y_2)^2\right)^{1/2} = (r_\alpha r_\alpha)^{1/2}$ is the cylindrical radius. Now we make use of the Lipschitz integral [164],

$$(\rho^2 + \tau^2)^{-1/2} = \int_0^\infty J_0(\lambda\rho)\mathrm{e}^{-|\tau|\lambda}\mathrm{d}\lambda. \tag{3.48}$$

Differentiating this gives the identities

$$(\rho^2 + \tau^2)^{-3/2} = \int_0^\infty \frac{\lambda}{\rho}J_1(\lambda\rho)\mathrm{e}^{-|\tau|\lambda}\mathrm{d}\lambda = \int_0^\infty \frac{\lambda}{|\tau|}J_0(\lambda\rho)\mathrm{e}^{-|\tau|\lambda}\mathrm{d}\lambda, \tag{3.49}$$

which allow the flow field to be written as

$$v_i = \frac{1}{8\pi\mu}T_j \sum_{n=-\infty}^{\infty}\int_0^\infty \lambda\Bigg[\epsilon_{ij\alpha}\frac{r_\alpha}{\rho}J_1(\lambda\rho)\left(\mathrm{e}^{-|r_{n,3}|\lambda} - \mathrm{e}^{-|R_{n,3}|\lambda}\right) \tag{3.50}$$

$$+ \epsilon_{ij3}J_0(\lambda\rho)\left(\mathrm{sgn}(r_{n,3})\mathrm{e}^{-|r_{n,3}|\lambda} - \mathrm{sgn}(R_{n,3})\mathrm{e}^{-|R_{n,3}|\lambda}\right)\Bigg]\mathrm{d}\lambda. \tag{3.51}$$

It now becomes necessary to split the solution into two parts, one for $x_3 > h$ and the other for $x_3 < h$, to deal with the discontinuity in the flow at $x_3 = h, \rho = 0$. From eq. (3.44)-(3.45) we have that

$$\mathrm{sgn}(R_{n,3}) = \begin{cases} +1, & n \geq 0 \\ -1, & n < 0 \end{cases} \quad \text{and} \quad \mathrm{sgn}(r_{n,3}) = \begin{cases} +1, & n > 0, \\ \mathrm{sgn}(x_3 - h), & n = 0, \\ -1, & n < 0. \end{cases}, \tag{3.52}$$

giving the flow field

$$v_i = \frac{\epsilon_{ij3}T_j}{4\pi\mu}\int_0^\infty \lambda J_0(\lambda\rho)\frac{\sinh\lambda h}{\sinh\lambda H}\cosh\lambda(H - x_3)\,\mathrm{d}\lambda + \frac{\epsilon_{ij\alpha}T_j}{4\pi\mu}\frac{r_\alpha}{\rho}\int_0^\infty \lambda J_1(\lambda\rho)\frac{\sinh\lambda h}{\sinh\lambda H}\sinh\lambda(H - x_3)\,\mathrm{d}\lambda, \tag{3.53}$$

for $x_3 > h$ and

$$v_i = -\frac{\epsilon_{ij3}T_j}{4\pi\mu}\int_0^\infty \lambda J_0(\lambda\rho)\frac{\sinh\lambda(H-h)}{\sinh\lambda H}\cosh\lambda x_3 \mathrm{d}\lambda + \frac{\epsilon_{ij\alpha}T_j}{4\pi\mu}\frac{r_\alpha}{\rho}\int_0^\infty \lambda J_1(\lambda\rho)\frac{\sinh\lambda(H-h)}{\sinh\lambda H}\sinh\lambda x_3 \mathrm{d}\lambda, \tag{3.54}$$

for $x_3 < h$; these solutions coincide on $x_3 = h$, except at $\rho = 0$ where they are singular. On the plates the flow should vanish; here we have

$$v_i(x_3 = H) = \frac{\epsilon_{ij3}T_j}{4\pi\mu}\int_0^\infty \lambda J_0(\lambda\rho)\frac{\sinh\lambda h}{\sinh\lambda H}\,\mathrm{d}\lambda \tag{3.55}$$

on the top plate and

$$v_i(x_3 = 0) = -\frac{\epsilon_{ij3}T_j}{4\pi\mu}\int_0^\infty \lambda J_0(\lambda\rho)\frac{\sinh\lambda(H-h)}{\sinh\lambda H}\mathrm{d}\lambda \tag{3.56}$$

on the bottom plate. Hence to complete the solution we must find an auxiliary flow which is regular everywhere in the channel, and opposite to these boundary values on the plates. However the flow solution due to a point torque normal to the walls is complete, as is the 3-component of the flow due to a parallel torque.

Auxiliary solution

The requirement is to find a flow field $\boldsymbol{w}$ and a pressure ϖ satisfying

$$\begin{gathered}\boldsymbol{\nabla}\varpi = \mu\nabla^2\boldsymbol{w}, \qquad \boldsymbol{\nabla}\cdot\boldsymbol{w} = 0, \qquad \nabla^2\varpi = 0, \\ \boldsymbol{w}(x_3 = 0, H) = -\boldsymbol{v}(x_3 = 0, H),\end{gathered} \tag{3.57}$$

so that the full solution is given by

$$\boldsymbol{u} = \boldsymbol{v} + \boldsymbol{w}, \qquad p = \varpi. \tag{3.58}$$

As done elsewhere [78, 121, 147] we shall solve this auxiliary problem in Fourier space. If we have cylindrical symmetry so that φ depends only on ρ then the two-dimensional Fourier transform,

$$\hat{\varphi}(\lambda_1, \lambda_2, x_3) = \frac{1}{2\pi}\int_{-\infty}^\infty\int_{-\infty}^\infty \varphi(r_1, r_2, x_3)\mathrm{e}^{\mathrm{i}(\lambda_1 r_1 + \lambda_2 r_2)}\mathrm{d}r_1\,\mathrm{d}r_2, \tag{3.59}$$

is equivalent to the Hankel transform,

$$\hat{\varphi}(\lambda, x_3) = \int_0^\infty \rho J_0(\lambda\rho)\varphi(\rho, x_3)\,\mathrm{d}\rho, \qquad \varphi(\rho, x_3) = \int_0^\infty \lambda J_0(\lambda\rho)\hat{\varphi}(\lambda, x_3)\,\mathrm{d}\lambda, \tag{3.60}$$

where $\lambda \equiv (\lambda_1^2 + \lambda_2^2)^{\frac{1}{2}}$. The reverse Fourier transform is

$$\varphi(r_1, r_2, x_3) = \frac{1}{2\pi} \int_{-\infty}^{\infty} \int_{-\infty}^{\infty} \hat{\varphi}(\lambda_1, \lambda_2, x_3) \mathrm{e}^{-\mathrm{i}(\lambda_1 r_1 + \lambda_2 r_2)} \mathrm{d}\lambda_1 \, \mathrm{d}\lambda_2. \tag{3.61}$$

The previous use of the Lipschitz integral ensured the boundary conditions for the auxiliary solution, eqs. (3.55)-(3.56), are expressed as Hankel transforms. Fourier-transforming the Stokes equations gives

$$-\mathrm{i}\lambda_\alpha \delta_{i\alpha} \hat{\varpi}^j + \delta_{i3} \frac{\partial}{\partial x_3} \hat{\varpi} = \mu \left(\frac{\partial^2}{\partial x_3^2} - \lambda^2 \right) \hat{w}_i, \tag{3.62}$$

while the continuity equation becomes

$$-\mathrm{i}\lambda_\alpha \hat{w}_\alpha + \frac{\partial}{\partial x_3} \hat{w}_3 = 0. \tag{3.63}$$

Since the pressure must be harmonic,

$$\left(\frac{\partial^2}{\partial x_3^2} - \lambda^2 \right) \hat{\varpi} = 0, \tag{3.64}$$

it has the general form

$$\hat{\varpi} = B_0 \sinh \lambda(H - x_3) + C_0 \cosh \lambda(H - x_3), \tag{3.65}$$

where B_0 and C_0 are some complex constants. Finally, the Fourier-transformed boundary conditions are

$$4\pi\mu \hat{w}_i(\lambda, H) = -\epsilon_{ij3} T_j \frac{\sinh \lambda h}{\sinh \lambda H}, \qquad 4\pi\mu \hat{w}_i(\lambda, 0) = \epsilon_{ij3} T_j \frac{\sinh \lambda(H - h)}{\sinh \lambda H} \tag{3.66}$$

Inserting eq. (3.65) into the Stokes equations, (3.62), we find that

$$\begin{aligned} 2\mu \hat{w}_i = {} & B_i \sinh \lambda(H - x_3) + C_i \cosh \lambda(H - x_3) \\ & + \left(B_0 \delta_{i3} + \mathrm{i}\delta_{i\alpha} \frac{\lambda_\alpha}{\lambda} C_0 \right) x_3 \sinh \lambda(H - x_3) \\ & + \left(C_0 \delta_{i3} + \mathrm{i}\delta_{i\alpha} \frac{\lambda_\alpha}{\lambda} B_0 \right) (x_3 - H) \cosh \lambda(H - x_3), \end{aligned} \tag{3.67}$$

for some as-yet undetermined complex vectors $\boldsymbol{B}$ and $\boldsymbol{C}$, and insisting on incompressibility finally gives the linear system

$$C_0 = \lambda H B_0 + \lambda B_3 + \mathrm{i}\lambda_\alpha C_\alpha, \quad B_0 = -\lambda H C_0 + \lambda C_3 + \mathrm{i}\lambda_\alpha B_\alpha. \tag{3.68}$$

The solution of eq. (3.68) with the boundary conditions (3.66) is

$$2\pi C_i = \epsilon_{3ji} T_j \frac{\sinh \lambda h}{\sinh \lambda H}, \tag{3.69}$$

$$2\pi C_0 = \mathrm{i}\epsilon_{3\beta j} T_j \lambda_\beta \frac{(\sinh \lambda h \sinh \lambda H - \lambda H \sinh \lambda (H-h))}{(H^2\lambda^2 - \sinh^2 \lambda H)}, \tag{3.70}$$

$$2\pi B_0 = \mathrm{i}\epsilon_{3\beta j} T_j \lambda_\beta \frac{(\lambda H \cosh \lambda (H-h) - \cosh \lambda h \sinh \lambda H)}{(H^2\lambda^2 - \sinh^2 \lambda H)}, \tag{3.71}$$

$$2\pi B_3 = \mathrm{i}\epsilon_{3\beta j} T_j \lambda_\beta H \coth \lambda H \frac{(\sinh \lambda h \sinh \lambda H - \lambda H \sinh \lambda (H-h))}{(H^2\lambda^2 - \sinh^2 \lambda H)}, \tag{3.72}$$

$$\begin{aligned} 2\pi B_\alpha = {} & \epsilon_{3\alpha j} \frac{\cosh \lambda h}{\sinh \lambda H} \\ & + \epsilon_{3\beta j} \frac{\lambda_\alpha \lambda_\beta}{\lambda^2} \frac{\lambda H \cosh \lambda H}{(H^2\lambda^2 - \sinh^2 \lambda H)} \left(\cosh \lambda h - \frac{\lambda H \cosh \lambda (H-h)}{\sinh \lambda H} \right). \end{aligned} \tag{3.73}$$

As expected, these coefficients are all zero when the rotlet points along the plate normal.

Now we need to transform back to real space. The pressure is

$$2\pi \hat{\varpi} = -\mathrm{i}\epsilon_{\beta 3 j} T_j \lambda_\beta A_\varpi(\lambda, x_3) \tag{3.74}$$

where

$$A_\varpi(\lambda, x_3) = \frac{(\lambda H \sinh \lambda (h - x_3) - \sinh \lambda H \sinh \lambda (H - h - x_3))}{(H^2\lambda^2 - \sinh^2 \lambda H)}, \tag{3.75}$$

so the real-space pressure is

$$2\pi \varpi = \frac{\epsilon_{\beta 3 j} T_j}{2\pi} \int_{-\infty}^{\infty} \int_{-\infty}^{\infty} (-\mathrm{i}\lambda_\beta) A_\varpi(\lambda, x_3) \mathrm{e}^{-\mathrm{i}(\lambda_1 r_1 + \lambda_2 r_2)} \mathrm{d}\lambda_1 \, \mathrm{d}\lambda_2 \tag{3.76}$$

$$= \frac{\epsilon_{\beta 3 j} T_j}{2\pi} \int_{-\infty}^{\infty} \int_{-\infty}^{\infty} \frac{\partial}{\partial r_\beta} A_\varpi(\lambda, x_3) \mathrm{e}^{-\mathrm{i}(\lambda_1 r_1 + \lambda_2 r_2)} \mathrm{d}\lambda_1 \, \mathrm{d}\lambda_2 \tag{3.77}$$

In the second line the differentiation may be taken outside the integration so that the integral is cylindrically symmetric, allowing it to be Hankel-transformed:

$$\begin{aligned} 2\pi \varpi &= \epsilon_{\beta 3 j} T_j \frac{\partial}{\partial r_\beta} \int_0^\infty \lambda J_0(\lambda \rho) A_\varpi(\lambda, x_3) \, \mathrm{d}\lambda \\ &= \epsilon_{3\alpha j} T_j \frac{r_\alpha}{\rho} \int_0^\infty \lambda^2 J_1(\lambda \rho) A_\varpi(\lambda, x_3) \, \mathrm{d}\lambda. \end{aligned} \tag{3.78}$$

For the flow field it is best to consider the different components separately. The

normal flow in Fourier space is

$$4\pi\mu\hat{w}_3 = \mathrm{i}\epsilon_{3\beta j}T_j\lambda_\beta A_{(3)}(\lambda, x_3), \tag{3.79}$$

where

$$\begin{aligned} A_{(3)}(\lambda, x_3) = \Bigg\{ &\frac{\lambda H^2 \sinh\lambda(H-h)\sinh\lambda x_3}{(H^2\lambda^2 - \sinh^2\lambda H)\sinh\lambda H} + \frac{\lambda x_3 H \sinh\lambda(h-x_3)}{(H^2\lambda^2 - \sinh^2\lambda H)} \\ &- \frac{x_3 \sinh\lambda H \sinh\lambda(H-x_3-h)}{(H^2\lambda^2 - \sinh^2\lambda H)} - \frac{H\sinh\lambda x_3 \sinh\lambda h}{(H^2\lambda^2 - \sinh^2\lambda H)}\Bigg\}, \end{aligned} \tag{3.80}$$

so in real space we have

$$4\pi\mu w_3 = \epsilon_{3\alpha j}T_j\frac{r_\alpha}{\rho}\int_0^\infty \lambda^2 J_1(\lambda\rho)A_{(3)}(\lambda, x_3)\,\mathrm{d}\lambda. \tag{3.81}$$

Finally, the parallel flow is

$$4\pi\mu\hat{w}_\alpha = \epsilon_{3\beta j}T_j\bigg(\frac{\sinh\lambda(H-x_3-h)}{\sinh\lambda H}\delta_{\alpha\beta} + \lambda_\alpha\lambda_\beta A_{(\alpha)}(\lambda, x_3)\bigg), \tag{3.82}$$

in Fourier space, where

$$\begin{aligned} A_{(\alpha)}(\lambda, x_3) = \Bigg\{ &\frac{H^2\cosh\lambda(H-h)\sinh\lambda x_3}{(H^2\lambda^2 - \sinh^2\lambda H)\sinh\lambda H} - \frac{x_3 H\cosh\lambda(h-x_3)}{(H^2\lambda^2 - \sinh^2\lambda H)} \\ &+ \frac{x_3\cosh\lambda(H-x_3-h)\sinh\lambda H}{\lambda(H^2\lambda^2 - \sinh^2\lambda H)} - \frac{H\sinh\lambda x_3\cosh\lambda h}{\lambda(H^2\lambda^2 - \sinh^2\lambda H)}\Bigg\}. \end{aligned} \tag{3.83}$$

Thus in real space it is

$$\begin{aligned} 4\pi\mu w_\alpha = \epsilon_{3\beta j}T_j\int_0^\infty \Bigg\{ &\delta_{\alpha\beta}J_0(\lambda\rho)\frac{\sinh\lambda(H-x_3-h)}{\sinh\lambda H} \\ &+ \Big[\delta_{\alpha\beta}\frac{\lambda}{\rho}J_1(\lambda\rho) - r_\alpha r_\beta\frac{\lambda^2}{\rho^2}J_2(\lambda\rho)\Big]A_{(\alpha)}(\lambda, x_3)\Bigg\}\lambda\,\mathrm{d}\lambda. \end{aligned} \tag{3.84}$$

This completes the solution for the rotlet. This supplements the existing solution for a Stokeslet, so that trajectories of a swimmer between two plates may be calculated using the reciprocal theorem.

3.5.2 Stress tensor

In order to use this result together with the reciprocal theorem we need to calculate the stress tensor by differentiating our various flow components. The idea is the same as in § 3.2: we expand the stress tensor about the centre of the (small) swimmer, retaining as much of the tensorial structure as possible.

Hence, we will calculate the stress tensor corresponding the rotlet solution we have just calculated (with the torque henceforth written with a tilde, to emphasise that it corresponds to the conjugate solution), as well as that for the Stokeslet calculated by Liron and Mochon [121], and evaluate them at the point (y_1, y_2, h), corresponding to a zeroth order expansion. The auxiliary solution, being regular everywhere in the channel, will not pose us problems; however, the flow corresponding to the rotlet array, given in eqs. (3.53)-(3.54), is singular at this point. As before, this singularity, and the analogous one in the stress tensor corresponding to the Stokeslet in this geometry, give the motion in an unbounded fluid, and is neglected. The terms that are left fully characterise the interactions with the geometry.

The flow due to the rotlets not in the channel, $\tilde{\boldsymbol{v}}$, is given by

$$4\pi\mu\tilde{v}_i = \frac{\epsilon_{ijk}\tilde{T}_j}{2}\int_0^\infty \left\{\delta_{k3}J_0(\lambda\rho)\frac{\partial A_0}{\partial x_3} - \delta_{k\alpha}r_\alpha\frac{\lambda}{\rho}J_1(\lambda\rho)A_0\right\}\mathrm{d}\lambda, \tag{3.85}$$

where

$$A_0 = \left[\frac{\sinh\lambda x_3}{\sinh\lambda H}\mathrm{e}^{-\lambda(H-h)} + \frac{\sinh\lambda(H-x_3)}{\sinh\lambda H}\mathrm{e}^{-\lambda h}\right] \tag{3.86}$$

and the total back flow, $\tilde{\boldsymbol{u}}$, is

$$\tilde{\boldsymbol{u}} = \tilde{\boldsymbol{v}} + \boldsymbol{w}, \qquad p = \varpi, \tag{3.87}$$

where the auxiliary solution is the same as before. The stress tensor $\tilde{\boldsymbol{\sigma}}$ corresponding to this back flow is given by

$$4\pi\tilde{\boldsymbol{\sigma}} = -4\pi\varpi\,\boldsymbol{I} + 4\pi\mu(\boldsymbol{\nabla}\tilde{\boldsymbol{u}} + (\boldsymbol{\nabla}\tilde{\boldsymbol{u}})^T). \tag{3.88}$$

After some rather tedious algebra we arrive at the expressions

$$\left[\tilde{\boldsymbol{\sigma}}\cdot\boldsymbol{e}_r\right]_i = \frac{1}{8\pi}a\tilde{T}_3\epsilon_{3ji}e_{r3}e_{rj}\int_0^\infty \frac{\partial A_0}{\partial x_3}\frac{\lambda}{\rho}J_1(\lambda\rho)\mathrm{d}\lambda + \mathcal{O}[a^2] \tag{3.89}$$

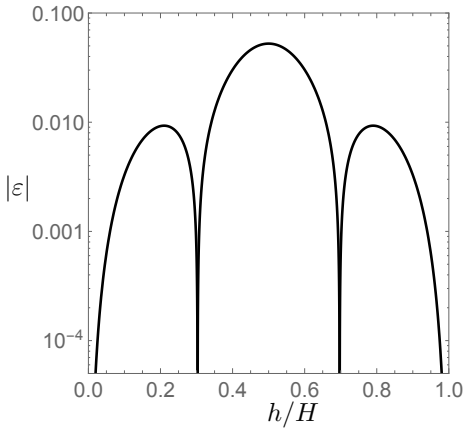

Figure 3.9: Fractional error $|\varepsilon|$ of the approximate integral eq. (3.96) compared to numerical integration of eq. (3.93)

and

$$\left[\tilde{\boldsymbol{\sigma}} \cdot \boldsymbol{e}_r\right]_i = \frac{1}{8\pi}\tilde{T}_\beta(\epsilon_{3i\beta}e_{r3} + \epsilon_{3k\beta}\delta_{i3}e_{rk}) \int_0^\infty \Bigg[\lambda^2 J_0(\lambda\rho)\frac{\cosh\lambda(h-x_3)}{\sinh\lambda H}\mathrm{e}^{-\lambda H} - \frac{\lambda}{\rho}J_1(\lambda\rho)\left[A_0 + \lambda\frac{\partial A_{(\alpha)}}{\partial x_3} + \lambda A_{(3)}\right]\Bigg]\mathrm{d}\lambda + \mathcal{O}[a] \tag{3.90}$$

for the stress tensors corresponding to torques pointing normal and parallel to the plates. The tensorial structure in these expressions is exactly the same as in the leading-order stress tensors used to calculate rotational motion near a single wall, eqs. (3.19) and (3.20).

These stress tensors are approximated by evaluating at the location of the swimmer, $x_3 = h, \rho = 0$, and retaining only the leading order term in the swimmer size a. This procedure is valid as long as the integral above is uniformly convergent; unfortunately we have not yet been able to demonstrate this. This then allows the limit-taking and integration to be exchanged.

Intrepidly assuming this *can* be done, we can take the limit of the integrand using the identity

$$\lim_{\rho\to 0}\rho^{-n}J_n(\lambda\rho) = \frac{\lambda^n}{(2n)!!}, \tag{3.91}$$

which gives the leading-order contributions in an expansion in the swimmer's size

and allows eq. (3.89) to be evaluated as

$$\begin{aligned}\left[\tilde{\boldsymbol{\sigma}}\cdot\boldsymbol{e}_r\right]_i\Big|_{\substack{x_3\to h\\ \rho\to 0}} &= \frac{1}{8\pi}a\tilde{T}_3\epsilon_{3ji}e_{r3}e_{rj}\int_0^\infty \frac{\lambda^3\sinh\lambda(2h-H)}{2\sinh\lambda H}\mathrm{d}\lambda + \mathcal{O}[a^2]\\ &= -\frac{3a\tilde{T}_3}{128\pi H^4}\epsilon_{3ji}e_{r3}e_{rj}\Big(\zeta\Big[4,\tfrac{h}{H}\Big]-\zeta\Big[4,1-\tfrac{h}{H}\Big]\Big)+\mathcal{O}[a^2]. \end{aligned}\tag{3.92}$$

In the same limit the stress tensor for parallel rotation, eq. (3.90), becomes

$$\begin{aligned}\left[\tilde{\boldsymbol{\sigma}}\cdot\boldsymbol{e}_r\right]_i\Big|_{\substack{x_3\to h\\ \rho\to 0}} &= -\frac{1}{8\pi}\tilde{T}_\beta(\epsilon_{3i\beta}e_{r3}+\epsilon_{3k\beta}\delta_{i3}e_{rk})\int_0^\infty\frac{\lambda^2}{2}\Big[\frac{\cosh\lambda(H-2h)}{\sinh\lambda H}\\ &-\frac{3\mathrm{e}^{-\lambda H}}{\sinh\lambda H}+\frac{\lambda^2H^2\cosh\lambda H}{(\lambda^2H^2-\sinh^2\lambda H)\sinh\lambda H}-\frac{2\lambda H\cosh^2\lambda h}{(\lambda^2H^2-\sinh^2\lambda H)}\\ &-\frac{2\lambda h\sinh\lambda H\sinh\lambda(H-2h)}{(\lambda^2H^2-\sinh^2\lambda H)}+\frac{\sinh\lambda H\cosh\lambda(H-2h)}{(\lambda^2H^2-\sinh^2\lambda H)}\Big]\mathrm{d}\lambda+\mathcal{O}[a]. \end{aligned}\tag{3.93}$$

The first two terms under the integral are readily integrated using

$$\frac{1}{\sinh\lambda H}=2\sum_{n=0}^{\infty}\mathrm{e}^{-(2n+1)\lambda H},\tag{3.94}$$

but we have been unable to integrate the remaining terms. Therefore we approximate again, by replacing the denominator by

$$(\lambda^2H^2-\sinh^2\lambda H)^{-1}\to-\sinh^{-2}\lambda H.\tag{3.95}$$

This approximation is appropriate for large λ, but even at $\lambda=0$ the integrand has the correct limit of zero in the approximation. With this in place the integral may be evaluated. A plot of the error of this approximation, compared to a numerical integration performed by Mathematica, is shown in fig. 3.9 and is under 10% in the entire range $0\le h\le H$. Finally, with these approximations in place the integral in eq. (3.93) is

$$\begin{aligned}&\int_0^\infty\frac{\lambda^2}{2}\Big[\frac{2\lambda h\sinh\lambda(H-2h)}{\sinh\lambda H}-\frac{3\mathrm{e}^{-\lambda H}}{\sinh\lambda H}+\frac{2\lambda H\cosh^2\lambda h}{\sinh^2\lambda H}-\frac{\lambda^2H^2\cosh\lambda H}{\sinh^3\lambda H}\Big]\\ &\qquad=\frac{3}{8H^3}\Big(\zeta\Big[3,\tfrac{h}{H}\Big]+\zeta\Big[3,1-\tfrac{h}{H}\Big]-4\zeta[3]\Big),\end{aligned}\tag{3.96}$$

so that the integration kernel for the calculation of rotations parallel to the plates

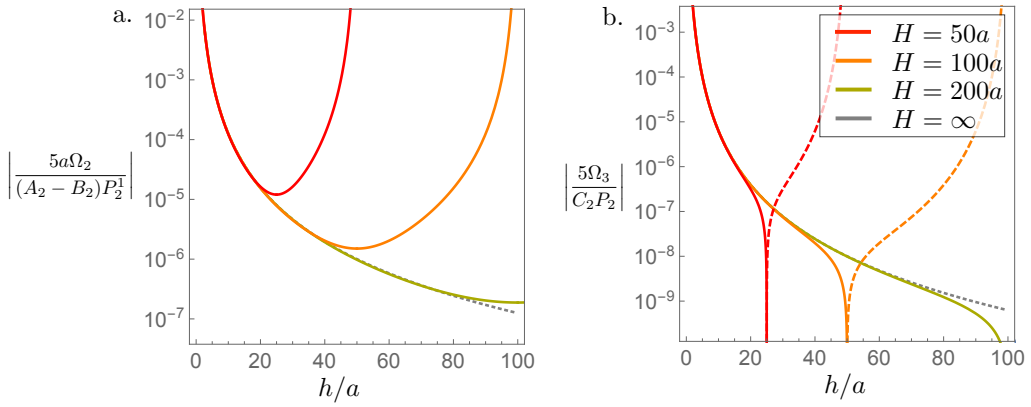

Figure 3.10: The rotation of a squirmer between two plates for a range of plate separations. Asymptotic one-wall limit shown as grey dotted line. (a) Parallel rotation Ω_2. (b) Normal rotation Ω_3. Dashed line indicates change of sign.

is

$$[\tilde{\boldsymbol{\sigma}} \cdot \boldsymbol{e}_r]_i = -\frac{3\tilde{T}_\beta}{64\pi H^3}(\epsilon_{3i\beta}n_3 + \epsilon_{3k\beta}\delta_{i3}n_k)\left(\zeta\left[3, \tfrac{h}{H}\right] + \zeta\left[3, 1-\tfrac{h}{H}\right] - 4\zeta[3]\right) + \mathcal{O}[a]. \tag{3.97}$$

3.5.3 The motion of a squirmer between two plates

Rotation

Now, finally, we may find the behaviour of a swimmer between two plates. The stress tensors have been heavily approximated, but are valid for a very small swimmer not close to either plate, $\frac{a}{H} \ll \frac{h}{H}$. Integrating the stress tensors against a slip velocity expanded in squirming modes, eq. (3.21), we find the rotations

$$a\Omega_2 = \frac{a^3}{8H^3}\left(\zeta\left[3, \tfrac{h}{H}\right] + \zeta\left[3, 1-\tfrac{h}{H}\right] - 4\zeta[3]\right)\frac{(B_2-A_2)}{5}P_2^1(\cos\alpha) + \mathcal{O}[a^4] \tag{3.98}$$

$$\Omega_3 = \frac{a^4}{16H^4}\left(\zeta\left[4, \tfrac{h}{H}\right] - \zeta\left[4, 1-\tfrac{h}{H}\right]\right)\frac{C_2}{5}P_2(\cos\alpha) + \mathcal{O}[a^5], \tag{3.99}$$

with the extra two powers of a coming from the integration measure. Since

$$\zeta\left[n, \tfrac{h}{H}\right] = \sum_{k=0}^{\infty}\left(\tfrac{h}{H}+k\right)^{-n} \to (h/H)^{-n} + \zeta[n] \quad \text{as} \quad \frac{h}{H} \to 0, \tag{3.100}$$

we can take the limit of eqs. (3.98) and (3.99) as the top plate is taken to infinity, $H \to \infty$, finding that they coincide exactly with the expressions calculated for inter-

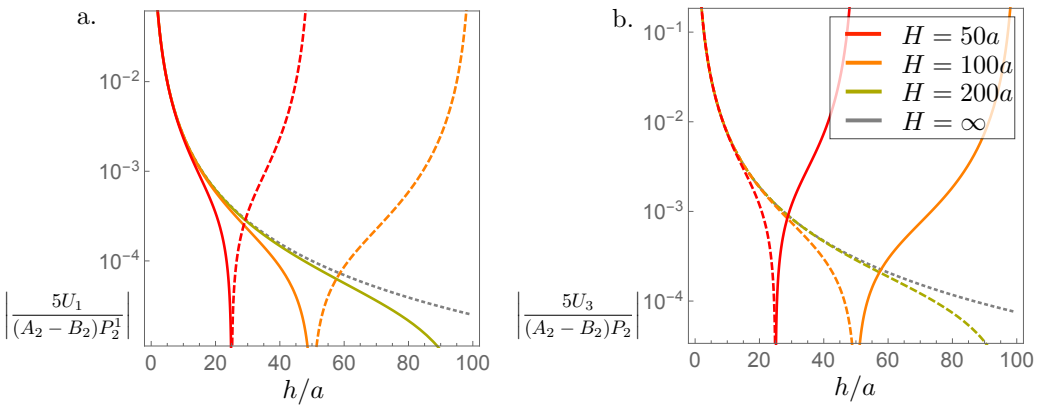

Figure 3.11: The translation of a squirmer between two plates for a range of plate separations. Asymptotic one-wall limit shown as grey dotted line. (a) Parallel translation U_1. (b) Normal translation U_3. Dashed line indicates change of sign.

action with a single wall, (3.25) and (3.26). A comparison is shown in fig. 3.10. It can also be seen that these expressions are symmetric and antisymmetric respectively under $h/H \to 1 - h/H$, as expected.

Translation

Using the solution of Liron and Mochon [121] for a point force in a channel, a similar procedure to that outlined in § 3.5.2, again omitting the tedious algebra, leads to the expression for the stress tensor corresponding to a point force,

$$\begin{aligned}\tilde{\sigma}_{ij}^{\tilde{\boldsymbol{F}}} = \frac{\tilde{F}_3}{4\pi}\int_0^\infty \mathrm{d}\lambda \Bigg[& 2\delta_{ij}\left((A_3 + A_4^k)\frac{\lambda}{\rho}J_1(\lambda\rho) - A_6 J_0(\lambda\rho)\right) \\ & + \delta_{i3}\delta_{j3}\left(\frac{\partial}{\partial x_3}\left(\lambda\frac{\partial A_0}{\partial\lambda} - 2A_0 + 2A_2\right)J_0(\lambda\rho) - 2(A_3 + A_4^k)\frac{\lambda}{\rho}J_1(\lambda\rho)\right)\Bigg] \\ & + \frac{\tilde{F}_\alpha}{4\pi}(\delta_{i3}\delta_{j\alpha} + \delta_{i\alpha}\delta_{j3})\int_0^\infty \mathrm{d}\lambda\frac{\lambda}{\rho}J_1(\lambda\rho)\left(A_3 + A_4^j - \frac{\partial A_1}{\partial x_3}\right) + \mathcal{O}[a], \end{aligned} \tag{3.101}$$

where $A_1, A_2, A_3, A_4^{j,k}, A_6$ are functions of λ, h, H, x_3 given explicitly by Liron and Mochon [121]. Finally, approximating these integrals as before where necessary (assuming uniform convergence of the integrand) and integrating the result against

a slip velocity, the leading-order translational motion is found to be

$$U_1 = \frac{a^2}{H^2}\frac{(B_2 - A_2)}{5}P_2^1(\cos\alpha)\Bigg[-\frac{1}{12}\Big(\zeta\Big[2,\tfrac{h}{H}\Big] - \zeta\Big[2,1-\tfrac{h}{H}\Big]\Big) \\ - \frac{1}{3}\Big(3\tfrac{h}{H}(1-\tfrac{h}{H}) - 1\Big)\Big(\zeta\Big[4,\tfrac{h}{H}\Big] - \zeta\Big[4,1-\tfrac{h}{H}\Big]\Big) \\ - \frac{1}{3}\tfrac{h}{H}\Big(1-\tfrac{h}{H}\Big)\Big(1-2\tfrac{h}{H}\Big)\Big(\zeta\Big[5,\tfrac{h}{H}\Big] + \zeta\Big[5,1-\tfrac{h}{H}\Big]\Big)\Bigg] + \mathcal{O}[a^3] \quad (3.102)$$

$$U_3 = -\frac{a^2}{H^2}\frac{(B_2 - A_2)}{5}P_2(\cos\alpha)\Bigg[\frac{3}{2}\Big(1-2\tfrac{h}{H}\Big)\zeta[3] + \frac{2}{3}\Big(\zeta\Big[2,\tfrac{h}{H}\Big] - \zeta\Big[2,1-\tfrac{h}{H}\Big]\Big) \\ - \frac{3}{4}\Big(1-2\tfrac{h}{H}\Big)\Big(\zeta\Big[3,\tfrac{h}{H}\Big] + \zeta\Big[3,1-\tfrac{h}{H}\Big]\Big) \\ + \frac{1}{12}\Big(33\tfrac{h}{H}(1-\tfrac{h}{H}) - 8\Big)\Big(\zeta\Big[4,\tfrac{h}{H}\Big] - \zeta\Big[4,1-\tfrac{h}{H}\Big]\Big) \\ + \frac{2}{3}\tfrac{h}{H}\Big(1-\tfrac{h}{H}\Big)\Big(1-2\tfrac{h}{H}\Big)\Big(\zeta\Big[5,\tfrac{h}{H}\Big] + \zeta\Big[5,1-\tfrac{h}{H}\Big]\Big)\Bigg] + \mathcal{O}[a^3]. \quad (3.103)$$

Once again using eq. (3.100) these expressions coincide with the one-wall results, eqs. (3.23) and (3.24), in the limit $H \to \infty$. The magnitude of the translation speed is shown for a variety of gap widths in fig. 3.11. As can be seen in these figures, the motion changes sign as the swimmer's position crosses the centre of the channel, as may be verified by exchanging h and $H - h$ in eqs. (3.102) and (3.103). This is a consequence of the head-tail symmetry of the squirming modes A_2 and B_2.

To this level of approximation the propulsive modes A_1, B_1 do not result in any interaction with the plates. However, adding a self-propulsion speed in the direction of the head's orientation α it is possible to write evolution equations for a squirmer. Trajectories of two such squirmers, a puller and a pusher, are shown in figs. 3.12 and 3.13 respectively. While the pusher rapidly crashes into one of the two plates, the puller travels for a longer distance along the channel before crashing or settling into the stable trajectory parallel to the plates in the middle of the channel. The existence of such a trajectory was also reported by the numerical study of de Graaf et al. [163], who included higher-order singularities in order to avoid collisions with the wall and found oscillatory behaviour down the channel observed *in vivo* by Jana et al. [161].

The inset of fig. 3.13 shows the evolution of orientation along a trajectory for a pusher and a puller. The pusher reorients itself so the head-tail axis is parallel to the plates; the drawing in of fluid perpendicular to this axis results in attraction to the nearest plate, and also means swimming parallel to the plates is unstable.

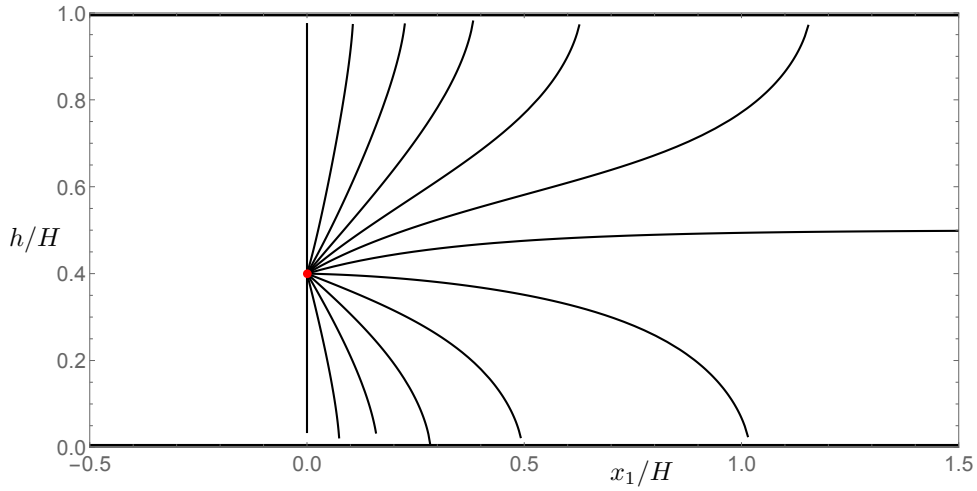

Figure 3.12: Trajectories of a contractile swimmer of radius $a = 0.01H$ between two plates for initial orientation $\alpha(t = 0) = n\pi/12, n \in \{1, 2, \ldots, 12\}$. As found by de Graaf et al. [163] pullers have a stable trajectory along the middle of the channel.

In contrast the puller exhibits a stable trajectory parallel to the plates because the expulsion of fluid normal to the swimming direction pushes it away from the plates. Otherwise, the orientation tends to evolve so that the head-tail axis is normal to the plates, resulting in collision.

Despite the lack of mathematical rigour, the approach demonstrated in this section has given valuable results, which reduce to the expected expressions when one of the plates is taken infinitely far away. Furthermore the behaviour found, and illustrated in figs. 3.12 and 3.13, compares favourably to that found in the detailed numerical study of de Graaf et al. [163]. We nevertheless emphasise that these results are preliminary, in particular assuming that the integrals performed are uniformly convergent and can thus be approximated in the way shown. More careful analysis is required to check the swimming behaviour in a channel. Numerical integration could be used to provide a better estimate, while the collision dynamics with the plates could be investigated more thoroughly by including the source-dipole term to the integration kernel to more accurately represent the swimmer's shape.

3.6 Discussion

The reciprocal theorem provides a simple and effective technique for harnessing solutions to the Stokes equations to calculate swimmer interactions. While the description obtained is only approximate, the fast decay of the higher-order terms that

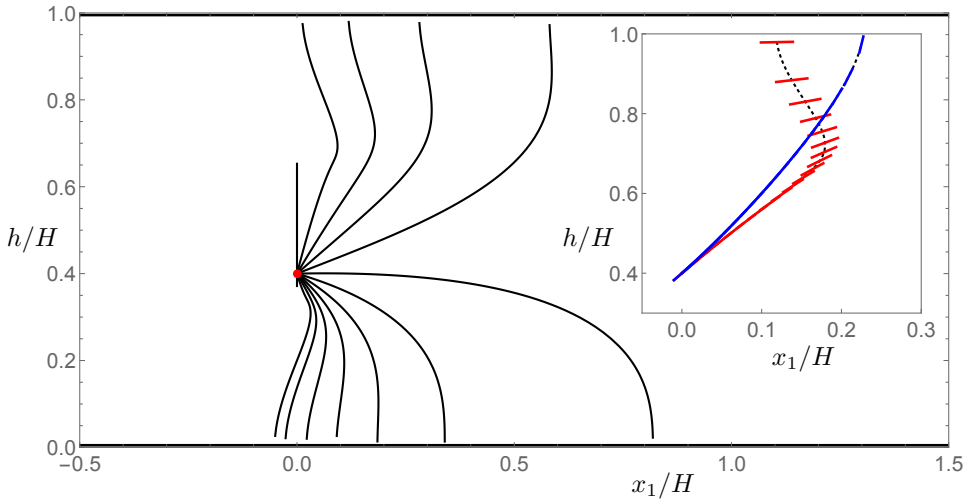

Figure 3.13: Trajectories of an extensile swimmer of radius $a = 0.01H$ between two plates for initial orientation $\alpha(t = 0) = n\pi/12, n \in \{1, 2, \ldots, 12\}$. There is strong wall attraction, as reported elsewhere for extensile swimmers [65]. When the swimmer is aligned with the wall normal there are two fixed points where the self-propulsion speed matches the repulsive effect of the stresslet. By symmetry, these are the same distance from the nearest plate (in this case, at $h = 0.653H, h = 0.347H$). Inset: trajectories of an extensile (red) and a contractile (blue) swimmer with the same boundary condition, showing evolution of orientation. The puller aligns with the wall normal, while the pusher aligns parallel to the wall, as reported elsewhere [47, 65]. The attraction to the wall of the extensile swimmer is perpendicular to the swimming direction, resulting in the kinked trajectory.

describe microscopic detail means that the agreement is good up to a small number of body sizes from the swimmer; indeed, even for an organism like *Chlamydomonas*, which propels itself by beating a pair of flagellae of length comparable to its body and therefore is not readily described as a squirming sphere, Drescher et al. [130] find that microscopic detail only becomes important at a distance of less than seven body sizes (with the caveat that the flow outside this near-field region is at most 1% of the magnitude at the swimmer's surface and therefore almost negligible).

Here two Stokes drag solutions have been used, namely Blake & Chwang's classic image systems for a point force and torque near an infinite plane [147], and Liron's solution for a Stokeslet between two parallel plates [121], which is here supplemented by the analogous rotlet, an apparently new result. The interaction with a plane represents the most basic of possible interactions, as well as being of interest in its own right; furthermore an object larger than a swimmer can be expected to act as a wall if the separation is smaller than the object's size. The motion between parallel plates is relevant for the variety of experiments that are

confined between two microscope slides [37, 45, 47] and has as a limit the interaction with a single wall, meaning the effect of increasing confinement is easy to assess by comparison.

Several other existing solutions lend themselves to the treatment demonstrated in this chapter. In particular, the solution for a Stokeslet outside a sphere by Oseen, later reproduced by Higdon [70], could be used to calculate interactions between swimmers, providing an alternative to the multipole expansions of Ishikawa et al. [67]. The solution for point singularities near a fluid interface [122, 123] could be used to calculate the swimming near a free surface, which has been examined in two dimensions using conformal maps [83] and in three using multipole expansions [18] or numerics [149], and may be particularly relevant for understanding biofilm formation [49]. Finally, there exists a solution for pipe flow due to a Stokeslet [124]. If a corresponding solution for the rotlet could be found in this geometry, as was done for the flow between two plates here, we would have a powerful tool for investigating swimming or transport in a pipe, of potential relevance to problems in medicine, particularly fertility [126] and respiratory disease [125]; this problem has attracted attention recently [163, 165], and the reciprocal theorem provides a useful way to attack it, although, regrettably, not in this thesis.

4

Exact solutions in two dimensions

Chapter 3 showed how the reciprocal theorem can be used to find approximate results for the interaction. However it is also valuable in obtaining exact solutions. We first demonstrate this in two dimensions, where a complete solution is available, and then extend to three. We look at the motion of a swimming disc in geometric confinement. We shall solve two cases: firstly, the interaction with a wall; then, inside a fluid region of finite volume with a circular boundary. Finally, interaction between two discs in an infinite fluid is discussed but not solved, due to mathematical issues with the conjugate solution.

4.1 Hydrodynamics in two dimensions

This chapter will explore some exact results in two dimensions using the reciprocal theorem and the classic solutions for a pair of discs in Stokes flow [107, 117]. There is a precedent for these results in the work of Crowdy, who inspired this research [81, 82], although here we make some generalisations of the geometry, and consider an arbitrary axisymmetric swimmer model. The conjugate solution had first been derived independently [166] and later related to that of Jeffrey and Onishi [107].

As well as conferring significant computational convenience, allowing study of problems that are intractable in higher dimensions, working in two dimensions is

appropriate in a number of regimes, such as those confined to a fluid surface [167] or in a thin planar region. There is a relatively small but wide-ranging literature of active swimming problems in two dimensions. A notable example is Crowdy's point-singularity model of swimmer near a wall [127, 140] which reproduced and explained the observed trajectories of a robotic floating swimmer [28, 168]. This model was later solved exactly [81]. Other examples include swimming under a free surface [83], near a corner [128] or gap in a wall [169] and inside a semi-infinite strip [139]. As well as the two-dimensional version of the squirmer model [78], other propulsion mechanisms studied explicitly include self-electrophoresis [94, 99], self-diffusiophoresis [82] and mixed stress and slip boundary conditions [170]. Studies of deforming two-dimensional bubbles [171, 172] have been used to study the hydrodynamics of cells with changing shape [173].

It is common to formulate two-dimensional problems using complex analysis [148], with space described by the complex coordinate z and its conjugate $\overline{z}$,

$$z \equiv x_1 + \mathrm{i}x_2, \qquad \overline{z} \equiv x_1 - \mathrm{i}x_2. \tag{4.1}$$

Under this formalism a vector is described by a complex number, with the components of the vector in the Cartesian directions given by its real and imaginary parts. If we have two vectors $\boldsymbol{a}, \boldsymbol{b}$ represented by the complex numbers a, b then their scalar and vector products are given by

$$\begin{aligned} \overline{a}b &= (\mathrm{Re}[a]\mathrm{Re}[b] + \mathrm{Im}[a]\mathrm{Im}[b]) + \mathrm{i}(\mathrm{Re}[a]\mathrm{Im}[b] - \mathrm{Re}[b]\mathrm{Im}[a]) \\ &\equiv \boldsymbol{a}\cdot\boldsymbol{b} + \mathrm{i}(\boldsymbol{a}\times\boldsymbol{b})_3. \end{aligned} \tag{4.2}$$

The generalisation of eq. (4.2) to three dimensions led Hamilton to his discovery of the quaternions [148]. Since $\boldsymbol{a}$ and $\boldsymbol{b}$ are coplanar their cross product is purely in the $\boldsymbol{e}_3$ direction. Hence when working with this representation of vectors as complex numbers vector products will be written as scalars.

For a two-dimensional flow $(u, v, 0)$, here written $u + \mathrm{i}v$, incompressibility is identically satisfied for all flows that are the curl of the field $(0, 0, \psi)$ such that

$$u = -\frac{\partial\psi}{\partial x_2}, \qquad v = \frac{\partial\psi}{\partial x_1}. \tag{4.3}$$

(although not all flows may be represented in this way – for example, any flow containing sources or sinks of fluid is not divergence-free everywhere). The scalar quantity ψ is called the streamfunction [174].

Taking the curl of the Stokes equations, eq. (1.1), gives

$$\boldsymbol{\nabla} \times \nabla^2 \boldsymbol{u} = \nabla^2(\boldsymbol{\nabla} \times (\boldsymbol{\nabla} \times \boldsymbol{\psi})) = \nabla^2(\boldsymbol{\nabla}(\boldsymbol{\nabla} \cdot \boldsymbol{\psi})) - \nabla^2\nabla^2\boldsymbol{\psi} = \mathbf{0}. \tag{4.4}$$

Therefore in two dimensions the Stokes equations reduce to the scalar biharmonic equation,

$$\nabla^4 \psi \equiv \nabla^2\nabla^2\psi = 0, \tag{4.5}$$

provided the streamfunction is divergence-free, which in this case means $\partial_{x_3}\psi = 0$, obviously true for any scalar streamfunction depending only on x_1 and x_2.

The solution of the biharmonic equation is found as follows. The Laplacian of the streamfunction must be harmonic,

$$\nabla^2\psi = 4\partial_z\partial_{\overline{z}}\psi = a(z) + b(\overline{z}), \tag{4.6}$$

for some analytic functions $a(z)$ and $b(z)$ [148]. Integrating successively with respect to $\overline{z}$ and z gives

$$2\partial_z\psi = \overline{z}a(z) + B(\overline{z}) + c(z) \tag{4.7}$$

$$\implies \psi = \frac{1}{2}\Big(\overline{z}A(z) + zB(\overline{z}) + c(z) + d(\overline{z})\Big), \tag{4.8}$$

where A, B are the antiderivatives of a, b, and c, d are arbitrary analytic functions. Hence the general solution of the biharmonic equation depends on four functions. Finally, the requirement that the streamfunction be real removes two degrees of freedom, and it is conventional [175] to write the streamfunction as

$$\psi(z, \overline{z}) = \mathrm{Im}\Big[\overline{z}f(z) + g(z)\Big]. \tag{4.9}$$

The analytic functions $f(z)$ and $g(z)$ are called the *Goursat functions*. Once these have been determined for a given flow the problem is solved, since from them all other quantities of interest can be derived [175] as

$$\frac{p}{\mu} - \mathrm{i}\omega = 4f'(z), \qquad u + \mathrm{i}v = -f(z) + z\overline{f'}(\overline{z}) + \overline{g'}(\overline{z}), \tag{4.10}$$

where p is the pressure and ω is the vorticity,

$$\boldsymbol{\omega} \equiv \boldsymbol{\nabla} \times \boldsymbol{u}, \tag{4.11}$$

and where we have used the Schwarz conjugate,

$$\overline{b}(z) \equiv \overline{b(\overline{z})}. \tag{4.12}$$

The stress tensor may be formed explicitly by combining the pressure and flow using eq. (1.2). However, in problems involving immersed objects it is more useful to define the stress normal to a boundary S, or, equivalently, the force per unit length along S. This is a vector, which may be written as a derivative with respect to arclength along S [81] as

$$(\boldsymbol{\sigma}\cdot\hat{\boldsymbol{n}}_S)_1 + \mathrm{i}(\boldsymbol{\sigma}\cdot\hat{\boldsymbol{n}}_S)_2 = 2\mu\mathrm{i}\frac{\mathrm{d}h}{\mathrm{d}S}, \quad \text{where} \tag{4.13}$$

$$h(z,\overline{z}) \equiv f(z) + z\overline{f'}(\overline{z}) + \overline{g'}(\overline{z}). \tag{4.14}$$

We comment briefly on the nature of the singularities in the Goursat functions associated to forces and torques in two dimensions, which may be determined from the stress tensor, (4.13). Since eq. (4.13) is a total derivative the total force F_S on S is given by

$$F_S = \{2\mu\mathrm{i}h(z,\overline{z})\}_S = \{4\mu\mathrm{i}f(z)\}_S, \tag{4.15}$$

where the curly braces indicate the change in the enclosed quantity over an anti-clockwise circuit of S. The second equality is deduced noticing that, within the fluid,

$$h(z,\overline{z}) = 2f(z) + u + \mathrm{i}v. \tag{4.16}$$

Then, since the fluid velocity must be single-valued everywhere in the fluid region, the force is simply the sum of the jumps in the value of f across the branch cuts that are traversed on a circuit. It can also be shown by similar arguments [81] that the torque T_S about a point z_0, on an object with boundary S is given by

$$T_S = 2\mu\mathrm{Re}\int_S (z-z_0)g''(z)\,\mathrm{d}z - 2\mu\mathrm{Re}\{\overline{z_0}f(z)\}_S. \tag{4.17}$$

The first term records any point torques in the fluid, while the second term accounts for the couple induced by point forces [127].

4.1.1 The reciprocal theorem

In two dimensions the reciprocal theorem takes precisely the same form as in three,

$$\sum_j \mathrm{Re}[U_j\overline{\tilde{F}_j}] + \mathrm{Re}[\Omega_j\overline{\tilde{T}_j}] = -\sum_j \mathrm{Re}\left[2\mu\mathrm{i}\int_{S_j}\overline{u_{sj}}\frac{\mathrm{d}\tilde{h}}{\mathrm{d}S}\mathrm{d}S\right]. \tag{4.18}$$

Here S_j denote the boundary components of the fluid with normal vector $\hat{\boldsymbol{n}}_S$, and $\mathrm{d}S$ is the arclength along these boundaries. Writing the right-hand side of eq. (4.18) in this way allows it to be integrated by parts and evaluated with the residue theorem, provided an appropriate conjugate solution is known, encoded in the function $\tilde{h}$, which corresponds to the normal stress due to forces $\tilde{F}_j$ and torques $\tilde{T}_j$.

In what follows S shall be taken to be the boundary of a disc centred at the point z_0, with an axisymmetric slip velocity u_s decomposed into Fourier modes corresponding to Blake's squirming set [78]. If u_r and u_θ are the radial and tangential components of u_s, then the specification is in terms of the real coefficients $A_n, B_n, n \geq 1$, so that

$$u_r = \sum_{n=0}^{\infty} A_n \cos n(\theta - \alpha), \qquad u_\theta = \sum_{n=1}^{\infty} B_n \sin n(\theta - \alpha). \tag{4.19}$$

The angle α specifies the direction of the swimmer's head-tail axis; this and the polar angle θ are measured from the real axis so that

$$\mathrm{e}^{\mathrm{i}\theta} = \frac{(z - z_0)}{|z - z_0|}, \tag{4.20}$$

allowing the complex form of the slip velocity to be written as

$$u_s = (u_r + \mathrm{i}u_\theta)\frac{(z - z_0)}{|z - z_0|}. \tag{4.21}$$

4.2 The conjugate two-disc problem

The solution for the motion of two discs in two-dimensional Stokes flow is a well-established result. Jeffery [117] solved the flow about two rotating discs; this was supplemented by Jeffrey and Onishi [107], who also found the flow due to translation, with a particular focus on the limit where one of the discs is infinite in radius and becomes a plane boundary. This solution was independently rediscovered using conformal mapping techniques by Tchieu et al. [166], and later identified with the Jeffrey-Onishi result for the interaction of a disc with a plane boundary [81]. Here we derive the same solution in the same way as Crowdy [81], but generalise to two discs in an arbitrary configuration, including where one encloses the other, and present the solution in terms of the two-dimensional fundamental singularities of viscous flow [127], which allows the result to be related to analogous and well-known results in three dimensions [147].

We consider two non-slip discs of radii $r_{1,2}$, as shown in fig. 4.1, centred at

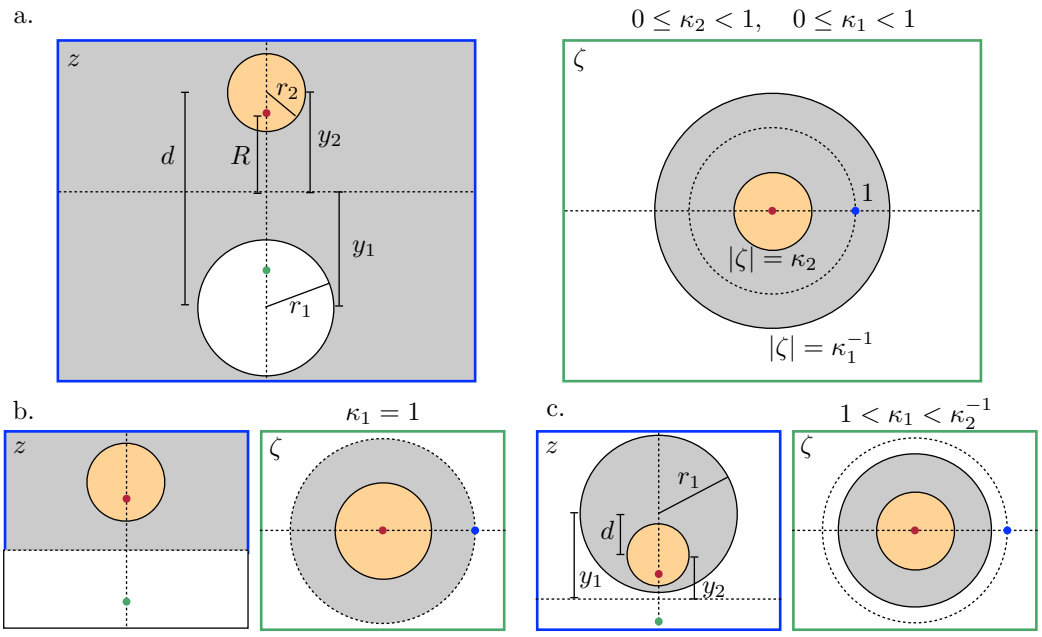

Figure 4.1: The conformal map between the z plane and the ζ plane used in this chapter. Regions in one plane map to regions of the same colour in the other, with the coloured frames representing infinity. Three distinct geometries are available from this conformal map: two external discs (a), a disc in the half-space (b) and two nested, non-overlapping discs (c). In the latter two cases the integration contour used to calculate force or torque is equivalent for both boundaries, up to a sign difference, since it does not enclose the singular point $\zeta = 1$. Therefore the force and torque on each boundary must be equal and opposite.

the points $z_{1,2}$ separated by a distance d. They are dragged by forces $\tilde{F}_{1,2}$ and torques $\tilde{T}_{1,2}$, resulting in translational velocities $\tilde{U}_{1,2}$ and angular velocities $\tilde{\Omega}_{1,2}$. Then, in the rest frame of the fluid, the flows on the surfaces of the discs correspond to translation plus rotation, and are given by

$$\tilde{u} + \mathrm{i}\tilde{v} = \begin{cases} \tilde{U}_1 + \mathrm{i}\frac{(z-z_1)}{r_1} r_1 \tilde{\Omega}_1 & \text{on} \quad |z - z_1|^2 = r_1^2, \\ \tilde{U}_2 + \mathrm{i}\frac{(z-z_2)}{r_2} r_2 \tilde{\Omega}_2 & \text{on} \quad |z - z_2|^2 = r_2^2. \end{cases} \tag{4.22}$$

These boundary conditions determine the Goursat functions $f(z)$ and $g(z)$ on the surfaces of the discs. Then, since $f(z)$ and $g(z)$ are holomorphic functions they are determined by analytic continuation into the fluid domain.

4.2.1 Conformal map

A conformal transformation is one that is locally angle preserving, which is to say that the Jacobian of the corresponding coordinate transformation is a scalar function times a rotation matrix. While in $d > 2$ Liouville's theorem limits the conformal transformations to homotheties, isometries and inversions, in two dimensions any analytic function defines a conformal transformation. These are of great use in two-dimensional fluid mechanics in simplifying boundary conditions. Possibly the most famous example is that of the flow around an airplane wing, in which a conformal transformation maps the flow about an airfoil, with nontrivial shape, to the much simpler case of flow about a rotating cylinder. Further examples abound in the literature on Stokes flows about bubbles, slits and with mixed boundary conditions [171, 172, 176, 177]. Darren Crowdy in particular has in recent years applied conformal transformation to a great variety of swimmer problems, such as the flow past a wall with a gap [138] with application to swimming near such a structure [169], exact solutions for a circular swimmer [81] and self-diffusiophoretic disc [82] near a wall, swimming underneath a free surface [83], near a corner [128] and in a semi-infinite strip [139]. These often rely on the point-singularity description outlined in Crowdy and Or [127] as an approximation of the swimming stroke, modelling the force dipole contribution that is common to force-free swimmers. Some examples by other authors also exist. For instance Squires and Bazant [99] find solutions for the swimming of chemically-propelled objects with non-trivial (simply connected) shape by relating them to solutions for a disc using conformal transformations, a procedure guaranteed by the Riemann mapping theorem.

Here the conformal transformation used is the definition of bipolar coordinates, which will be outlined in more depth in Chapter 5. The standard polar grid is the stereographic projection of the lines of latitude and longitude on S^2 onto the plane about one of the poles, whereas the bipolar grid is a stereographic projection of the same lines of latitude and longitude about an equatorial point. Hence the two coordinate systems are related by a solid rotation in three-dimensional space. Any pair of lines of latitude, when projected thus, become two non-concentric circles on the plane, with one enclosing the other if they originated on the same hemisphere of the globe. Thus any pair of circles may be related to concentric circles. More technically, the fluid region between two non-concentric discs is conformally equivalent to a twice-punctured plane, and any such region is conformally equivalent to an annulus [119].

Given any pair of circles in the plane, there exist two points on their common diameter that map to each other under inversion in the circles. If the circles are

concentric these two points are their common centre and infinity. We take their common diameter to be the imaginary axis and define the z coordinate by placing these two points at $z = \pm \mathrm{i}R$, where R is real. The Möbius transformations

$$z(\zeta) = -\mathrm{i}R\frac{\zeta+1}{\zeta-1} \quad \text{and} \quad \zeta(z) = \frac{z-\mathrm{i}R}{z+\mathrm{i}R}, \tag{4.23}$$

map the family of circles which relate the points $z = \pm \mathrm{i}R$ under inversion to the family of concentric circles about $\zeta = 0$, with the real line mapped to the unit circle and infinity to $\zeta = 1$.

Then, if a circle of radius r_1 located at z_1 maps to the circle $|\zeta| = \kappa_1^{-1}$ and another circle or radius r_2 and centre z_2 to $|\zeta| = \kappa_2$, with $0 \leq \kappa_1$ and $0 \leq \kappa_2 \leq 1$, we derive the geometry in z space as

$$\begin{aligned} r_{1,2} &= \left|\frac{2R\kappa_{1,2}}{1-\kappa_{1,2}^2}\right|, \qquad y_{1,2} = R\frac{1+\kappa_{1,2}^2}{1-\kappa_{1,2}^2}, \\ z_1 &= -\mathrm{i}y_1, \qquad z_2 = \mathrm{i}y_2, \qquad d \equiv y_1 + y_2, \end{aligned} \tag{4.24}$$

as illustrated in figure 4.1(a). In the limit $\kappa_i \to 1$ disc i becomes an infinite wall (figure 4.1(b)), while if $\kappa_1 > 1$ the fluid in the z plane is now the region between two non-concentric nested circular boundaries (figure 4.1(c)).

The fluid region must be free of singularities. Hence in the ζ plane we may only have singularities in $|\zeta| > \kappa^{-1}$, $|\zeta| < \kappa_2$ or at $\zeta = 1$, which is the image of infinity and may therefore have a divergent flow due to the Stokes paradox. When finding the forces and torques acting on two discs this singularity structure means that with $\kappa_1 \geq 1$, corresponding to a half-space or nested circles, the forces and torques must be equal and opposite.

Defining the transformed Goursat functions by

$$\mathcal{F}(\zeta) \equiv f(z(\zeta)), \qquad \mathcal{G}(\zeta) \equiv g'(z(\zeta)), \tag{4.25}$$

the boundary conditions (4.22) transform to

$$-\mathcal{F}(\zeta) + z(\zeta)\frac{\overline{\mathcal{F}}'(\overline{\zeta})}{\overline{z}'(\overline{\zeta})} + \overline{\mathcal{G}}(\overline{\zeta}) = \begin{cases} \tilde{U}_1 + \mathrm{i}(z(\zeta) - z_1)\tilde{\Omega}_1 & \text{on } |\zeta| = \kappa_1^{-1}, \\ \tilde{U}_2 + \mathrm{i}(z(\zeta) - z_2)\tilde{\Omega}_2 & \text{on } |\zeta| = \kappa_2. \end{cases} \tag{4.26}$$

The problem is therefore to find $\mathcal{F}$ and $\mathcal{G}$, which may then be transformed back to give f and g. Using eq. (4.23), eqs. (4.26) are transformed to the ζ plane as conditions on the circles parametrised by $\overline{\zeta} = 1/\kappa_1^2\zeta$ and $\overline{\zeta} = \kappa_2^2/\zeta$, which are

analytically continued to the entire domain, so that

$$-\mathcal{F}(\zeta)+z(\zeta)\frac{\overline{\mathcal{F}}'(1/\kappa_1^2\zeta)}{\overline{z}'(1/\kappa_1^2\zeta)}+\overline{\mathcal{G}}\Big(\frac{1}{\kappa_1^2\zeta}\Big)=\tilde{U}_1+\mathrm{i}(z(\zeta)-z_1)\tilde{\Omega}_1 \tag{4.27}$$

$$-\mathcal{F}(\zeta)+z(\zeta)\frac{\overline{\mathcal{F}}'(\kappa_2^2/\zeta)}{\overline{z}'(\kappa_2^2/\zeta)}+\overline{\mathcal{G}}\Big(\frac{\kappa_2^2}{\zeta}\Big)=\tilde{U}_2+\mathrm{i}(z(\zeta)-z_2)\tilde{\Omega}_2. \tag{4.28}$$

We rescale 4.27 by $\zeta\to\zeta/\kappa_1^2$ and 4.28 by $\zeta\to\kappa_2^2\zeta$, and subtract them to eliminate $\mathcal{G}(\zeta)$, giving the condition

$$\begin{aligned}&\mathcal{F}(\zeta/\kappa_1^2)-\mathcal{F}(\kappa_2^2\zeta)+\frac{(1-\kappa_1^2\kappa_2^2)(\zeta-1)^2}{\zeta(\zeta-\kappa_1^2)(\kappa_2^2\zeta-1)}\overline{\mathcal{F}}'\Big(\frac{1}{\zeta}\Big)\\ &=\tilde{U}_2-\tilde{U}_1+2R(\zeta-1)\Big(\frac{\kappa_1^2\tilde{\Omega}_1}{(1-\kappa_1^2)(\zeta-\kappa_1^2)}+\frac{\kappa_2^2\tilde{\Omega}_2}{(1-\kappa_2^2)(\kappa_2^2\zeta-1)}\Big).\end{aligned} \tag{4.29}$$

By (4.27) and (4.28), $\mathcal{G}(\zeta)$ is then given by either of

$$\mathcal{G}(\zeta)=\overline{\tilde{U}}_1-\frac{2\kappa_1^2R(\zeta-1)\tilde{\Omega}_1}{(1-\kappa_1^2)(\kappa_1^2\zeta-1)}+\overline{\mathcal{F}}\Big(\frac{1}{\kappa_1^2\zeta}\Big)+\frac{(\zeta-1)^2(\kappa_1^2\zeta+1)}{2(\kappa_1^2\zeta-1)}\mathcal{F}'(\zeta) \tag{4.30}$$

$$=\overline{\tilde{U}}_2+\frac{2\kappa_2^2R(\zeta-1)\tilde{\Omega}_2}{(1-\kappa_2^2)(\zeta-\kappa_2^2)}+\overline{\mathcal{F}}\Big(\frac{\kappa_2^2}{\zeta}\Big)+\frac{(\zeta-1)^2(\zeta+\kappa_2^2)}{2(\zeta-\kappa_2^2)}\mathcal{F}'(\zeta). \tag{4.31}$$

Finally in order to calculate the mobility matrices we need expressions for the force and torque. Using eqs. (4.15) and (4.17), these are given by

$$F_{1,2}=\mp\{4\mu\mathrm{i}\mathcal{F}(\zeta)\}_{1,2}, \tag{4.32}$$

$$T_{1,2}=2\mu\mathrm{Re}\Big[\int_{1,2}\mathrm{d}\zeta\,(z(\zeta)-z_{1,2})\frac{\mathrm{d}\mathcal{G}(\zeta)}{\mathrm{d}\zeta}\Big]-2\mu\mathrm{Re}\{\overline{z_{1,2}}\mathcal{F}(\zeta)\}_{1,2} \tag{4.33}$$

Note that if $\kappa_1<1$ then under the conformal transformation the boundary of disc 1 is inverted so the integrations to calculate force and torque on this disc change sense and pick up a minus sign.

The general solution to this problem was found by Tchieu et al. [166] to be of the form

$$\mathcal{F}(\zeta)=\mathcal{F}_0\log\zeta+\mathcal{F}_\alpha\zeta+\frac{\mathcal{F}_\beta}{\zeta}+\frac{\mathcal{F}_\gamma}{\zeta-1}, \tag{4.34}$$

by expanding eq. (4.27)-(4.28) in partial fractions and matching to the Goursat functions. Crowdy [81] also used this solution, showing that it is identical to the much older solution by Jeffrey and Onishi [107] in which the conformal transformation, eq. (4.23), was implicit through the use of bipolar coordinates.

What does eq. (4.34) physically correspond to? Without yet evaluating the

unknown constants we may transform back to the z plane to get a better idea of what this flow field is. Combining eq. (4.34) with the conformal map, eq. (4.23) we find the flow field has singularities at the focal points $z = \pm \mathrm{i}R$ and centres $z = z_{1,2}$ of the discs. These singularities are identified with fundamental singularities of Stokes flow and the ansatz may be expressed as a singular part u^* and a part analytic everywhere, u^a. Then,

$$u + \mathrm{i}v = u^* + u^a, \tag{4.35}$$

with the singular flow given by

$$\begin{aligned}
u^* = \mathcal{F}_0 \mathrm{Stokeslet}[z - \mathrm{i}R] - \mathcal{F}_0 \mathrm{Stokeslet}[z + \mathrm{i}R] \\
-2\mathrm{i}R\Big(\mathcal{F}_0 - \frac{\overline{\mathcal{F}_\alpha}}{\kappa_1^2} - \mathcal{F}_\beta \kappa_1^2\Big)\mathrm{Rotlet}[z - \mathrm{i}R] \\
-2\mathrm{i}R\Big(\mathcal{F}_0 + \frac{\mathcal{F}_\alpha}{\kappa_1^2} + \overline{\mathcal{F}_\beta}\kappa_1^2\Big)\mathrm{Rotlet}[z + \mathrm{i}R] \\
+2\mathrm{i}R\Big(\mathcal{F}_0 + \frac{\mathcal{F}_\alpha}{\kappa_1^2} - \mathcal{F}_\beta \kappa_1^2 - \frac{\kappa_1^2 \mathrm{Re}[\mathcal{F}_\gamma]}{(1-\kappa_1^2)^2}\Big)\mathrm{Rotlet}[z - z_1] \\
+2\mathrm{i}R\mathcal{F}_\beta\Big(\mathrm{Stresslet}[z - \mathrm{i}R] - \mathrm{i}R\mathrm{Dipole}[z - \mathrm{i}R]\Big) \\
-2\mathrm{i}R\mathcal{F}_\alpha\Big(\mathrm{Stresslet}[z + \mathrm{i}R] + \mathrm{i}R\mathrm{Dipole}[z + \mathrm{i}R]\Big),
\end{aligned} \tag{4.36}$$

using the definitions of the Stokeslet, rotlet, stresslet and source-dipole listed by Crowdy and Or [127], and the analytic flow by

$$u^a = -\frac{\mathrm{i}\mathrm{Re}[\mathcal{F}_\gamma]}{R}(z - z_1) + \Big[\mathcal{F}_\alpha \frac{1-\kappa_1^2}{\kappa_1^2} - \mathcal{F}_\beta(1-\kappa_1^2) - 2\mathcal{F}_0 \log[\kappa_1]\Big]. \tag{4.37}$$

Although the Jeffery-Jeffrey-Onishi solution is well-established this representation of the flow in terms of point singularities has not appeared elsewhere, and is instructive in understanding the nature of this solution. The structure of eq. (4.36) shows that we have equal and opposite forces on the two discs. This means only relative motions can be calculated using the reciprocal theorem, since the left-hand side of eq. (4.18) gives only $U_2 - U_1$. To calculate absolute motions using the reciprocal theorem a Stokes drag solution with *non-zero* total force is needed. The flow would diverge logarithmically with a strength proportional to the total force, and would therefore have at least a logarithmic singularity of $\zeta = 1$, and its reflections in the boundaries $|\zeta| = \kappa_1^{-1}$ and $|\zeta| = \kappa_2$. This singularity structure involves the Schottky-Klein prime function and its derivatives [178], which arises naturally in several problems relating to elliptic operators in multiply-connected domains [179], in this case the biharmonic equation in the annulus. Several attempts to overcome

Jeffery's paradox [117] rely on placing singularities at infinity that correspond to a non-zero total force and torque [118, 180–182], although this not been related to the more theoretical literature on flow in multiply-connected domains in which the Schottky-Klein prime function arises [178, 179].

We also note from eq. (4.37) that the coefficient $\mathcal{F}_\gamma$ is associated with solid rotation of the entire fluid domain (the imaginary part of $\mathcal{F}_\gamma$ corresponds to a constant streamfunction and does not affect the flow field, so it may be set to zero without loss of generality). This is a valid solution to eq. (4.22), as we shall see later, because at no point have we insisted on an asymptotically decaying flow field, and because the inertia of an infinite volume of fluid is, at zero Reynolds number, negligible. This results in force-free translation and torque-free rotation of one or both of the discs. Furthermore, as the analytic part of the flow field has a constant contribution, we have a potentially non-zero stream at infinity; this is known as Jeffery's paradox [117]. This, again, will be discussed later.

4.3 A swimming disc in a confined geometry, $\kappa_1 \geq 1$

For the confined geometries corresponding to a disc next to a wall or within a circular boundary, shown in figs. 4.1(b,c), the forces and torques are equal and opposite, so only relative motions and rotations in the swimmer problem may be determined. This is not a problem since in these cases one of the boundaries defines a frame of reference. Furthermore, the fact that the fluid is bounded regularises the solution and means the Stokes paradox does not arise.

Combining the ansatz (4.34) with the condition (4.29) determines $\mathcal{F}(\zeta)$ and $\mathcal{G}(\zeta)$, with the frame of reference chosen by setting $\tilde{U}_1 = \tilde{\Omega}_1 = 0$. Then, eqs. (4.32) and (4.33) allow the resistance matrix to be calculated as

$$\begin{bmatrix} \mathrm{Im}[\tilde{F}_2] \\ \mathrm{Re}[\tilde{F}_2] \\ \tilde{T}_2 \end{bmatrix} = 4\pi\mu \begin{bmatrix} M_{11} & 0 & 0 \\ 0 & M_{22} & M_{32} \\ 0 & M_{23} & M_{33} \end{bmatrix} \begin{bmatrix} \mathrm{Im}[\tilde{U}_2] \\ \mathrm{Re}[\tilde{U}_2] \\ \tilde{\Omega}_2 \end{bmatrix}, \tag{4.38}$$

where

$$M_{11} = \frac{1}{\frac{(1-\kappa_1^2\kappa_2^2)}{(1+\kappa_1^2\kappa_2^2)} + \log[\kappa_1\kappa_2]}, \qquad M_{22} = -\frac{\kappa_1\kappa_2}{K}\left(\frac{r_1}{r_2} + \frac{r_2}{r_1}\right), \tag{4.39}$$

$$M_{23} = M_{32} = \frac{(1-\kappa_1^2\kappa_2^2)}{K}\frac{r_2^2}{2R}, \tag{4.40}$$

$$M_{33} = \frac{1}{K}\left(\frac{(1-\kappa_1^2\kappa_2^2)^2}{(1-\kappa_1^2)(1-\kappa_2^2)}r_2^2 + r_1r_2\kappa_1\kappa_2\left(1 + \frac{(1+\kappa_1^2\kappa_2^2)}{(1-\kappa_1^2\kappa_2^2)}\log(\kappa_1\kappa_2)\right)\right), \tag{4.41}$$

and

$$K = (\kappa_1^2\kappa_2^2 - 1) - \kappa_1\kappa_2\left(\frac{r_1}{r_2} + \frac{r_2}{r_1}\right)\log(\kappa_1\kappa_2). \tag{4.42}$$

The resistance matrix is symmetric, which can be proven to be a general property of motion in a viscous fluid using the reciprocal theorem [88] (in linear elasticity this result is called the Maxwell-Betti theorem [93]). For a disc in the half space, given by the limit $\kappa_1 \to 1$ and $r_1 \to \infty$, the mobility matrix is diagonal, with $M_{23} = M_{32} = 0$, as found by Jeffrey and Onishi [107] and Crowdy [81], and its entries are

$$M_{11} = \frac{1}{\frac{(1-\kappa_2^2)}{(1+\kappa_2^2)} + \log(\kappa_2)}, \qquad M_{22} = \frac{1}{\log(\kappa_2)}, \qquad M_{33} = -\frac{(1+\kappa_2^2)}{(1-\kappa_2^2)}r_2^2, \tag{4.43}$$

Armed with this solution, we are now able to apply the reciprocal theorem. Given a disc with surface slip velocities u_s swimming in a force-free and torque-free fashion and transforming the integral (4.18) to the annulus in ζ space, we obtain

$$\begin{aligned}\mathrm{Re}[\tilde{F}_2]\mathrm{Re}[U_2 - U_1] + \mathrm{Im}[\tilde{F}_2]\mathrm{Im}[U_2 - U_1] + \tilde{T}_2(\Omega_2 - \Omega_1) = \\ 4\pi\mu\mathrm{Re}\left[\oint_{|\zeta|=\kappa_2} \overline{u_{s2}}\mathcal{H}_2'(\zeta)\frac{\mathrm{d}\zeta}{2\pi\mathrm{i}}\right]\end{aligned} \tag{4.44}$$

where the stress function $\mathcal{H}_2'(\zeta)$ is related to the Stokes drag solution, using (4.16), by

$$\mathcal{H}_2'(\zeta) = 2\mathcal{F}'(\zeta) + \mathrm{i}z'(\zeta)\tilde{\Omega}_2 = 2\mathcal{F}_\alpha + \frac{2\mathcal{F}_0}{\zeta} - \frac{2\mathcal{F}_\beta}{\zeta^2} - \frac{2(\mathcal{F}_\gamma + R\tilde{\Omega}_2)}{(\zeta-1)^2}. \tag{4.45}$$

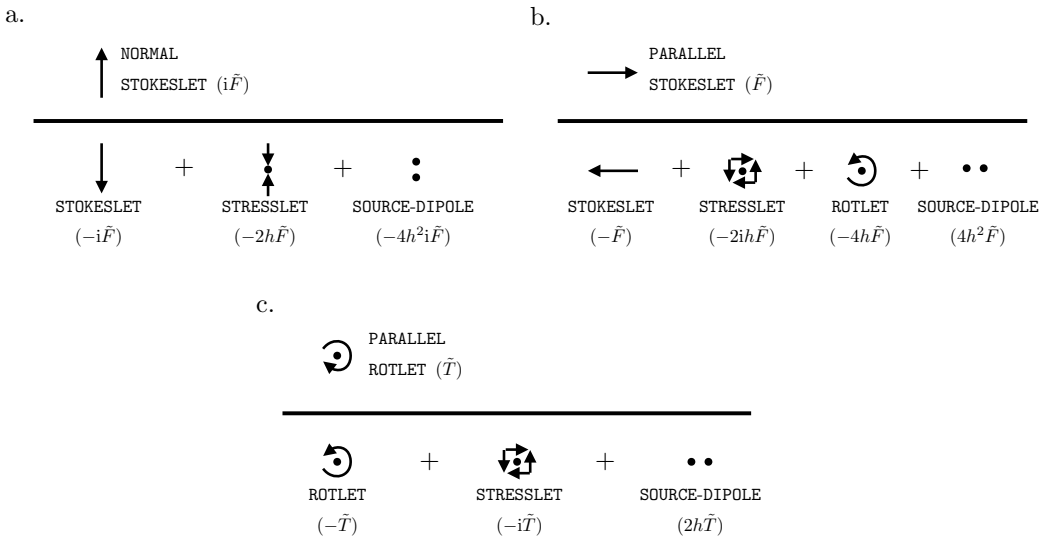

Figure 4.2: The image systems for point force and torque near a wall in two dimensions, after Blake and Chwang [147]. These have the same qualitative structure as their three-dimensional analogues.

Inverting this system we find that the ansatz parameters may be expressed as

$$\begin{gathered}\mathcal{F}_0 = -\frac{\tilde{F}_2}{8\pi\mu}, \quad \mathcal{F}_\gamma = -\frac{R(1-\kappa_1^2\kappa_2^2)}{4\pi\mu r_1^2(1+\kappa_1^2\kappa_2^2)}\tilde{T}_2 - \frac{R^2(1-\kappa_1^2\kappa_2^4)}{2\pi\mu r_1^2(1-\kappa_2^2)(1+\kappa_1^2\kappa_2^2)}\mathrm{Re}[\tilde{F}_2] \\ \mathcal{F}_\alpha = \frac{\kappa_1^2}{\kappa_2^2}\overline{\mathcal{F}_\beta} = \frac{\kappa_1^2}{8\pi\mu(1+\kappa_1^2\kappa_2^2)}\left(\tilde{F}_2 - \frac{2\mathrm{Re}[\tilde{F}_2]}{(1-\kappa_2^2)} - \tilde{T}_2\right)\end{gathered} \tag{4.46}$$

and the disc's rotation is

$$\tilde{\Omega}_2 = -\frac{(1-\kappa_1^2\kappa_2^2)^2}{4\pi\mu\kappa_1 r_1(1-\kappa_2^2)(1+\kappa_1^2\kappa_2^2)}\mathrm{Re}[\tilde{F}_2] - \frac{(1-\kappa_1^2\kappa_2^2)(r_1^{-2}+r_2^{-2})}{4\pi\mu(1+\kappa_1^2\kappa_2^2)}\tilde{T}_2. \tag{4.47}$$

In the half-space $r_1 \to \infty$ so $\mathcal{F}_\gamma \to 0$. Hence the flow field may be described purely in terms of flow singularities as in eq. (4.36). Furthermore in the limit $\kappa_2 \to 0$ we obtain the two-dimensional analogues of the image systems for point forces and torques near a wall originally given by Blake and Chwang [147] (although this is a rather convoluted way to obtain this result: a procedure for a direct calculation of these image systems was given by Crowdy and Or [127], who used it to find the interaction of a stresslet with a wall and model the swimming of a particular floating robotic device [28]). These image systems are illustrated schematically in fig. 4.2.

Now introducing a squirming set on the surface of the disc, as in eq. (4.19), where α denotes the angle the swimmer's head-tail axis makes with the real line,

evaluation of the integral (4.44) gives the motions

$$\mathrm{Re}[U_2] = \sum_n \kappa_2^{n-1}\left[\left(\frac{2\kappa_2^2(1-\kappa_1^2)}{(1+\kappa_1^2\kappa_2^2)} - n(1+\kappa_2^2)\right)A_n + n\frac{(1-\kappa_1^2\kappa_2^2)(1+\kappa_2^2)}{(1+\kappa_1^2\kappa_2^2)}B_n\right]\sin n\Big(\alpha+\frac{\pi}{2}\Big) \tag{4.48}$$

$$\mathrm{Im}[U_2] = \sum_n \kappa_2^{n-1}\left[\left(\frac{2\kappa_2^2(1+\kappa_1^2)}{(1+\kappa_1^2\kappa_2^2)} + n(1-\kappa_2^2)\right)A_n - n\frac{(1-\kappa_1^2\kappa_2^2)(1-\kappa_2^2)}{(1+\kappa_1^2\kappa_2^2)}B_n\right]\cos n\Big(\alpha+\frac{\pi}{2}\Big) \tag{4.49}$$

$$\Omega_2 = \sum_n \frac{2\kappa_2^n}{r_2}\left[\left(n - \frac{(1-\kappa_1^2\kappa_2^2)}{(1+\kappa_1^2\kappa_2^2)}\right)A_n + \left(1 - n\frac{(1-\kappa_1^2\kappa_2^2)}{(1+\kappa_1^2\kappa_2^2)}\right)B_n\right]\sin n\Big(\alpha+\frac{\pi}{2}\Big) \tag{4.50}$$

The results we give here extend the analysis of Crowdy [81], who considered a disc with surface activity corresponding to the squirming mode B_2 near a wall, to arbitrary squirming motions and to arbitrary geometries with $\kappa_1 \geq 1$.

4.3.1 Dynamics

Now we may transform back to real space and find the trajectories corresponding to these evolution equations. We will consider the case of a wall and a concave boundary separately, since different coordinate systems are convenient for each. For a wall we have

$$R = \sqrt{y^2 - r_2^2}, \qquad \kappa_2 = \frac{y - \sqrt{y^2 - r_2^2}}{r_2}, \qquad \kappa_1 = 1$$
$$U_2 = \dot{x} + \mathrm{i}\dot{y}, \qquad \Omega_2 = \dot{\alpha} \tag{4.51}$$

where x, y are the Cartesian coordinates parallel and normal to the wall.

For a concave boundary of radius r_1 we define the swimmer's position using the polar coordinate (d, ϕ) relative to the centre of the tank. The motion can only depend on the orientation relative to the radius, so we must replace α by $\alpha - \phi$.

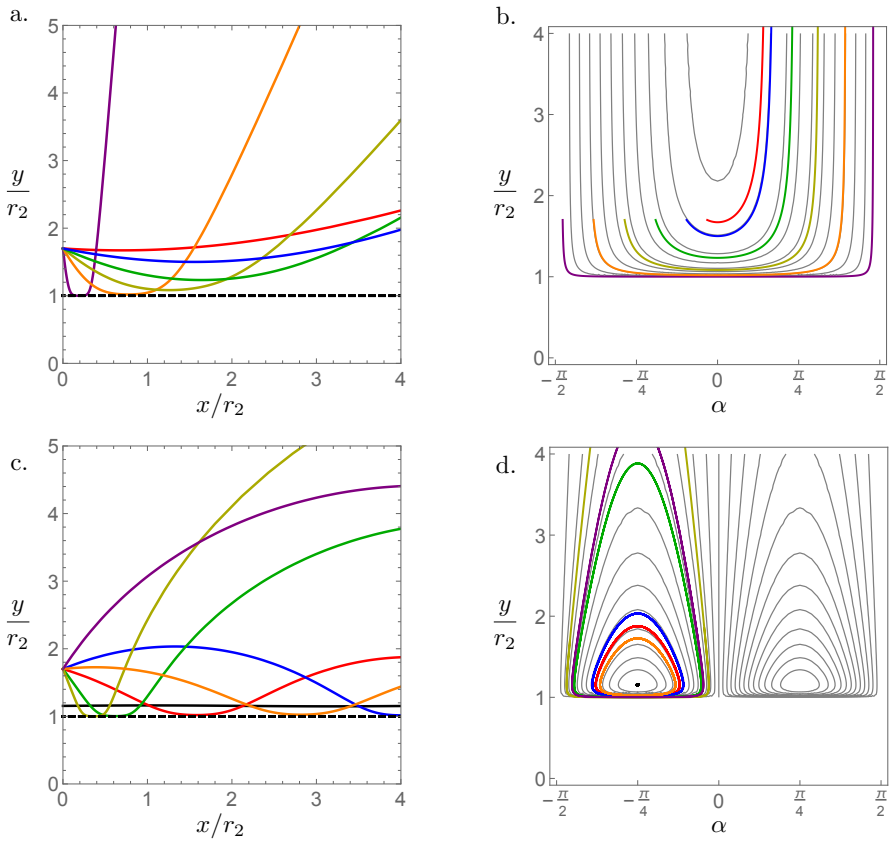

Figure 4.3: (a) Trajectory of a squirmer with $B_1 = 1$ in real space for a variety of initial conditions. (b) Trajectories in phase space. (c) Trajectory of a squirmer with $B_2 = 1$ in real space for a variety of initial conditions. (d) Trajectories in phase space, showing the periodic orbits reported by Crowdy [81].

Finally, to transform the motions to real space we use

$$\begin{aligned} R &= \frac{\sqrt{d^4 + r_1^4 + r_2^4 - 2(d^2 r_1^2 + d^2 r_2^2 + r_1^2 r_2^2)}}{2d}, \\ \kappa_{1,2} &= \pm \frac{d^2 + r_{1,2}^2 - r_{2,1}^2 + \sqrt{d^4 + r_1^4 + r_2^4 - 2(d^2 r_1^2 + d^2 r_2^2 + r_1^2 r_2^2)}}{2d r_{1,2}}, \\ U_2 &= d\dot{\phi} - \mathrm{i}\dot{d}, \qquad \Omega_2 = \dot{\alpha}. \end{aligned} \tag{4.52}$$

A detailed analysis of these dynamical systems could at this point follow, in the spirit of Or and Murray [28] and Crowdy [81], and indeed would be straightforward, given the solution (4.50); we feel this is not an undertaking likely to lead to tremendous insight into general squirmer behaviour. Instead we attempt to characterise the behaviour by exploring a number of trajectories for specific examples.

The behaviour of a swimmer with the tangential modes B_1 and B_2 is shown in fig. 4.3. In the former case, which gives self-propulsion, the interaction with the wall is short-ranged and leads to deflection and scattering for all initial configurations except those with an initial orientation exactly normal to the wall, as can be seen in the phase portrait, fig. 4.3(b). B_2 on the other hand, the surface activity studied by Crowdy [81], shows periodic bound trajectories, as had also been earlier predicted by point-singularity models [127] and seen in a particular floating robotic swimmer [28].

Since the radial modes A_1 and A_2 correspond to deformations it is physically unrealistic for them to take a constant value. Instead we consider the simplest possible activity with these contributions oscillating: a squirmer of unit radius deforming to a side-to-side to a shape somewhat resembling a jelly-bean, as shown in fig. 4.4(a) on page 78, with a radial slip velocity

$$u_r = 0.1 \sin \omega_1 (t - \pi) \sin(\theta - \alpha) + 0.2 \sin 2\omega_1 (t - \pi/2) \sin 2(\theta - \alpha). \tag{4.53}$$

While time-averaging this would result in zero activity, the interaction with the wall causes a gradual realignment of the swimmer's axis parallel to the wall and eventual collision for all initial conditions examined. Two of these trajectories, both in real space and in parameter space, are shown in fig. 4.4(b),(c) and fig. 4.4(d),(e), and demonstrate a drift towards the wall. In this case a more detailed treatment of an explicitly deforming boundary is needed to determine the accuracy of the slip velocity, since the deformation has been taken to be only one order of magnitude smaller than the swimmer's size; in three dimensions the slip velocity due to radial deformations of such large size is not well-described by the linearised description used here [183]. Studies of a deforming bubble in Stokes flow would provide a way to do this [171, 172].

A more biologically realistic model is Blake's swimmer [78], undergoing a short-wavelength, periodic deformation of the shape,

$$r_s(t) = a\Big[1 + \epsilon \sum_{n\geq 2} \mathcal{A}_n(t) \cos n(\theta - \alpha)\Big], \quad \theta_s(t) = \theta + \epsilon \sum_{n\geq 1} \mathcal{B}_n(t) \sin n(\theta - \alpha), \tag{4.54}$$

with

$$\begin{aligned} \mathcal{A}_N &= \frac{\epsilon_1}{\epsilon} \cos \nu t, \qquad \mathcal{A}_{N+1} = \frac{\epsilon_2}{\epsilon} \sin \nu t, \\ \mathcal{B}_N &= \frac{\epsilon_3}{\epsilon} \cos \nu t, \qquad \mathcal{B}_{N+1} = \frac{\epsilon_4}{\epsilon} \sin \nu t, \end{aligned} \tag{4.55}$$

inspired by multiflagellates such as *Paramecium* which propel themselves using a metachronal wave of beating cilia [151]. Then the squirming set for such a swimmer is found by projecting the deformations onto the surface of the sphere; the explicit squirming set is given in tables 2.1 and 2.2. In this case we have taken the model parameters to be $N = 20$ and $\epsilon_1 = -\epsilon_2 = -\epsilon_3 = \epsilon_4 = 0.05r_2$. A consequence of the structure of the activity is that the dipolar contributions to the slip velocity are purely periodic in time, and therefore zero in a time averaged description, so that a squirmer of this form is neither a pusher nor a puller. This in turn means the interaction with a wall results only in reorientation and deflection, as may be seen in fig. 4.5. A comparison of the full time-dependent model and a time-averaged description shows that there is very little difference in trajectories, even when the separation with a surface is very small. This is because the swimming speed is of order $\epsilon^2\nu r_2$, while one time period of the squirming action is $2\pi/\nu$. Hence in one time period the swimmer translates by a displacement around two orders of magnitude smaller than its size, and the propagation speed of the surface metachronal wave is much smaller than the swimming speed.

The behaviour of a small swimmer inside a circular tank has the same qualitative features as the swimming near a wall. Thus the B_2 modes, shown on the left-hand side of fig. 4.6(a), show similar periodic orbits following the edge of the tank. The right-hand side of the same figure shows the behaviour of constant A_2 behaviour, and is shown for comparison with the results of Davis and Crowdy [128], who found very similar trajectories, which reorient and stop on impact, for a swimmer modelled by a dipole singularity with higher-order image corrections. Fig. 4.6(b) shows the motion of a simple puller (blue) and pusher (red), demonstrating the symmetry under time-reversal: the red trace followed backwards is the same as the blue trace, up to a reversal of swimming direction, as demonstrated schematically in fig 2.3. A Blake-type metachronal swimmer again undergoes deflection, with the time-dependence of the swimming stroke becoming important close to contact and changing the deflection angle (fig. 4.7).

4.4 Two external discs

The flow about two non-enclosing cylinders was solved by Jeffery [117], but not given in general except for the special case of two counter-rotating cylinders of equal size (the general case, completed but unpublished by Jeffery, was given explicitly much later by Smith [184]). This was used to demonstrate what has since become known as the Jeffery paradox: that two rotating cylinders generate a uniform stream

infinitely far away, as well as a solid-body rotation of the fluid. This problem, together with the Stokes paradox mentioned earlier, arises because the assumption of Stokes flow is not valid at infinity. In particular, an expansion in Reynolds number about the Stokesian limit fails where flows decay more slowly than the reciprocal of distance [100]. Thus we expect to run into some problems. In the enclosed geometries considered previously ($\kappa_1 \geq 1$) these problems were avoided since the flow at infinity is either specified as a boundary condition (in the case of the wall) or physically irrelevant (in the case of enclosing circular boundaries).

The ansatz used for the solution, eq. (4.34), features equal and opposite forces on the boundaries. This avoids the Stokes paradox, since far away the effect of the two opposing forces cancels out, at the expense of limiting the utility of possible solutions. Nevertheless when used with the reciprocal theorem we are still able to resolve relative motions, and thus characterise interactions. On the other hand, following the same solution scheme as used in the previous section runs into deeper problems. In particular, while there is a non-zero force and torque on each of the two cylinders, the force and torque acting on any portion of the fluid containing both cylinders is zero [180, 181, 185]. Thus we do not have sufficient freedom in our solution to specify six components of motion, as they are driven by six forces/torques with three constraints (that the resultant force in both planar directions and torque on the cluster be zero).

Before discussing the resolution of this problem we demonstrate the Jeffery solution as a limiting case of the solution presented above. In terms of the ansatz coefficients the forces are equal and opposite, as before, and given by

$$\tilde{F}_{1,2} = \pm 8\pi\mu\mathcal{F}_0, \tag{4.56}$$

while the torques are

$$\begin{aligned}\tilde{T}_{1,2} &= -8\pi\mu y_{1,2}\mathrm{Re}[\mathcal{F}_0] \mp 8\pi\mu R(\kappa_1^{-2} + \kappa_2^2)\mathrm{Re}[\alpha] \\ &= -\mathrm{Im}[\overline{z_{1,2}}\tilde{F}_{1,2}] \mp 8\pi\mu R(\kappa_1^{-2} + \kappa_2^2)\mathrm{Re}[\alpha]\end{aligned} \tag{4.57}$$

The first term in the torque corresponds to the couple induced by the tangential force, which is perpendicular to the line of centres of the discs. It may be verified by taking a circuit about $\zeta = 1$ that the total torque on the system about the origin is zero.

The resistance matrix for the motion of the two cylinders is

$$\begin{bmatrix} \mathrm{Im}[\tilde{F}_1] \\ \mathrm{Re}[\tilde{F}_1] \\ \tilde{T}_1 \\ \tilde{T}_2 \end{bmatrix} = 4\pi\mu \begin{bmatrix} \mathcal{M}_{U\parallel} & 0 & 0 & 0 \\ 0 & \mathcal{M}_{U\perp} & \frac{r_1}{r_2}\mathcal{M}_{\Omega U} & \frac{r_2}{r_1}\mathcal{M}_{\Omega U} \\ 0 & \frac{r_1}{r_2}\mathcal{M}_{\Omega U} & \mathcal{M}_{\Omega 1} & \mathcal{M}_{\Omega\Omega} \\ 0 & \frac{r_2}{r_1}\mathcal{M}_{\Omega U} & \mathcal{M}_{\Omega\Omega} & \mathcal{M}_{\Omega 2} \end{bmatrix} \begin{bmatrix} \mathrm{Im}[\tilde{U}_1 - \tilde{U}_2] \\ \mathrm{Re}[\tilde{U}_1 - \tilde{U}_2] \\ \tilde{\Omega}_1 \\ \tilde{\Omega}_2 \end{bmatrix}, \quad (4.58)$$

where

$$\begin{aligned} \mathcal{M}_{U\parallel} &= \frac{1}{\frac{(1-\kappa_1^2\kappa_2^2)}{(1+\kappa_1^2\kappa_2^2)} + \log[\kappa_1\kappa_2]}, \qquad \mathcal{M}_{U\perp} = \frac{\kappa_1\kappa_2}{K}\left(\frac{r_1}{r_2} + \frac{r_2}{r_1}\right) \\ \mathcal{M}_{\Omega U} &= -\frac{r_1 r_2}{2R}\frac{(1-\kappa_1^2\kappa_2^2)}{K}, \qquad \mathcal{M}_{\Omega 1,2} = \frac{(1-\kappa_1^2\kappa_2^2)^2}{(1-\kappa_1^2)(1-\kappa_2^2)K} r_{1,2}^2 - \mathcal{M}_{\Omega\Omega} \\ \mathcal{M}_{\Omega\Omega} &= \frac{\kappa_1\kappa_2 r_1 r_2}{K}\left(1 + \frac{(1+\kappa_1^2\kappa_2^2)}{(1-\kappa_1^2\kappa_2^2)}\log[\kappa_1\kappa_2]\right), \end{aligned} \quad (4.59)$$

and

$$K = \kappa_1\kappa_2\left(\frac{r_1}{r_2} + \frac{r_2}{r_1}\right)\log(\kappa_1\kappa_2) - (1-\kappa_1^2\kappa_2^2). \quad (4.60)$$

As the ansatz (4.34) has no net force (as is clear from the expression of the flow in terms of singularities, eq. (4.36)),

$$\tilde{F}_2 = -\tilde{F}_1. \quad (4.61)$$

This system is not invertible, the resistance matrix having determinant zero. With respect to the four components of motion shown in the resistance matrix, there is a solution to the Stokes equations with the boundary conditions (4.22) that is force- and torque-free, but with nonzero motion of the two discs. Consider the flow field

$$\tilde{u} + \mathrm{i}\tilde{v} = \mathrm{i}\Omega_\odot(z - z_\odot), \quad (4.62)$$

which corresponds to solid rotation of the fluid about a point $z_\odot$ (this solid rotation does not introduce any forces or torques in the zero Reynolds number limit as these would be a result of inertia). Since this flow is not singular anywhere it is trivially true that there is no force or torque acting anywhere. Next, on the disc surfaces the boundary conditions are

$$\mathrm{i}\Omega_\odot(z - z_\odot) = \tilde{U}_1 + \mathrm{i}(z - z_1)\tilde{\Omega}_1, \quad \mathrm{i}\Omega_\odot(z - z_\odot) = \tilde{U}_2 + \mathrm{i}(z - z_2)\tilde{\Omega}_2 \quad (4.63)$$

so

$$\tilde{\Omega}_1 = \tilde{\Omega}_2 = \Omega_\odot, \quad \tilde{U}_{1,2} = -\mathrm{i}\Omega_\odot(z_{1,2} - z_\odot). \tag{4.64}$$

This solid-body rotation arises from the solution presented above and vanishes only if

$$r_1^2\tilde{\Omega}_1 = -r_2^2\tilde{\Omega}_2. \tag{4.65}$$

Presumably this is the reason Jeffery chose the solution of two equal counter-rotating cylinders, which satisfies this condition, to present his paradox [117].

For the reciprocal theorem we require, ideally, a solution to the Stokes dragging of the two cylinders with independent forces and torques on each one. Failing this a solution able to isolate equal and opposite force and torque on the two cylinders at least allows for relative motions to be computed. However we cannot even do this; while the axial force, $\mathrm{Im}[\tilde{F}_1]$ decouples from the rest of the motion, the tangential force cannot be decoupled from the torque. We find that

$$\tilde{T}_2 = -\tilde{T}_1 - \frac{2R(1-\kappa_1^2\kappa_2^2)}{(1-\kappa_1^2)(1-\kappa_2^2)}\mathrm{Re}[\tilde{F}_1], \tag{4.66}$$

so while the case $\tilde{F}_{1,2} = 0, \tilde{T}_{1,2} \neq 0$ may be calculated, allowing determination of relative rotations, this solution does not afford us the case $\tilde{T}_{1,2} = 0, \tilde{F}_{1,2} \neq 0$, and the translation may not be isolated.

Resolution of Jeffery's paradox

As the streamfunction is a biharmonic function it may have harmonic terms added to it. One such term, which is not separable, is the two-dimensional Green's function for Laplace's equation,

$$\log|z|. \tag{4.67}$$

Clearly, derivatives of this function are also harmonic, and by consequence biharmonic. In his solution of the Stokes flow about two rotating discs Jeffery [117] neglected this important term from his expansion of the streamfunction.

These extra terms had been identified in a previous paper on elastic stress in a domain between two circular boundaries, also governed by the biharmonic equation [186], but not applied to the hydrodynamic problem. It was later recognised, apparently independently, by Umemura [181] and Watson [118] that these forgotten contributions to the streamfunction correspond to Stokeslets and rotlets at infinity - in other words, allow a non-zero resultant force and torque on the cylinder cluster, while avoiding the overall solid-body rotation that plagues any naïve attempt to

solve the two-disc Stokes drag problem.

Since the total force on the system may now be non-zero the Stokes paradox once again appears. Although the resolution by matching to an outer Navier-Stokes solution has been used in the two-disc solution [180, 181] to regularise the far-field flow (see also the work of Smith [182, 185] for discussions of the Jeffery paradox as a limit of three-dimensional Stokes flow), as we saw in Chapter 2 the Stokes paradox does not preclude use of the reciprocal theorem. Hence for our purposes it would be sufficient to find just the inner solution.

4.5 Discussion

We have presented exact solutions for the interaction of a circular swimmer with a planar or concave boundary in two dimensions. While the equations of motion of an active disc near a wall have been given before by Crowdy [81, 82], and indeed the present work should be viewed as an extension of these studies, we generalise to concave geometries and account for any axisymmetric slip velocity. This is possible thanks to the use of the reciprocal theorem, which allows the motion due to any slip velocity to be found once a suitable integration kernel has been identified.

The conjugate solution used here is that for Stokes drag on two circular boundaries [81, 107, 117, 166] which, by its use of bipolar coordinates, gives a general result valid both for a interaction of a disc with a plane wall and with a circular enclosure. By rederiving this result based on the approach of [81] we have been able to express the solution in terms of point-singularities, connecting it to the three-dimensional literature on singularity solutions.

We have examined the motion of a circular swimmer propelling itself by means of surface distortions, as proposed by Blake [78], representing the metachronal wave of microorganisms such as *Paramecium* and *Opalina*. As the squirming sets of these organisms lack a stresslet term, A_2, B_2, the interaction with surfaces results in reorientation and deflection, with the deflection angle slightly changed if a fully time-dependent model is considered. The behaviour at a wall and a concave boundary is qualitatively similar.

A full generalisation to non-axisymmetric slip velocities would be straightforward by supplementing Blake's two-dimensional squirming modes, eq. (4.19) with the antisymmetric slip velocity

$$u_r = \sum_{n=0}^{\infty} A'_n \sin n(\theta - \alpha), \qquad u_\theta = \sum_{n=1}^{\infty} B'_n \cos n(\theta - \alpha). \tag{4.68}$$

This antisymmetric squirming set is rather simpler to write down than the full three-dimensional expansion of slip velocity in vector spherical harmonics [77]. Equations of motion analogous to eqs. (4.48)-(4.50) could be found, and it is expected by the similarity of the structure of eq. (4.68) to the axisymmetric squirming set, eq. (4.19), that the algebra will follow in the same way. This would give a full, exact solution for all components of motion, which is not available in three dimensions, as will be discussed in Chapter 5. In this way investigation of non-axisymmetric swimming strategies, under-investigated in the literature, could be undertaken and would be an illuminating extension of this work.

While the Jeffery-Jeffrey-Onishi solution may be further generalised to the Stokes drag on two separate discs in an infinite fluid, and thus in principle be used to calculate exact expressions for the interactions of two swimmers with each other, this solution is known to have serious issues that hinder such use. Specifically, the Jeffery-Jeffrey-Onishi solution exhibits zero net force and zero net torque on the system of two discs. As a result there is no freedom to independently specify the forces and torques, and the resistance matrix for the two discs, eq. (4.58), is singular. Furthermore, for all choices of rotations of the two discs except $r_1^2\tilde{\Omega}_1 = -r_2^2\tilde{\Omega}_2$ the flow corresponds to a solid-body rotation of the entire fluid domain, and is therefore not physically realistic.

These issues are addressed in a number of papers by the addition of a point force and torque at infinity, which allows the disc cluster to experience non-zero resultant force and torque [118, 180, 181]. These extra point singularities at infinity manifest themselves in the conformal-mapping formulation of the problem as Schottky-Klein prime functions, which arise naturally in problems involving elliptic operators in multiply-connected domains as a result of infinite series of reflections in the boundaries [178]. This also results in the Stokes paradox, since the net force in the fluid is zero, which is typically dealt with by taking the Stokes flow as an inner solution and matching to an outer solution of the Navier-Stokes equations. Nevertheless, as we have seen in Chapter 2 the Stokes paradox does not hinder use of the reciprocal theorem and this additional step is not required.

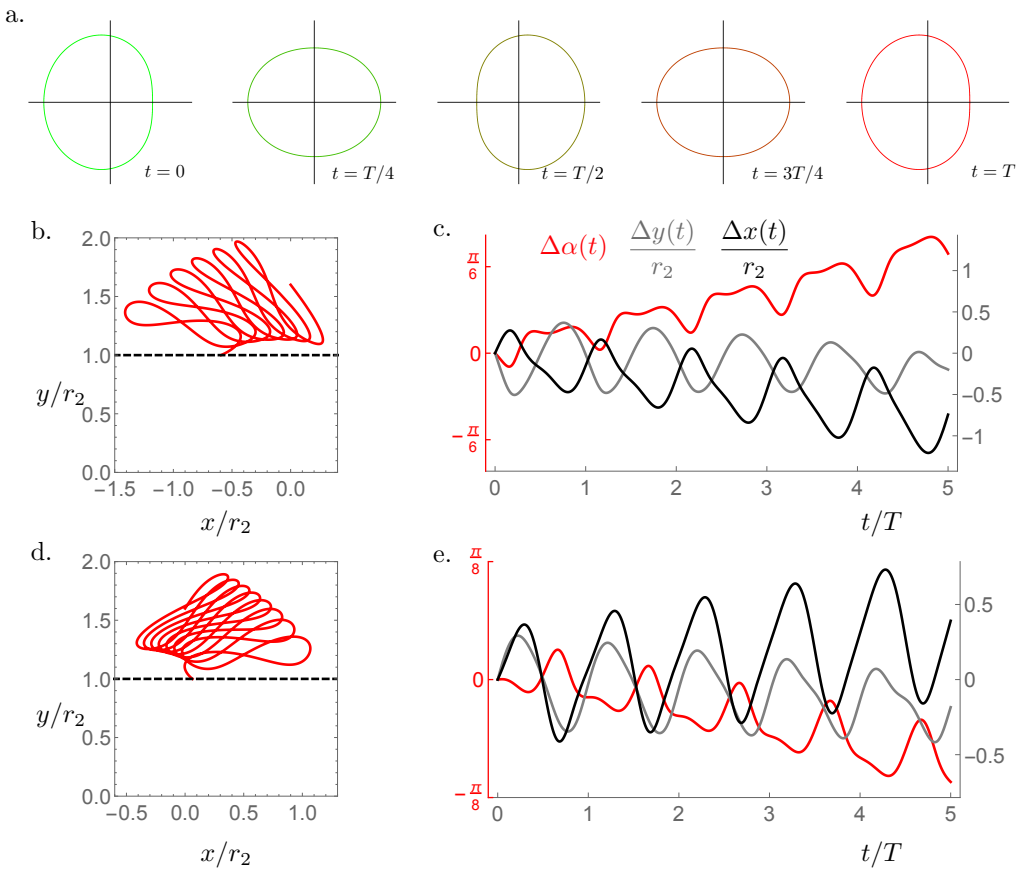

Figure 4.4: Behaviour of a 'jelly-bean' squirmer of unit radius with changing shape near a wall. The slip velocity is $u_r = 0.1 \sin\omega_1(t-\phi_1)\sin(\theta-\alpha) + 0.2\sin 2\omega_1(t-\phi_2)\sin 2(\theta-\alpha)$, with phases $\phi_1 = \pi$, $\phi_2 = \pi/2$. (a) Cycle of shapes over a time period T. (b) Trajectory in real space with initial configuration $\alpha(0) = -0.7$rad. (c) Trajectory of coordinates and orientation in time for trajectory (b), where Δ denotes the difference from the initial value of a particular quantity. (d) Trajectory in real space with initial configuration $\alpha(0) = +0.6$rad. (e) Trajectory of coordinates and orientation in time for trajectory (d).

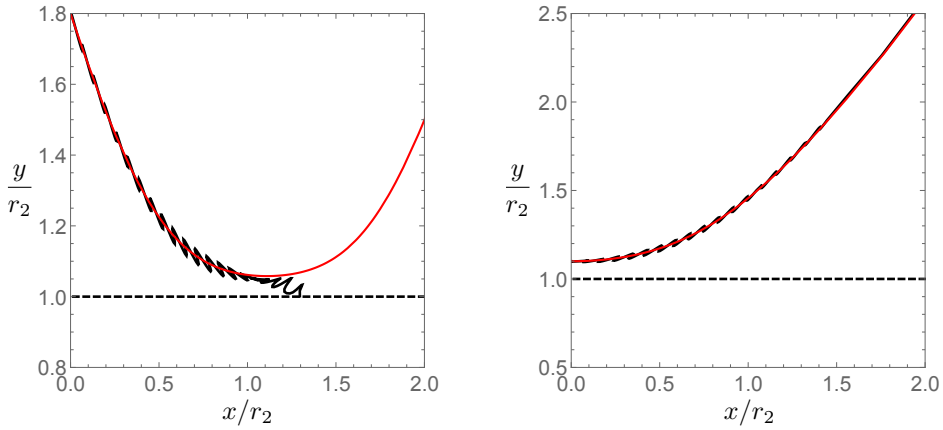

Figure 4.5: Some example trajectories of the motion of a time-dependent Blake-type squirmer, as outlined in chapter 2, near a wall. The squirmer's parameters are $N = 20$, $\epsilon_1 = -\epsilon_2 = -\epsilon_3 = \epsilon_4 = 0.05r_2$. The black trace retains full time-dependence, while the red trace uses time-averaged squirming coefficients. The dominance of the A_1 and B_1 modes means the generic behaviour is deflection. The squirmer description breaks down if the gap between the swimmer and the wall becomes comparable to the amplitude of the surface oscillations, since the squirming coefficients are calculated by an expansion in this amplitude.

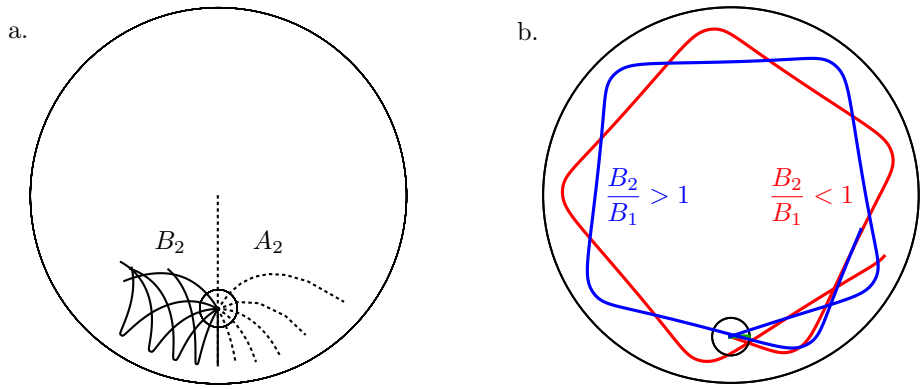

Figure 4.6: (a) Behaviour of squirming modes A_2 (dashed) and B_2 (solid) for initial orientations $\alpha(0) = n\pi/12$, $n \in \{0, \ldots, 6\}$. At impact the B_2 mode causes deflection and scattering, while A_2 leads to trapping as seen in point-singularity models [128]. (b) Swimming of a puller (blue) and pusher (red) with the same relative magnitude of B_1 and B_2, indicating time-reversal symmetry. the initial orientation is the horizontal direction, to the right.

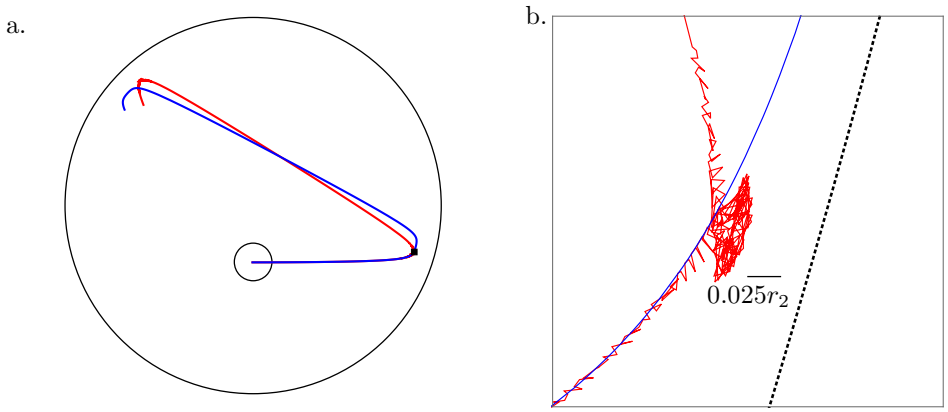

Figure 4.7: (a) Some example trajectories of the motion of a time-dependent Blake-type squirmer in a circular tank (red), compared to a time-averaged description (blue). The squirmer's parameters are $N = 20$, $\epsilon_1 = -\epsilon_2 = -\epsilon_3 = \epsilon_4 = 0.025r_2$. (b) Close-up of impact with wall, showing difference between time-dependent and time-averaged descriptions. Collision radius shown as dotted black line. The region shown corresponds to the small black box in (a).

5

Exact solutions in three dimensions

In this chapter, we find exact solutions for the axisymmetric translation and rotation of a squirmer in the presence of a spherical or planar boundary. These are valid at any separation, both in the far-field where point singularity solutions are accurate and in the contact limit of vanishing separation, where such approximate solutions are not accurate. They also account for any type of squirming motion and not simply the lowest order modes that point singularity descriptions are typically restricted to [65, 67]. It should be noted that the behaviour of a squirmer close to a surface has been investigated numerically by Ishimoto and Gaffney [149].

This is done using exact solutions for the conjugate Stokes drag problem. Such solutions are available for the Stokes drag on a pair of spheres, or of a single sphere close to a planar wall or fluid interface. The symmetries of the geometry mean there are two independent directions, namely the common diameter of the two spheres and any axis perpendicular to this, and the solution consists of translation and rotation in each of these directions, so that the general motion separates into four components that can be treated individually. The axisymmetric rotation was solved exactly by Jeffery [114], and has since been supplemented by the closely related solution for rotation of a sphere beneath a planar fluid interface [115, 187]. The solution for axisymmetric translation was given by Stimson and Jeffery [113] and found to be in remarkably good agreement with experiment [188]. The special

case of sedimentation of a sphere towards a solid plane was subsequently given a more detailed analysis both in the limit of large separation [189] and of contact [190], with the latter giving a comparison to results obtained from lubrication theory, while the case of two spheres in contact translating along their line of centres was studied by Cooley and O'Neill [191]. Several attempts to find the non-axisymmetric motions and rotations have been unable to give the solution in a closed form; the problem is reduced to a system of difference equations, of which an analytic solution has not been found. Nevertheless it is possible to compute the flow to any degree of accuracy [116, 192–197].

All of these results rely on the use of bispherical coordinates, in which any configuration of two convex or concave spherical boundaries, as well as the intermediate limit of a plane, is an isosurface. This coordinate system greatly simplifies the imposition of boundary conditions; furthermore, since it is conformally equivalent to spherical coordinates, Laplace's [198] and by consequence Stokes' [117] equations are separable.

This Chapter exhibits exact solutions for hydrodynamics interactions between spherical squirmers, using the reciprocal theorem. The derivation of the conjugate solutions used is rather technical, and the reader primarily interested in applications to swimmer motion is invited to skip directly to § 5.4, and refer back to previous sections as necessary. We first introduce the bispherical coordinate system which facilitates exact calculations on two spherical boundaries. We then demonstrate the Stokes drag solutions that are to be used with the reciprocal theorem: §5.2 is an exposition of Jeffery's solution for the drag on two spheres rotating in an axisymmetric arrangement, together with a closely related solution for the rotation of spheres in two fluids separated by a stress-free interface, while §5.3 is a discussion of the general solution to the Stokes equations in bispherical coordinates, and the application to two axisymmetric translating spheres.

The motion of an axisymmetric squirmer interacting with a passive spherical boundary is found in §5.4 using the reciprocal theorem. The contribution to the motion from the azimuthal squirming coefficients is found explicitly for all orders and is shown for a model organism driven by a rotating cap, while a simple extension to case of interaction with a planar free surface discussed in §5.4.5. The meridional and radial squirming coefficients do not at present have a general form for the interaction valid at all orders; in §5.4.6 we calculate the interaction due to the lowest two orders of these modes. Finally we discuss some of the limitations of the method presented here in §5.5.

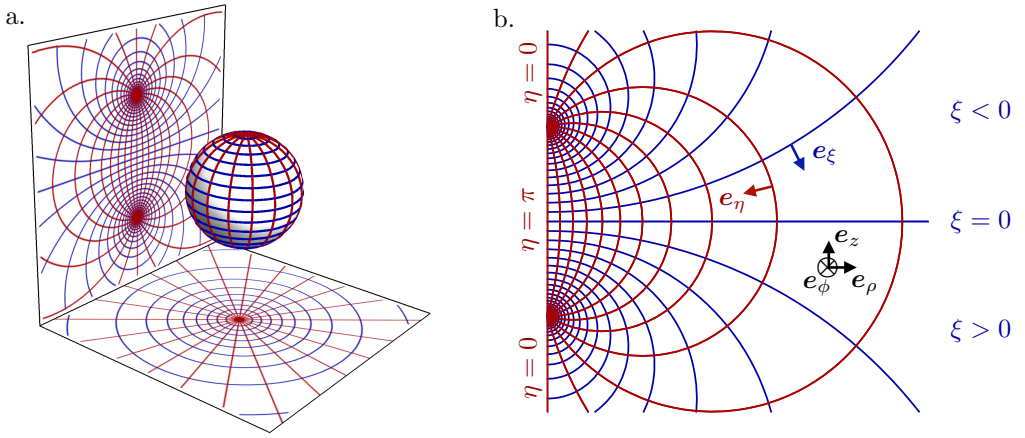

Figure 5.1: (a) Stereographic projection of gridlines on a globe about a pole gives a polar grid (below), while a projection about an equatorial point gives a bipolar grid. (b) Conventions of the bispherical coordinate system (ξ, η, ϕ) used in this work, related to the cylindrical basis (z, ρ, ϕ). The ϕ coordinate coincides for the two coordinate systems.

5.1 Bispherical coordinates

In three dimensions, to perform calculations involving conditions on two spherical surfaces it is convenient to use *bispherical coordinates*. These arise naturally as an extension of the two-dimensional bipolar coordinates used in the previous chapter by rotation about the line of separation of the two discs; this rotation is quantified by an azimuthal coordinate.

As we shall see, this definition of bispherical coordinates is particularly convenient for axisymmetric configurations, such as the translation or rotation about the separation axis, in which case the problem is effectively two-dimensional (for the same reason, the three-dimensional Stokes streamfunction is only useful in axisymmetric contexts [174]).

There exist several uses of the bispherical coordinate system in the swimmer literature, although it appears none exploit them to solve for interactions, instead using them to model novel swimming strategies. For instance, [103] and [104] constructed a theoretical model of a catalytic dimer [199, 200] composed of a self-diffusiophoretic [30, 31] catalytic bead attached to a passive bead of 'cargo'. Self-propulsion results from the head-tail asymmetry and may be adjusted by changing the relative sizes and compositions of the two beads, and is calculated using the single-body form of the reciprocal theorem [89]. Many two-dimensional studies on two discs [81, 82, 166] use bipolar coordinates, a planar analogue of bispherical.

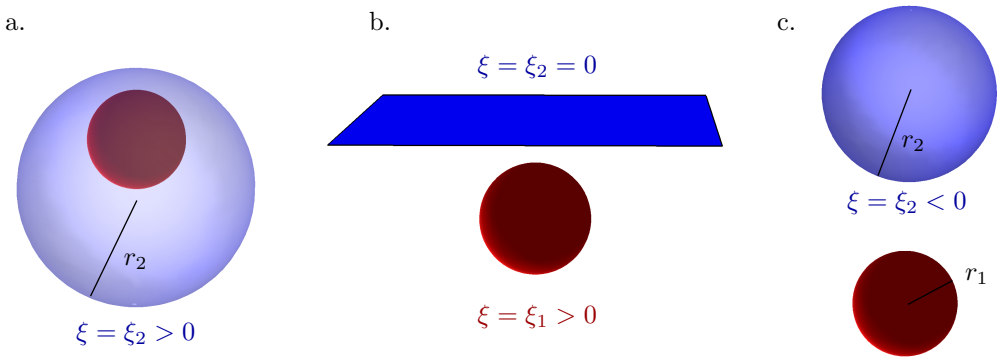

Figure 5.2: The range of geometries allowed by the bispherical coordinate system. The red sphere is given by $\xi = \xi_1$, which is always taken to be positive; the other boundary is defined by $\xi = \xi_2$, and the sign of ξ_2 determines the geometry as shown: (a) A spherical enclosure. (b) A planar surface. (c) A solid sphere.

The closely related toroidal coordinates have also seen use in calculating the flow about a torus [108–110], and using these solutions the swimming speed of Purcell's rolling toroidal swimmer [3, 12].

5.1.1 Definition of coordinates

The solution of boundary value problems on two spheres is greatly simplified by employing a *bispherical* coordinate system, where these surfaces are level sets. If $z + \mathrm{i}\rho$ is a complex coordinate on a Cartesian grid, the bipolar coordinate grid $\xi + \mathrm{i}\eta$ is defined by

$$\xi + \mathrm{i}\eta = \ln\left[\frac{z + \mathrm{i}\rho - R}{z + \mathrm{i}\rho + R}\right], \qquad z + \mathrm{i}\rho = -R\left[\frac{\sinh\xi - \mathrm{i}\sin\eta}{\cosh\xi - \cos\eta}\right], \tag{5.1}$$

where R is a positive real number. This can be thought of as a stereographic projection of the lines of latitude and longitude on a sphere about a point on the equator. The poles map to two symmetric points. Finally, a rotation by 2π about the symmetry axis on which the points lie gives an azimuthal coordinate ϕ, which coincides for bispherical and ordinary cylindrical coordinates. Note that this definition differs slightly from the most common definition in the literature,

$$\xi + \mathrm{i}\eta = \ln\frac{\rho + \mathrm{i}(z + R)}{\rho + \mathrm{i}(z - R)}, \tag{5.2}$$

which more closely matches the conformal map used in the previous chapter [113], although the two definitions are obviously equivalent since they differ only by a

rotation. Eq. (5.1) gives the conformal transformation used previously under the identification $\mathrm{e}^{\xi+\mathrm{i}\eta} \equiv \zeta$ and $-\rho + \mathrm{i}z \equiv z$ (noting in the latter case that the z on the left hand side is the axial coordinate while that on the right hand side is the complex coordinate).

Surfaces of constant ξ are non-intersecting spheres of radius $r = R\,|\mathrm{cosech}\xi|$ with their centres at $-R\coth\xi$; we define the fluid as the region $\xi_2 < \xi < \xi_1$, where ξ_1 is taken to be positive. The choice of ξ_2 defines the geometry: if it is positive the fluid is the region between two nested spherical boundaries and if it is negative the fluid is external to two spheres, while the intermediate case $\xi_2 = 0$ represents the half-space.

The metric in bispherical coordinates is conformal to the standard round metric on $\mathbb{R} \times S^2$,

$$\mathrm{d}\rho^2 + \mathrm{d}z^2 + \rho^2\mathrm{d}\phi^2 = h^2[\mathrm{d}\xi^2 + \mathrm{d}\eta^2 + \sin^2\eta\,\mathrm{d}\phi^2], \tag{5.3}$$

where

$$h(\xi,\eta) = \frac{R}{\cosh\xi - \cos\eta} \tag{5.4}$$

is the conformal factor. This conformal equivalence means the scale factors are immediate:

$$h_\xi = h_\eta = h(\xi,\eta), \qquad h_\phi = h(\xi,\eta)\sin\eta. \tag{5.5}$$

These can be used in the usual way to compute differential operators.

We now record some useful relations between bispherical and cylindrical coordinates. Since the ϕ coordinates coincide for both coordinate systems there is a planar rotation about this axis that maps between $(\boldsymbol{e}_\xi, \boldsymbol{e}_\eta)$ and $(\boldsymbol{e}_z, \boldsymbol{e}_\rho)$ (up to a minus sign). By our definition of the bispherical coordinates we find that

$$\begin{bmatrix} \boldsymbol{e}_z \\ \boldsymbol{e}_\rho \end{bmatrix} = -\begin{bmatrix} \cos\beta & -\sin\beta \\ \sin\beta & \cos\beta \end{bmatrix}\begin{bmatrix} \boldsymbol{e}_\xi \\ \boldsymbol{e}_\eta \end{bmatrix} \tag{5.6}$$

where the rotation angle is defined by

$$\cos\big(\beta(\xi,\eta)\big) \equiv \frac{1-\cosh\xi\cos\eta}{\cosh\xi - \cos\eta}, \quad \sin\big(\beta(\xi,\eta)\big) \equiv \frac{\sinh\xi\sin\eta}{\cosh\xi - \cos\eta}. \tag{5.7}$$

Using this transformation we derive the following properties of the bispherical unit

vectors,

$$\begin{aligned} h^{-1}\partial_\xi \boldsymbol{e}_\xi &= \frac{\sin\eta}{R}\boldsymbol{e}_\eta, \qquad & h^{-1}\partial_\eta \boldsymbol{e}_\xi &= -\frac{\sinh\xi}{R}\boldsymbol{e}_\eta, \\ \partial_\phi \boldsymbol{e}_\xi &= -\sin\beta\,\boldsymbol{e}_\phi, & h^{-1}\partial_\xi \boldsymbol{e}_\eta &= -\frac{\sin\eta}{R}\boldsymbol{e}_\xi, \\ h^{-1}\partial_\eta \boldsymbol{e}_\eta &= \frac{\sinh\xi}{R}\boldsymbol{e}_\xi, & \partial_\phi \boldsymbol{e}_\eta &= -\cos\beta\,\boldsymbol{e}_\phi, \\ \partial_\phi \boldsymbol{e}_\phi &= -\boldsymbol{e}_\rho = \cos\beta\,\boldsymbol{e}_\eta + \sin\beta\,\boldsymbol{e}_\xi, \end{aligned} \tag{5.8}$$

which will be useful later when calculating derivatives.

5.1.2 Laplace's equation in bispherical coordinates

As we saw in the previous chapter, solutions to the Stokes equations can be constructed using harmonic functions. While Laplace's equation may be computed using the scale factors as

$$\nabla^2 u = \frac{1}{h^3}\partial_\xi h \partial_\xi u + \frac{1}{h^3 \sin\eta}\partial_\eta \sin\eta h \partial_\eta u + \frac{1}{h^2 \sin^2\eta}\partial_{\phi\phi} u = 0, \tag{5.9}$$

this form is not separable. We therefore establish the general form of solutions of Laplace's equation, $\nabla^2 u = 0$, in bispherical coordinates. The following solution was first given by Jeffery [198].

Defining a conformal metric tensor by $g_{ij} = h^2 \tilde{g}_{ij}$, the Laplacian of a scalar function u is given by

$$\nabla^2 u = \frac{1}{\sqrt{\det g}}\,\partial_i \sqrt{\det g}\, g^{ij}\partial_j u. \tag{5.10}$$

Introducing a conformal scaling of the field u with weight w,

$$\nabla^2 u = h^{-3}\frac{1}{\sqrt{\det \tilde{g}}}\,\partial_i h \sqrt{\det \tilde{g}}\,\tilde{g}^{ij}\partial_j\big(h^{-w}(h^w u)\big), \tag{5.11}$$

$$\begin{aligned} &= h^{-3}\bigg[h^{1-w}\frac{1}{\sqrt{\det \tilde{g}}}\,\partial_i \sqrt{\det \tilde{g}}\,\tilde{g}^{ij}\partial_j h^w u \\ &\quad - w\bigg(\frac{1}{\sqrt{\det \tilde{g}}}\,\partial_i \sqrt{\det \tilde{g}}\,\tilde{g}^{ij} h^{-w}\partial_j h\bigg) h^w u \\ &\quad + (1-2w) h^{-w}\tilde{g}^{ij}(\partial_i h)(\partial_j h^w u)\bigg]. \end{aligned} \tag{5.12}$$

The last term in eq. (5.12) is eliminated by the choice $w = \frac{1}{2}$ for the conformal weight for any conformal metric. In this case $\tilde{g}_{ij}$ is the standard round metric on

$\mathbb{R} \times S^2$ as given in eq. (5.3),

$$\tilde{g}_{ij} = \begin{bmatrix} 1 & 0 & 0 \\ 0 & 1 & 0 \\ 0 & 0 & \sin^2\eta \end{bmatrix}. \tag{5.13}$$

Substituting the explicit form of the metric Laplace's equation in bispherical coordinates takes the form

$$\nabla^2 u = h^{-\frac{5}{2}}\left[\partial_{\xi\xi} + \frac{1}{\sin\eta}\,\partial_\eta \sin\eta \partial_\eta + \frac{1}{\sin^2\eta}\partial_{\phi\phi} - \frac{1}{4}\right] h^{\frac{1}{2}} u = 0. \tag{5.14}$$

Supposing a separable solution of the form

$$h^{\frac{1}{2}} u = \Xi(\xi) H(\eta) \mathrm{e}^{\mathrm{i}m\phi}, \tag{5.15}$$

eq. (5.14) becomes

$$\frac{\Xi''(\xi)}{\Xi(\xi)} - \frac{1}{4} = \frac{m^2}{\sin^2\eta} - \frac{1}{H(\eta)}\left(\frac{1}{\sin\eta}\partial_\eta \sin\eta \partial_\eta H(\eta)\right). \tag{5.16}$$

Since this must hold for $H(\eta)$ independently of ξ and for $\Xi(\xi)$ independently of η, the right- and left-hand sides must equal the same constant, say $l(l+1)$, and we must solve

$$\Xi''(\xi) = \left(l + \tfrac{1}{2}\right)^2 \Xi(\xi) \tag{5.17}$$

and

$$\frac{1}{\sin\eta}\partial_\eta \sin\eta \partial_\eta H(\eta) + \left(l(l+1) + \frac{m^2}{\sin^2\eta}\right) H(\eta). \tag{5.18}$$

The first of these gives an exponential dependence on ξ. The latter is Legendre's differential equation, with the general solution

$$H(\eta) = \chi_1 P_l^m(\cos\eta) + \chi_2 Q_l^m(\cos\eta) \tag{5.19}$$

where P_l^m and Q_l^m are associated Legendre functions of the first and second kind respectively and $\chi_{1,2}$ are some constants. Since $Q_l^m(\cos\eta)$ is divergent for $\eta = 0, \pi$, corresponding to the z-axis, any solution which is to be finite on this axis can only contain contributions from Legendre functions of the first kind. Furthermore, since the η coordinate is periodic we retain only Legendre polynomials of integer order.

Hence the general harmonic function in bispherical coordinates is

$$u = h^{-\frac{1}{2}} \sum_{l=0}^{\infty} \sum_{m=-l}^{l} \Big[a_{l,m}\, \mathrm{e}^{(l+1/2)(\xi-\xi_2)} + b_{l,m}\, \mathrm{e}^{-(l+1/2)(\xi-\xi_1)} \Big] \mathrm{e}^{\mathrm{i}m\phi} P_l^m(\cos\eta), \quad (5.20)$$

where $a_{l,m}$, $b_{l,m}$ are arbitrary constants, subject only the condition that u be real. The factors depending on ξ_1 and ξ_2 have explicitly been put in to reflect the fact that we will be solving this (and other related differential equations) in the region between ξ_1 and ξ_2.

5.2 Stokes drag solutions for axisymmetric rotations

5.2.1 Two rotating spheres

The general solution for axisymmetric azimuthal flows was given by Jeffery [114], together with a number of specific examples, including the coaxial rotation of two spheres, and was subsequently expanded upon by Kanwal [112]. Here we present the solution for two spheres, together with a closely related solution for a sphere rotating about the normal to a flat free surface [115, 187]. The solution may then be used together with the reciprocal theorem to calculate the axisymmetric rotation of a spherical squirmer close to another sphere or free surface.

For an axisymmetric, purely azimuthal Stokes flow, such as that due to a solid of revolution rotating about its symmetry axis [114], the fluid velocity takes the form $\boldsymbol{u} = u_\phi(z,\rho)\boldsymbol{e}_\phi$. The pressure is constant everywhere and may be taken to be equal to zero without loss of generality, and the Stokes equation is reduced to the scalar equation

$$(\nabla^2 - \rho^{-2}) u_\phi = 0. \quad (5.21)$$

This equation is rather simpler to solve than the full Stokes equations and as such several exact solutions of rotating axisymmetric objects exist in the literature, such as ellipsoids [114], lenses and tori [112]. By an entirely analogous procedure to the solution of Laplace's equation shown above, the general solution of equation (5.21) in bispherical coordinates is

$$h^{\frac{1}{2}} u_\phi = \sum_l \Big[c_l\, \mathrm{e}^{(l+\frac{1}{2})(\xi-\xi_2)} + d_l\, \mathrm{e}^{-(l+\frac{1}{2})(\xi-\xi_1)} \Big] P_l^1(\cos\eta), \quad (5.22)$$

where c_l and d_l are real constants. The force per unit area on the boundary takes

the form

$$\boldsymbol{\sigma}\cdot\hat{\boldsymbol{n}}\Big|_{\partial D_i} = \pm\mu\Big(h^{-\frac{3}{2}}\partial_\xi(h^{\frac{1}{2}}u_\phi) + h^{-\frac{1}{2}}\frac{3\sinh\xi}{2R}h^{\frac{1}{2}}u_\phi\Big)\Big|_{\xi=\xi_i}\boldsymbol{e}_\phi, \tag{5.23}$$

and the torque about the common diameter is given by

$$T_i = \int_{\xi=\xi_i}\rho\,\boldsymbol{e}_\phi\cdot(\boldsymbol{\sigma}\cdot\hat{\boldsymbol{n}})h^2\sin\eta\,\mathrm{d}\eta\,\mathrm{d}\phi \tag{5.24}$$

$$= \pm 2\pi\mu\int_0^\pi \sin\eta\Big(h^{\frac{3}{2}}\partial_\xi(h^{\frac{1}{2}}u_\phi) + h^{\frac{5}{2}}\frac{3\sinh\xi}{2R}h^{\frac{1}{2}}u_\phi\Big)\sin\eta\,\mathrm{d}\eta, \tag{5.25}$$

where the integral over ϕ is immediate since the stress tensor is axisymmetric. The η integral is computed as follows. Since $h^{\frac{1}{2}}$ is the generating function for Legendre polynomials [154] we have

$$\left(\frac{h}{R}\right)^{\frac{1}{2}} = \sqrt{2}\sum_m \mathrm{e}^{-(m+\frac{1}{2})|\xi|}P_m(\cos\eta), \tag{5.26}$$

it follows by differentiating both sides with respect to η that

$$\left(\frac{h}{R}\right)^{\frac{3}{2}}\sin\eta = -2^{\frac{3}{2}}\sum_m \mathrm{e}^{-(m+\frac{1}{2})|\xi|}P_m^1(\cos\eta). \tag{5.27}$$

Then, n differentiations with respect to ξ give

$$\left(\frac{h}{R}\right)^{n+\frac{3}{2}}\sin\eta = \sqrt{2}\frac{(-2)^{n+1}}{(2n+1)!!}\sum_{m=1}^{\infty}P_m^1(\cos\eta)\left[\frac{1}{\sinh\xi}\partial_\xi\right]^n\mathrm{e}^{-(m+\frac{1}{2})|\xi|}. \tag{5.28}$$

We shall make extensive use of equation (5.28) in evaluating integrals throughout this chapter. In this particular case we need only consider $n = 0$ and $n = 1$, which give us decompositions of $h^{\frac{3}{2}}$ and $h^{\frac{5}{2}}$ in Legendre polynomials of degree 1. Combining these expansions with the integral (5.25) gives an integral over a product of Legendre polynomials, easily evaluated using the orthogonality property

$$\int_0^\pi \mathrm{d}\eta\,\sin\eta P_l^1(\cos\eta)P_m^1(\cos\eta) = \frac{2l(l+1)}{(2l+1)}\delta_{lm} \tag{5.29}$$

to give the torques

$$T_1 = -4\pi\mu(2R)^{\frac{3}{2}} \sum_l l(l+1)\mathrm{e}^{-(l+\frac{1}{2})\xi_2} c_l, \tag{5.30}$$

$$T_2 = \begin{cases} 4\pi\mu(2R)^{\frac{3}{2}} \sum_l l(l+1)\mathrm{e}^{-(l+\frac{1}{2})\xi_2} c_l & \text{if } \xi_2 > 0, \\ -4\pi\mu(2R)^{\frac{3}{2}} \sum_l l(l+1)\mathrm{e}^{(l+\frac{1}{2})\xi_1} d_l & \text{if } \xi_2 < 0. \end{cases} \tag{5.31}$$

The torques are equal and opposite when the fluid is the finite volume between nested spheres ($\xi_2 > 0$) as a result of incompressibility.

The coefficients c_l and d_l are found from the boundary conditions of solid-body rotation of each sphere. If the sphere $\xi = \xi_{1,2}$ rotates about the z axis with angular velocity $\omega_{1,2}$, then the flow must satisfy

$$h^{\frac{1}{2}} u_\phi\big|_{\xi=\xi_{1,2}} = \omega_{1,2} h^{\frac{3}{2}} \sin\eta\big|_{\xi=\xi_{1,2}}. \tag{5.32}$$

Using equation (5.27) write the boundary conditions as

$$h^{\frac{1}{2}} u_\phi\big|_{\xi=\xi_{1,2}} = -(2R)^{\frac{3}{2}} \omega_{1,2} \sum_l \mathrm{e}^{-(l+\frac{1}{2})|\xi_{1,2}|} P_l^1(\cos\eta). \tag{5.33}$$

Equating (5.22) and (5.33) yields the solution scheme

$$\begin{bmatrix} \mathrm{e}^{(l+\frac{1}{2})(\xi_1-\xi_2)} & 1 \\ 1 & \mathrm{e}^{(l+\frac{1}{2})(\xi_1-\xi_2)} \end{bmatrix} \begin{bmatrix} c_l \\ d_l \end{bmatrix} = -(2R)^{\frac{3}{2}} \begin{bmatrix} \omega_1 \mathrm{e}^{-(l+\frac{1}{2})|\xi_1|} \\ \omega_2 \mathrm{e}^{-(l+\frac{1}{2})|\xi_2|} \end{bmatrix}. \tag{5.34}$$

This is invertible, except for in the degenerate limit $\xi_1 = \xi_2$ in which two spheres share a boundary, and leads to the explicit expressions

$$c_l = -(2R)^{\frac{3}{2}} \frac{\mathrm{e}^{-(l+\frac{1}{2})|\xi_1|}\omega_1 - \mathrm{e}^{-(l+\frac{1}{2})(\xi_1-\xi_2+|\xi_2|)}\omega_2}{2\sinh(l+\frac{1}{2})(\xi_1-\xi_2)} \tag{5.35}$$

$$d_l = (2R)^{\frac{3}{2}} \frac{\mathrm{e}^{-(l+\frac{1}{2})(\xi_1-\xi_2+|\xi_1|)}\omega_1 - \mathrm{e}^{-(l+\frac{1}{2})|\xi_2|}\omega_2}{2\sinh(l+\frac{1}{2})(\xi_1-\xi_2)}, \tag{5.36}$$

which solve the problem fully. In the contact limit $\xi_1, \xi_2 \to 0$ the expressions (5.35) and (5.36) are undefined since the denominator vanishes. However, since

$$\frac{1}{2\sinh\xi} = \frac{\mathrm{e}^{-\xi}}{1-\mathrm{e}^{-2\xi}} = \mathrm{e}^{-\xi} \sum_{n=0}^{\infty} \mathrm{e}^{-2n\xi} = \sum_{n=0}^{\infty} \mathrm{e}^{-(2n+1)\xi}, \tag{5.37}$$

expressions (5.35) and (5.36) may be written as uniformly convergent sums,

$$c_l = (2R)^{\frac{3}{2}} \sum_{n=0}^{\infty} \Big(\omega_2 \mathrm{e}^{-(l+\frac{1}{2})\left(2(n+1)(\xi_1-\xi_2)+|\xi_2|\right)} - \omega_1 \mathrm{e}^{-(l+\frac{1}{2})\left((2n+1)(\xi_1-\xi_2)+|\xi_1|\right)} \Big), \quad (5.38)$$

$$d_l = (2R)^{\frac{3}{2}} \sum_{n=0}^{\infty} \Big(\omega_1 \mathrm{e}^{-(l+\frac{1}{2})\left(2(n+1)(\xi_1-\xi_2)+|\xi_1|\right)} - \omega_2 \mathrm{e}^{-(l+\frac{1}{2})\left((2n+1)(\xi_1-\xi_2)+|\xi_2|\right)} \Big), \quad (5.39)$$

allowing the torques (5.31) to be evaluated explicitly as

$$T_{1,2} = 8\pi\mu r_{1,2}^3 \sum_{n=0}^{\infty} \Big\{ \omega_{1,2} \frac{\sinh^3 \xi_{1,2}}{\sinh^3\big(n(\xi_{1,2}-\xi_{2,1})+\xi_{1,2}\big)} - \omega_{2,1} \frac{\sinh^3 \xi_{1,2}}{\sinh^3 (n+1)(\xi_{1,2}-\xi_{2,1})} \Big\}, \qquad \xi_2 < 0 < \xi_1, \quad (5.40)$$

$$T_{1,2} = \pm 8\pi\mu r_1^3 (\omega_1 - \omega_2) \sum_{n=0}^{\infty} \frac{\sinh^3 \xi_1}{\sinh^3\big(n(\xi_1-\xi_2)+\xi_1\big)}, \qquad 0 \le \xi_2 < \xi_1. \quad (5.41)$$

5.2.2 Two rotating spheres separated by a fluid interface

Using the general solution (5.22) it is possible to construct the solution for an axisymmetric, azimuthal flow in two phases of different viscosities μ_1 and μ_2 with a spherical interface at $\xi = \xi_0$. Here we will consider the most general case available using bispherical coordinates, of a rotating sphere at $\xi_1 > \xi_0$ and another one at $\xi_2 < \xi_0$, which reduces to the solution presented above when $\mu_1 = \mu_2 = \mu$. Alternatively, as $\mu_2/\mu_1 \to \infty$ the interface at ξ_0 becomes a solid boundary and the flow once again corresponds to that between two solid spheres. This solution was given by [115] for the rotation of a single sphere near a planar interface; it had previously been noted by [187] that when two spheres of the same size rotate with the same angular frequency about their common diamater the stress on the midplane identically vanishes, giving the solution for a single sphere beneath a free surface.

Suppose we have in each phase a solution of the form (5.22), so that

$$h^{\frac{1}{2}} u_1 \boldsymbol{e}_\phi = \sum_{l=1}^{\infty} \Big(a_l \, \mathrm{e}^{(l+\frac{1}{2})(\xi-\xi_0)} + b_l \, \mathrm{e}^{-(l+\frac{1}{2})(\xi-\xi_1)} \Big) P_l^1(\cos\eta) \boldsymbol{e}_\phi, \quad \xi_0 < \xi < \xi_1, \quad (5.42)$$

$$h^{\frac{1}{2}} u_2 \boldsymbol{e}_\phi = \sum_{l=1}^{\infty} \Big(c_l \, \mathrm{e}^{(l+\frac{1}{2})(\xi-\xi_2)} + d_l \, \mathrm{e}^{-(l+\frac{1}{2})(\xi-\xi_0)} \Big) P_l^1(\cos\eta) \boldsymbol{e}_\phi, \quad \xi_2 < \xi < \xi_0. \quad (5.43)$$

The flow is driven by the rotations ω_1 and ω_2 on the surfaces of the two solid spheres at ξ_1 and ξ_2. As before, ξ_1 is taken to be positive, and the sphere it describes convex, while the sphere at ξ_2 may be convex ($\xi_2 < 0$), flat ($\xi_2 = 0$) or concave ($\xi_2 > 0$).

The flow is driven by the rotating spheres, so that

$$h^{\frac{1}{2}}u_{1,2}\big|_{\xi=\xi_{1,2}} = -(2R)^{\frac{3}{2}}\omega_{1,2}\sum_{l=1}^{\infty}\mathrm{e}^{-(l+\frac{1}{2})|\xi_{1,2}|}P_l^1(\cos\eta). \tag{5.44}$$

To match the upper and lower solutions the flow and the stress must be continuous across the interface. The first of these conditions,

$$h^{\frac{1}{2}}u_1\big|_{\xi=\xi_0} = W^{\frac{1}{2}}u_2\big|_{\xi=\xi_0}. \tag{5.45}$$

implies the relationship between the unknown coefficients

$$a_l + b_l\,\mathrm{e}^{-(l+\frac{1}{2})(\xi_0-\xi_1)} = c_l\,\mathrm{e}^{(l+\frac{1}{2})(\xi_0-\xi_2)} + d_l. \tag{5.46}$$

Flat interface, $\xi_0 = 0$

If the fluid interface is flat, $\xi_0 = 0$, the pressure in both phases is the same. Then the stress on the boundary identically has no normal component so we need only match the tangential component, which is given by (5.23). Hence the stress continuity condition is

$$\mu_1 h^{-\frac{3}{2}}\partial_\xi\big(W^{\frac{1}{2}}u_1\big)\Big|_{\xi=\xi_0} = \mu_2 W^{-\frac{3}{2}}\partial_\xi\big(W^{\frac{1}{2}}u_2\big)\Big|_{\xi=\xi_0}, \tag{5.47}$$

immediately giving the relation

$$a_l\,\mathrm{e}^{(l+\frac{1}{2})\xi_0} - b_l\,\mathrm{e}^{-(l+\frac{1}{2})(\xi_0-\xi_1)} = \frac{\mu_2}{\mu_1}\Big(c_l\,\mathrm{e}^{(l+\frac{1}{2})(\xi_0-\xi_2)} - d_l\,\mathrm{e}^{-(l+\frac{1}{2})\xi_0}\Big). \tag{5.48}$$

The force per unit area on the two boundaries is

$$\begin{aligned}\sigma\cdot\hat{\boldsymbol{n}} &= \mu_1(h^{-3/2}\partial_\xi h^{1/2}u_1 + \frac{3\sinh\xi_1}{2R}\Omega^{-1/2}\Omega^{1/2}u_1)_{\xi_1}\boldsymbol{e}_\phi \\ &= \sum_l \mu_1(h^{-3/2}(l+1/2)(a_l\mathrm{e}^{(l+1/2)\xi_1} - b_l) \\ &+ \frac{3\sinh\xi_1}{2R}h^{-1/2}(a_l\mathrm{e}^{(l+1/2)\xi_1} + b_l))_{\xi_1}P_l^1(\cos\eta)\boldsymbol{e}_\phi\end{aligned} \tag{5.49}$$

on ξ_1, while on ξ_2 it is

$$\begin{aligned}\sigma\cdot\hat{\boldsymbol{n}} &= -\mu_2(h^{-3/2}\partial_\xi h^{1/2}u_2 + \frac{3\sinh\xi_2}{2R}h^{-1/2}\Omega^{1/2}u_2)_{\xi_2}\boldsymbol{e}_\phi \\ &= -\sum_l \mu_2(h^{-3/2}(l+1/2)(c_l - d_l\mathrm{e}^{-(l+1/2)\xi_2}) \\ &+ \frac{3\sinh\xi_2}{2R}h^{-1/2}(c_l + d_l\mathrm{e}^{-(l+1/2)\xi_2}))_{\xi_2}P_l^1(\cos\eta)\boldsymbol{e}_\phi.\end{aligned} \tag{5.50}$$

Integrating these quantities over the spheres we find that

$$T_1 = -\pi\mu_1(2R)^{3/2}\sum_l 4l(l+1)a_l, \quad T_2 = -\pi\mu_2(2R)^{3/2}\sum_l 4l(l+1)d_l, \tag{5.51}$$

with the coefficients given by

$$\begin{aligned}a_l &= (2R)^{3/2}\frac{\Big(((\mu_1-\mu_2)\mathrm{e}^{(2l+1)\xi_2} - (\mu_1+\mu_2))\omega_1 + 2\mu_2\mathrm{e}^{(2l+1)\xi_2}\omega_2\Big)}{(\mu_1+\mu_2)(\mathrm{e}^{(2l+1)\xi_1} - \mathrm{e}^{(2l+1)\xi_2}) + (\mu_1-\mu_2)(1-\mathrm{e}^{(2l+1)(\xi_1+\xi_2)})} \\ d_l &= (2R)^{3/2}\frac{\mathrm{e}^{(2l+1)\xi_2}\Big(2\mu_1\omega_1 - ((\mu_1-\mu_2)+(\mu_1+\mu_2)\mathrm{e}^{(2l+1)\xi_1})\omega_2\Big)}{(\mu_1+\mu_2)(\mathrm{e}^{(2l+1)\xi_1} - \mathrm{e}^{(2l+1)\xi_2}) + (\mu_1-\mu_2)(1-\mathrm{e}^{(2l+1)(\xi_1+\xi_2)})},\end{aligned} \tag{5.52}$$

with similar expressions for b_l and c_l. The relationship between the two viscosities μ_1 and μ_2 is conveniently encoded in a single dimensionless parameter,

$$\lambda = \frac{\mu_1-\mu_2}{\mu_1+\mu_2}. \tag{5.53}$$

which can take values between between -1 and 1. At these extreme values one of the two phases is inviscid relative to the other, while at the intermediate value $\lambda = 0$ the two phases have the same viscosity and the interface is negligible.

There does not appear to be a general resummation that regularises the divergence of (5.52). Two special cases, however, may be resummed, namely $\xi_2 \to -\infty$ and $\xi_2 = -\xi_1$, corresponding respectively to a sphere only in one of the two phases, and to both spheres having the same size. Therefore these choices both represent a loss of a degree of freedom, since the two spheres may not be specified independently. In fact we will see that in the latter case it is instructive to think of one of the two spheres as the image of the other under reflection in the boundary. It is worth recalling that the use of bispherical coordinates was already restrictive, since the choice of two spheres of arbitrary size separated by a plane fixes the spatial configuration such that the surfaces of the sphere and the intermediate plane are level sets; hence, fixing the relative sizes of the spheres also fixes their distance from the central plane.

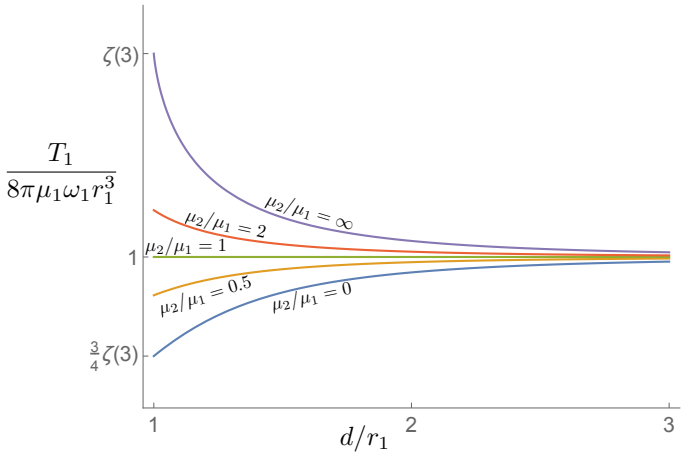

Figure 5.3: The torque on a sphere of radius r_1 in a fluid with viscosity μ_1 when it rotates at rate ω_1 a distance d from the planar interface with another fluid of viscosity μ_2. $\mu_2 > \mu_1$ the torque increases with approach to the boundary, while when $\mu_2 < \mu_1$ torque decreases; the asymptotic approach to the free-space rotation $8\pi\mu_1\omega_1 r_1^3$ is proportional to d^{-3}. Adapted from [115].

When there is only one sphere, $\xi_2 \to -\infty$ and

$$a_l = -\frac{(2R)^{3/2}\omega_1 \mathrm{e}^{-(2l+1)\xi_1}}{1+\lambda \mathrm{e}^{-(2l+1)\xi_1}} = -(2R)^{3/2}\omega_1 \sum_m \mathrm{e}^{-(2l+1)(m+1)\xi_1}(-\lambda)^m \tag{5.54}$$

$$d_l = 0.$$

The torque on the sphere is

$$T_1 = 8\pi\mu_1\omega_1 R^3 \sum_m (-\lambda)^m \sum_l 4l(l+1)\mathrm{e}^{-(2l+1)(m+1)\xi_1} \tag{5.55}$$

$$= 8\pi\mu_1\omega_1 r_1^3 \sum_m (-\lambda)^m \frac{\sinh^3\xi_1}{\sinh^3(m+1)\xi_1}. \tag{5.56}$$

[115] studied precisely this limit, noting that "the more general problem of two spheres one in each phase rotating with unequal angular velocities can be treated by the same method", as shown above.

Resummation is also possible when the two spheres have the same size and are equally far from the interface on either side, in which case $\xi_2 = -\xi_1$ and $r_1 = r_2 \equiv r$.

Then the coefficients become

$$\begin{aligned}
a_l &= \frac{(2R)^{3/2}((\lambda \mathrm{e}^{-(2l+1)\xi_1} - 1)\omega_1 + (1-\lambda)\mathrm{e}^{-(2l+1)\xi_1}\omega_2)}{1 - \mathrm{e}^{-2(2l+1)\xi_1}} \mathrm{e}^{-(2l+1)\xi_1} \\
&= (2R)^{3/2}(\lambda\omega_1 + (1-\lambda)\omega_2) \sum_m \mathrm{e}^{-(2l+1)(2m+2)\xi_1} - (2R)^{3/2}\omega_1 \sum_m \mathrm{e}^{-(2l+1)(2m+1)\xi_1} \\
d_l &= -\frac{(2R)^{3/2}\mathrm{e}^{-2(2l+1)\xi_1}(-(1+\lambda)\omega_1 + (\lambda + \mathrm{e}^{(2l+1)\xi_1})\omega_2)}{1 - \mathrm{e}^{-2(2l+1)\xi_1}} \\
&= ((1+\lambda)\omega_1 - \lambda\omega_2)(2R)^{3/2} \sum_m \mathrm{e}^{-(2l+1)(2m+2)\xi_1} - (2R)^{3/2}\omega_2 \sum_m \mathrm{e}^{-(2l+1)(2m+1)\xi_1},
\end{aligned} \tag{5.57}$$

so now the torques are given by

$$\begin{aligned}
T_1 &= 8\pi\mu_1 r^3 \sum_m \left[\omega_1 \frac{\sinh^3 \xi_1}{\sinh^3 (m+1)\xi_1} - \frac{2(\mu_1\omega_1 + \mu_2\omega_2)\sinh^3 \xi_1}{(\mu_1+\mu_2)\sinh^3(2m+2)\xi_1} \right] \\
T_2 &= 8\pi\mu_2 r^3 \sum_m \left[\omega_2 \frac{\sinh^3 \xi_1}{\sinh^3 (m+1)\xi_1} - \frac{2(\mu_1\omega_1 + \mu_2\omega_2)\sinh^3 \xi_1}{(\mu_1+\mu_2)\sinh^3(2m+2)\xi_1} \right].
\end{aligned} \tag{5.58}$$

The first term in these is the torque close to a no-slip wall, and the other is a reduction in the torque due to the finite viscosity of the other phase. When the two phases have the same composition and the boundary vanishes, $\mu_1 = \mu_2 = \mu$, this expression becomes the rotation of two equal spheres, also given by (5.40), explicitly

$$\begin{aligned}
T_1 &= 8\pi\mu r^3 \sum_m \left[\omega_1 \frac{\sinh^3 \xi_1}{\sinh^3 (2m+1)\xi_1} - \omega_2 \frac{\sinh^3 \xi_1}{\sinh^3(2m+2)\xi_1} \right] \\
T_2 &= 8\pi\mu r^3 \sum_m \left[\omega_2 \frac{\sinh^3 \xi_1}{\sinh^3 (2m+1)\xi_1} - \omega_1 \frac{\sinh^3 \xi_1}{\sinh^3(2m+2)\xi_1} \right].
\end{aligned} \tag{5.59}$$

Thus, by comparison with (5.56), we see that two special cases of rotation near a planar boundary are described by an 'image system': when $\omega_2 = -\omega_1$, (5.58) is the torque close to a no-slip wall, while the rotation close to a free surface is given by $\omega_2 = \omega_1$, as noted by [187].

The more general case where $\xi_0 \neq 0$ is of interest, since it represents the rotation of a sphere inside or outside a bubble of a different fluid; as the flow in this case is still azimuthal and axisymmetric the pressure in each phase is constant, but to sustain the curvature of the bubble's membrane there must be a pressure step across the boundary equal to the Laplace pressure inside the bubble. Taking $p_1 = 0$,

the stress condition on the surface is

$$\mu_1\Big(h^{-\frac{3}{2}}\partial_\xi h^{\frac{1}{2}}u_1+\frac{3\sinh\xi}{2R}h^{-\frac{1}{2}}h^{\frac{1}{2}}u_1\Big)_{\xi=\xi_0}\boldsymbol{e}_\phi$$
$$=\Big(p_2+\frac{2\gamma\sinh\xi_0}{R}\Big)\boldsymbol{e}_\xi+\mu_2\Big(h^{-\frac{3}{2}}\partial_\xi h^{\frac{1}{2}}u_2+\frac{3\sinh\xi}{2R}h^{-\frac{1}{2}}h^{\frac{1}{2}}u_2\Big)_{\xi=\xi_0}\boldsymbol{e}_\phi, \qquad (5.60)$$

so the pressure-balance condition is

$$p_2=-\frac{2\gamma\sinh\xi_0}{R}, \qquad (5.61)$$

where γ is the surface tension.

We have not yet succeeded in finding a closed expression for the flow satisfying the tangential part of eq. (5.60) because the second term on each side depending on $\sinh\xi_0$, which in the case of a planar interface vanished, cannot be expanded in the same Legendre series as the first term, resulting in an infinite set of difference equations determining the coefficients of the flow. It is noted that the condition may be written in the neat form

$$\mu_1\partial_\xi h^{-1}u_1\Big|_{\xi=\xi_0}=\mu_2\partial_\xi h^{-1}u_2\Big|_{\xi=\xi_0}, \qquad (5.62)$$

suggesting that a different expansion of the flow may be useful.

5.2.3 The contact limit

In the limit of vanishing separation where the spheres touch, ξ_1 and ξ_2 both tend to zero in a way that preserves the ratio r_1/r_2,

$$\sinh\xi_1\sim\xi_1, \qquad \sinh\xi_2\sim\mathrm{sgn}(\xi_2)\frac{r_1}{r_2}\xi_1. \qquad (5.63)$$

In this limit (5.40) and (5.41) converge to the finite limiting values

$$T_{1,2}\to\frac{8\pi\mu r_1^3r_2^3}{(r_1+r_2)^3}\Big\{\omega_{1,2}\,\zeta\Big(3,(1+\tfrac{r_{1,2}}{r_{2,1}})^{-1}\Big)-\omega_{2,1}\,\zeta(3)\Big\}, \qquad \xi_2<0<\xi_1, \qquad (5.64)$$

$$T_{1,2}\to\pm\frac{8\pi\mu r_1^3(\omega_1-\omega_2)}{(1-\frac{r_1}{r_2})^3}\zeta\Big(3,(1-\tfrac{r_1}{r_2})^{-1}\Big), \qquad 0\le\xi_2<\xi_1, \qquad (5.65)$$

where $\zeta(s,q)\equiv\sum_{n=0}^{\infty}(n+q)^{-s}$ is the Hurwitz zeta function and $\zeta(s,1)\equiv\zeta(s)$ the Riemann zeta function. That the torque remains finite even when the two spheres touch is due to the fact that the contact point between them has zero area.

That these limits exist may be demonstrated using elementary analysis. We

must show that the limit of the summand exists, and that the sum is uniformly convergent. This then allows exchange of the limit-taking and the summation operations. Consider, for example,

$$\lim_{\xi\to 0}\sum_{n=1}^{\infty}\frac{\sinh^3\xi}{\sinh^3 n\xi}=\zeta(3). \tag{5.66}$$

By L'Hôpital's rule

$$\lim_{\xi\to 0}\frac{\sinh^3\xi}{\sinh^3 n\xi}=\frac{1}{n^3}. \tag{5.67}$$

Since

$$\begin{aligned}\sinh n\xi &\geq n\sinh\xi\geq 0, \qquad &\forall\, n\geq 1,\ \xi\geq 0\\ \sinh n\xi &\leq n\sinh\xi\leq 0, \qquad &\forall\, n\geq 1,\ \xi\leq 0\end{aligned} \tag{5.68}$$

we have that the summand is bounded independently of ξ,

$$\frac{\sinh^3\xi}{\sinh^3 n\xi}\leq\frac{1}{n^3} \qquad \forall\,\xi,\ n\geq 1, \tag{5.69}$$

and therefore forms a uniformly convergent sequence by the Weierstrass M-test. Hence the order of the limit and the summation in the original expression can be interchanged, and

$$\lim_{\xi\to 0}\sum_{n=1}^{\infty}\frac{\sinh^3\xi}{\sinh^3 n\xi}=\sum_{n=1}^{\infty}\lim_{\xi\to 0}\frac{\sinh^3\xi}{\sinh^3 n\xi}=\zeta(3). \tag{5.70}$$

All other limits of this type are found in exactly the same way and will not be shown further.

The solution we have presented for two separate spheres is fully general and allows any combination of torques. For use with the reciprocal theorem we require solutions in which one or the other of the torques is zero. We have been unable to invert (5.40) analytically to give the mobility functions for two external spheres in general, with the exception of the limit of infinite separation where, for $T_2=0$, T_1 is the usual drag on a sphere rotating with angular velocity ω_1 and ω_2 is the asymptotic vorticity due to a rotlet, $(d/r_1)^{-3}\omega_1$, and in the opposite limit of contact, as in (5.64). In practice the value of ω_2 such that T_2 vanishes may be computed numerically and gives the free rotation of sphere 2 due to a torque applied to sphere 1 about their common diameter. These free rotations are tabulated by Jeffery [114].

Where one sphere encloses the other ($\xi_2>0$) the torques on the two spheres

are equal and opposite. This means the left-hand side of (2.9), in the absence of force, becomes $T_1(\tilde{\Omega}_1 - \tilde{\Omega}_2)$ and allows the relative rotation to be determined. It is natural to take the concave boundary to set the frame of reference. In the intermediate limit of a plane ($\xi_2 = 0$) the two solutions (5.64) and (5.65) coincide. As with the enclosed system the torque on the wall is equal and opposite to the torque on the finite-sized sphere.

5.3 Stokes drag solution for two spheres translating about the common diameter

The translational motion of two spheres along their common diameter was first studied by [113] and subsequently adapted for the special case of a sphere sedimenting towards a planar surface [189, 190]. The approach adopted involves the introduction of a streamfunction to solve the continuity equation by construction and then the Stokes equations reduce to a fourth-order operator for the streamfunction. Later studies [110, 116, 146, 192, 193, 197], motivated in part by a desire to extend to translations perpendicular to the common axis, follow the opposite approach: the Stokes equation is first solved by constructing a harmonic vector from an appropriate combination of the flow and the pressure ($\boldsymbol{u} - \frac{1}{2\mu} p\boldsymbol{x}$), the coefficients of which are then to be determined from boundary conditions and the imposition of incompressibility, resulting in a set of second-order difference equations that unfortunately proves analytically intractable. Our own approach here returns to the original method of Stimson & Jeffery in that we first solve the continuity equation, although the exact way we do this differs slightly from their approach and may be viewed as a minor modernisation to the more explicit use of cohomological methods. We also generalise to arbitrary translational speeds V_1 and V_2 and to the full range of geometries allowed by the bispherical coordinate system.

The fluid domain is bounded by two spherical surfaces. In such a region the continuity equation, $\boldsymbol{\nabla} \cdot \boldsymbol{u} = 0$, has solutions where the velocity is the curl of a vector potential and solutions that are not of this form. The latter correspond to volume changes of the two spheres, either compressions or expansions. When the two spheres are external to each other these may evidently be made independently, while if one encloses the other any changes must be correlated so as to preserve the total volume of fluid between them. In formal terms for the former case, the second de Rham cohomology group for the fluid domain is $H^2_{\mathrm{dR}}(\mathbb{R}^3 \backslash \{\mathrm{pt}_1, \mathrm{pt}_2\}) \cong \mathbb{R}^2$ and solutions of the continuity equation are characterised by a pair of real numbers corresponding to these classes, which specify the strengths of the two sources (or

sinks). Representatives of the two classes may be given by converting standard point-singularity expressions [147] into bispherical coordinates. For two sources of equal unit strength we find

$$\boldsymbol{u}_{(1,1)} = \frac{1}{4\pi}\frac{h^{-1/2}}{\sqrt{2}R^{3/2}}\Big\{\big[(1-2\cosh\xi-\cos\eta)\sinh\xi/2\big]\boldsymbol{e}_\xi + \big[\sin\eta\cosh\xi/2\big]\boldsymbol{e}_\eta\Big\}, \quad (5.71)$$

while for a source-sink pair of equal and opposite unit strength we have

$$\boldsymbol{u}_{(1,-1)} = \frac{1}{4\pi}\frac{h^{-1/2}}{\sqrt{2}R^{3/2}}\Big\{\big[(1-2\cosh\xi+\cos\eta)\cosh\xi/2\big]\boldsymbol{e}_\xi - \big[\sin\eta\sinh\xi/2\big]\boldsymbol{e}_\eta\Big\}. \quad (5.72)$$

Thus the most general flow field in this domain may be written

$$\boldsymbol{u} = f\,\boldsymbol{u}_{(1,1)} + g\,\boldsymbol{u}_{(1,-1)} + \boldsymbol{\nabla}\times\boldsymbol{\psi}, \quad (5.73)$$

for an arbitrary pair of real numbers f, g and an arbitrary vector potential $\boldsymbol{\psi}$. Although we do not pursue it here, the full solution would constitute an interesting extension with possible applications to swimming problems where there is an exchange of volume between components of a swimmer, such as the metaboly of *Euglena* [14]. In everything that follows we consider only two spheres of fixed volume, corresponding to the particular solution $f = g = 0$.

Without loss of generality the vector potential can be chosen to be divergence-free, $\boldsymbol{\nabla}\cdot\boldsymbol{\psi} = 0$ (the Lorenz gauge in electromagnetism). Then to satisfy the Stokes equations it must be biharmonic

$$\nabla^4\boldsymbol{\psi} = \boldsymbol{0}. \quad (5.74)$$

We emphasise that this is different to the equation solved by [113] for their stream-function. Solutions of the biharmonic equation may be characterised as follows. If λ is a harmonic function then $z\lambda$ is biharmonic but not harmonic. The same is true for each of the Cartesian coordinates. Thus the general solution of the scalar biharmonic equation can be written

$$\lambda = \lambda_1 + (\nu_1 x + \nu_2 y + \nu_3 z)\lambda_2, \quad (5.75)$$

where λ_1, λ_2 are arbitrary harmonic functions and (ν_1, ν_2, ν_3) is a real constant vector, which without loss of generality can be normalised to unit magnitude. A general biharmonic vector is an arbitrary biharmonic scalar field in each Cartesian direction. Of course, there is a large degree of redundancy in (5.75) since different

choices of the constants ν_1, ν_2, ν_3 can lead to the same biharmonic function λ when coupled to suitable changes in the harmonic functions λ_1, λ_2. To the best of our knowledge, this redundancy is properly understood in terms of sheaf cohomology and Penrose's twistor transform [201], although currently this lies outside our own expertise. In the present situation, the axisymmetry of the problem allows one to see the appropriate choices that should be made.

On grounds of axisymmetry the flow field should have components in the axial (z) and radial (ρ) directions only (equivalently the ξ and η directions), with no azimuthal component, and should be independent of the azimuthal angle ϕ. An appropriate vector potential for such a flow has the form $\boldsymbol{\psi} = \psi(z,\rho)\boldsymbol{e}_\phi$ (uniquely so if we impose Lorenz gauge). We determine the scalar function ψ by writing a suitable biharmonic vector using (5.75),

$$\psi \boldsymbol{e}_\phi = \big[\lambda_1^x - y\lambda_2\big]\boldsymbol{e}_x + \big[\lambda_1^y + x\lambda_2\big]\boldsymbol{e}_y, \tag{5.76}$$

$$= \big[\lambda_1^x \cos\phi + \lambda_1^y \sin\phi\big]\boldsymbol{e}_\rho + \big[\lambda_1^y \cos\phi - \lambda_1^x \sin\phi + \rho\lambda_2\big]\boldsymbol{e}_\phi. \tag{5.77}$$

Thus λ_2 should be independent of ϕ, while λ_1^x and λ_1^y should contain only terms with dependence $\sin\phi$ and $\cos\phi$, respectively, and have equal and opposite coefficients. Using (5.20) together with standard manipulations of the associated Legendre polynomials, the potential can be given in the general form

$$h^{-\frac{1}{2}}\psi = \sum_{l=1}^{\infty}\Big(A_l \mathrm{e}^{(l+\frac{3}{2})\xi} + D_l \mathrm{e}^{-(l+\frac{3}{2})\xi} + B_l \mathrm{e}^{(l-\frac{1}{2})\xi} + C_l \mathrm{e}^{-(l-\frac{1}{2})\xi}\Big) P_l^1(\cos\eta) \tag{5.78}$$

for real constants A_l, B_l, C_l, D_l. The boundary conditions that determine these constants are that the flow should equal the constant translation speeds $V_{1,2}\,\boldsymbol{e}_z$ on the two spheres $\xi = \xi_{1,2}$, and that the normal gradient of flow should vanish on their surfaces. These conditions may be combined into the statement $\boldsymbol{\nabla}(\rho\psi - \frac{1}{2}\rho^2 V_j)_{\xi=\xi_j} = \boldsymbol{0}$ [113], giving four equations to determine the four unknown coefficients, that in our formulation reduce to the 2×2 block-diagonal form

$$\begin{bmatrix} (\mathrm{e}^{(l+\frac{3}{2})\xi_1} + \mathrm{e}^{(l+\frac{3}{2})\xi_2}) & (\mathrm{e}^{(l-\frac{1}{2})\xi_1} + \mathrm{e}^{(l-\frac{1}{2})\xi_2}) \\ (2l+3)(\mathrm{e}^{(l+\frac{3}{2})\xi_1} - \mathrm{e}^{(l+\frac{3}{2})\xi_2}) & (2l-1)(\mathrm{e}^{(l-\frac{1}{2})\xi_1} - \mathrm{e}^{(l-\frac{1}{2})\xi_2}) \end{bmatrix} \begin{bmatrix} A_l + D_l \mathrm{e}^{-(l+\frac{3}{2})(\xi_1+\xi_2)} \\ B_l + C_l \mathrm{e}^{-(l-\frac{1}{2})(\xi_1+\xi_2)} \end{bmatrix}$$

$$= \frac{R}{\sqrt{2}} \begin{bmatrix} \Big(\frac{\mathrm{e}^{-(l+\frac{3}{2})|\xi_1|}}{(2l+3)} - \frac{\mathrm{e}^{-(l-\frac{1}{2})|\xi_1|}}{(2l-1)}\Big)V_1 + \Big(\frac{\mathrm{e}^{-(l+\frac{3}{2})|\xi_2|}}{(2l+3)} - \frac{\mathrm{e}^{-(l-\frac{1}{2})|\xi_2|}}{(2l-1)}\Big)V_2 \\ \mathrm{sgn}(\xi_1)\Big(\mathrm{e}^{-(l-\frac{1}{2})|\xi_1|} - \mathrm{e}^{-(l+\frac{3}{2})|\xi_1|}\Big)V_1 - \mathrm{sgn}(\xi_2)\Big(\mathrm{e}^{-(l-\frac{1}{2})|\xi_2|} - \mathrm{e}^{-(l+\frac{3}{2})|\xi_2|}\Big)V_2 \end{bmatrix} \tag{5.79}$$

and

$$\begin{bmatrix} (\mathrm{e}^{(l+\frac{3}{2})\xi_1} - \mathrm{e}^{(l+\frac{3}{2})\xi_2}) & (\mathrm{e}^{(l-\frac{1}{2})\xi_1} - \mathrm{e}^{(l-\frac{1}{2})\xi_2}) \\ (2l+3)(\mathrm{e}^{(l+\frac{3}{2})\xi_1} + \mathrm{e}^{(l+\frac{3}{2})\xi_2}) & (2l-1)(\mathrm{e}^{(l-\frac{1}{2})\xi_1} + \mathrm{e}^{(l-\frac{1}{2})\xi_2}) \end{bmatrix} \begin{bmatrix} A_l - D_l \mathrm{e}^{-(l+\frac{3}{2})(\xi_1+\xi_2)} \\ B_l - C_l \mathrm{e}^{-(l-\frac{1}{2})(\xi_1+\xi_2)} \end{bmatrix}$$
$$= \frac{R}{\sqrt{2}} \begin{bmatrix} \Big(\frac{\mathrm{e}^{-(l+\frac{3}{2})|\xi_1|}}{(2l+3)} - \frac{\mathrm{e}^{-(l-\frac{1}{2})|\xi_1|}}{(2l-1)}\Big) V_1 - \Big(\frac{\mathrm{e}^{-(l+\frac{3}{2})|\xi_2|}}{(2l+3)} - \frac{\mathrm{e}^{-(l-\frac{1}{2})|\xi_2|}}{(2l-1)}\Big) V_2 \\ \mathrm{sgn}(\xi_1)\Big(\mathrm{e}^{-(l-\frac{1}{2})|\xi_1|} - \mathrm{e}^{-(l+\frac{3}{2})|\xi_1|}\Big) V_1 + \mathrm{sgn}(\xi_2)\Big(\mathrm{e}^{-(l-\frac{1}{2})|\xi_2|} - \mathrm{e}^{-(l+\frac{3}{2})|\xi_2|}\Big) V_2 \end{bmatrix} \tag{5.80}$$

Inversion is straightforward, although we will not give the explicit forms of the coefficients A_l, B_l, C_l, D_l here. For later convenience we record the expression for the fluid velocity in the bispherical basis

$$\begin{aligned} \boldsymbol{u} = \boldsymbol{\nabla} \times \boldsymbol{\psi} = &\Big[h^{-\frac{1}{2}} \frac{1}{\sin\eta} \partial_\eta \big(\sin\eta\, h^{-\frac{1}{2}} \psi\big) - \frac{3\sin\eta}{2R} h^{\frac{1}{2}}.h^{-\frac{1}{2}} \psi\Big] \boldsymbol{e}_\xi \\ &- \Big[h^{-\frac{1}{2}} \partial_\xi \big(h^{-\frac{1}{2}} \psi\big) - \frac{3\sinh\xi}{2R} h^{\frac{1}{2}}.h^{-\frac{1}{2}} \psi\Big] \boldsymbol{e}_\eta. \end{aligned} \tag{5.81}$$

Finally, the pressure at a point $\boldsymbol{x}$ can be computed from the flow field through the integral

$$p(\boldsymbol{x}) = p_\infty + \int_\infty^{\boldsymbol{x}} \mathrm{d}\boldsymbol{l} \cdot \boldsymbol{\nabla} p = p_\infty + \mu \int_\infty^{\boldsymbol{x}} \mathrm{d}\boldsymbol{l} \cdot \nabla^2 \boldsymbol{u}, \tag{5.82}$$

where p_∞ is its asymptotic value, although we will not need to evaluate it explicitly here.

The solution we have presented is equivalent to those given previously [113, 189], although it is not identical because the manner in which we have solved the continuity equation differs slightly. This leads, for instance, to an expansion of the vector potential in associated Legendre polynomials P_l^1, rather than in Gegenbauer polynomials $C_{n+1}^{-1/2}$. In addition the final form we arrive at for determining the coefficients A_l, B_l, C_l, D_l presents the 4×4 problem in block diagonal form, which we have not seen in the previous literature. We feel this offers a modest improvement.

[113] have given an elegant and compact expression for the hydrodynamic drag on the spheres. Unfortunately, we cannot directly adopt their formula as the vector potential we have introduced in the solution of the continuity equation is not identical to their streamfunction. Nonetheless, the final expression for the drag that we obtain is almost the same as theirs. It is found by integrating the normal component of the stress (1.2) over the surfaces $\xi_{1,2}$ and consists of a viscous component F_v due to gradients of the flow, and a component driven by the pressure,

F_p. The former is easy to write down given (5.81),

$$F_{v\,1,2} = \pm\, 4\pi\mu \int_0^\pi \mathrm{d}\eta\, h^2 \sin\eta \Big[\frac{\cosh\xi\cos\eta - 1}{\cosh\xi - \cos\eta} \Big(\frac{1}{h}\partial_\xi u_\xi - \frac{\sin\eta}{R} u_\eta \Big) + \frac{\sinh\xi \sin\eta}{2(\cosh\xi - \cos\eta)} \Big(\frac{1}{h}(\partial_\xi u_\eta + \partial_\eta u_\xi) + \frac{\sin\eta}{R} u_\xi + \frac{\sinh\xi}{R} u_\eta \Big) \Big] \Big|_{\xi=\xi_{1,2}} . \quad (5.83)$$

The contribution of the pressure to the drag is given by the integral

$$F_{p\,1,2} = \pm \boldsymbol{e}_z \cdot \int_0^{2\pi} \mathrm{d}\phi \int_0^\pi \mathrm{d}\eta\, h^2 \sin\eta\, (-p)\, \boldsymbol{e}_\xi \Big|_{\xi=\xi_{1,2}} \quad (5.84)$$

$$= \pm\pi\mu \int_0^\pi \mathrm{d}\eta\, h^3 \sin^2\eta\, (\boldsymbol{e}_\eta \cdot \nabla^2 \boldsymbol{u}) \Big|_{\xi=\xi_{1,2}}, \quad (5.85)$$

where we have used the definition of the pressure, (5.82), and integrated by parts to rewrite this in terms of the flow field which is known. Using the expression (5.81) leads to eight separate contributions involving partial derivatives of the vector potential and half-integer powers of the conformal factor W, which can be expanded in associated Legendre polynomials using various derivatives of (5.26). Thus each term in the integral is written a product of two expansions in Legendre polynomials, and may be evaluated using orthogonality. This is a straightforward but tedious undertaking, and eventually yields a remarkably simple form for the pressure on each sphere,

$$F_{1,2} = \pm 4\pi\mu\sqrt{2R} \sum_{l=1}^{\infty} l(l+1) \begin{cases} -(A_l + B_l), & \xi_{1,2} \geq 0, \\ (C_l + D_l), & \xi_{1,2} < 0. \end{cases} \quad (5.86)$$

When the fluid has a finite volume or in the limiting case of the half-space ($\xi_2 \geq 0$), the net force on the fluid is zero since the contributions from the two boundaries are equal and opposite. This is also seen for a point force in the half-space [147], which is obtained from our solution in the limit $\xi_1 \to \infty$, $\xi_2 \to 0$, with R held constant.

Since the coefficients have exponential decay in ξ_1 and ξ_2 the sums converge rapidly for large separation, however the forces are divergent as the separation vanishes. This limit has been treated in detail by Cox and Brenner [190] for a planar boundary. The force has a leading-order divergence of order ξ_i^{-2}, and a subleading harmonic sum independent of ξ, which can be regularised as a logarithmic dependence on separation. Generalising their method to arbitrary curvature the forces

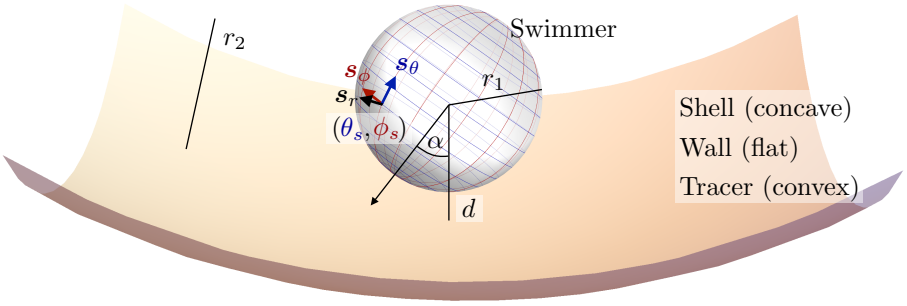

Figure 5.4: A spherical swimmer of radius r_1, located a perpendicular distance d away from the surface of a shell, wall or tracer of radius r_2. The swimmer surface is parametrised by the coordinate (θ_s, ϕ_s) and the swimmer approaches the passive sphere at an angle α to the common diameter.

have the limiting expressions

$$F_1 = 12\pi\mu V_1 r_1 \left(\frac{\xi_1^{-2}}{(1+\frac{r_1}{r_2})^3} - \frac{\left(1 + 7\frac{r_1}{r_2} + \left(\frac{r_1}{r_2}\right)^2\right)}{5(1+\frac{r_1}{r_2})^3} \log \xi_1 \right) \tag{5.87}$$
$$+ \text{ constant \& decaying terms}, \quad \xi_2 < 0 < \xi_1,$$

$$F_1 = 12\pi\mu V_1 r_1 \left(\frac{\xi_1^{-2}}{(1-\frac{r_1}{r_2})^3} - \frac{\left(1 - 7\frac{r_1}{r_2} + \left(\frac{r_1}{r_2}\right)^2\right)}{5(1-\frac{r_1}{r_2})^3} \log \xi_1 \right) \tag{5.88}$$
$$+ \text{ constant \& decaying terms}, \quad 0 \leq \xi_2 < \xi_1,$$

for small separations and $V_2 = 0$.

5.4 Swimmer interactions

5.4.1 Squirming

The results of the previous section for Stokes drag of two spheres allow a variety of axisymmetric swimmer motions to be determined via the reciprocal theorem. For instance, we can explore phenomena such as the circular motion of microorganisms such as *E. coli* close to planar boundaries [40, 43] and free surfaces [42, 44], the hydrodynamics of a daughter colony of *Volvox* inside its parent [39], or the contact interaction of swimmers with passive particles [156]. The contact interaction with a plane is can also shed light on general features of interaction of a swimmer with a large (non-spherical) obstacle, such as a channel of large diameter compared to its size [48, 161] or a post [51]. Many of these problems have been studied asymptotically using leading-order point-singularity descriptions [47, 65, 67], but using

the exact solutions for Stokes drag we can describe the behaviour for arbitrarily small separation, enabling us to understand the role of hydrodynamics in situations of physical contact [48, 51]. Furthermore an exact description allows to assess the accuracy, and therefore utility, of point-singularity approximations.

The reciprocal theorem gives the motion as

$$\begin{aligned}\tilde{U}_1 F_1 + \tilde{U}_2 F_2 + \tilde{\Omega}_1 T_1 + \tilde{\Omega}_2 T_2 = &- \int_0^{2\pi} \mathrm{d}\phi \int_0^{\pi} h^2 \sin\eta \, \mathrm{d}\eta \, (\boldsymbol{u}_{s1} \cdot \boldsymbol{\sigma} \cdot \hat{\boldsymbol{n}})\Big|_{\xi=\xi_1} \\ &- \int_0^{2\pi} \mathrm{d}\phi \int_0^{\pi} h^2 \sin\eta \, \mathrm{d}\eta \, (\boldsymbol{u}_{s2} \cdot \boldsymbol{\sigma} \cdot \hat{\boldsymbol{n}})\Big|_{\xi=\xi_2}, \quad (5.89)\end{aligned}$$

and clearly, since this is linear, to calculate interactions it suffices to calculate the cases $\boldsymbol{u}_{s1} \neq 0, \boldsymbol{u}_{s2} = 0$ and $\boldsymbol{u}_{s1} = 0, \boldsymbol{u}_{s2} \neq 0$ separately and sum them [67]. Hence we shall demonstrate just former of these two cases. The stress tensor is (5.23) for the rotation, or an equivalent expression for the translation.

We consider a swimmer of radius r_1 centred a perpendicular distance d away from the surface of a passive sphere of radius r_2, which may be convex, flat or concave and we respectively term the *tracer*, *wall* or *shell*, as shown in fig. 5.4. The swimmer approaches the surface at an angle α and its squirming motion is described in terms of a local orthonormal basis $\{\boldsymbol{s}_r, \boldsymbol{s}_\theta, \boldsymbol{s}_\phi\}$ and polar coordinate system (θ_s, ϕ_s) relative to this direction. Its slip velocity may be decomposed into squirming modes [75] as

$$\boldsymbol{u}^s = \sum_{n\geq 1} \Big[A_n P_n(\cos\theta_s)\, \boldsymbol{s}_r + B_n V_n(\cos\theta_s)\, \boldsymbol{s}_\theta + r_1 C_n V_n(\cos\theta_s)\, \boldsymbol{s}_\phi \Big], \quad (5.90)$$

where $V_n(x) \equiv -2P_n^1(x)/n(n+1)$ and A_n, B_n and C_n are real coefficients with the units of velocity. The free swimming speed, asymptotically far from the surface, is $U_{\text{free}} = (2B_1 - A_1)/3$ [75, 76]. The addition of the azimuthal modes C_n [77] allows for axial rotation of the swimmer, as seen in several real microorganisms.

To perform the integral in (5.89) it is convenient to express the swimmer's slip velocity in bispherical coordinates. By the spherical cosine rule, the swimmer polar angle satisfies

$$\cos\theta_s = \cos\alpha\cos\beta + \sin\alpha\sin\beta\cos\phi, \quad (5.91)$$

where β is given by eq. (5.7). This relationship is illustrated in figure 5.5. Then,

the surface unit vectors are given by the transformation

$$\begin{bmatrix} \boldsymbol{s}_r \\ \boldsymbol{s}_\theta \\ \boldsymbol{s}_\phi \end{bmatrix} = \begin{bmatrix} -1 & 0 & 0 \\ 0 & \frac{\partial_\beta \cos\theta_s}{\sin\theta_s} & \frac{\sin\alpha\sin\phi}{\sin\theta_s} \\ 0 & \frac{\sin\alpha\sin\phi}{\sin\theta_s} & -\frac{\partial_\beta \cos\theta_s}{\sin\theta_s} \end{bmatrix} \begin{bmatrix} \boldsymbol{e}_\xi \\ \boldsymbol{e}_\eta \\ \boldsymbol{e}_\phi \end{bmatrix}. \tag{5.92}$$

The slip velocity involves Legendre polynomials in $\cos\theta_s$, which can be expanded using the addition theorem for Legendre functions [155],

$$\begin{aligned} P_n(\cos\alpha\cos\beta + \sin\alpha\sin\beta\cos\phi) &= P_n(\cos\alpha)P_n(\cos\beta) \\ &\quad + 2\sum_{m=1}^{n} \frac{(n-m)!}{(n+m)!} P_n^m(\cos\alpha)P_n^m(\cos\beta)\cos m\phi. \end{aligned} \tag{5.93}$$

A number of proofs of this are compiled by Maleček and Nádeník [202]. As the stress tensor in (5.89) is axisymmetric the integral over ϕ can be performed first and only affects the slip velocity, leading to the azimuthally averaged expression

$$\langle \boldsymbol{u}^s \rangle_\phi = -\sum_{n\geq 1} P_n(\cos\alpha)\Big[A_n P_n(\cos\beta)\boldsymbol{e}_\xi + B_n V_n(\cos\beta)\boldsymbol{e}_\eta - r_1 C_n V_n(\cos\beta)\boldsymbol{e}_\phi\Big]. \tag{5.94}$$

It is already clear from (5.94) that the radial and meridional modes A_n and B_n cannot drive axisymmetric rotation, since the normal stress corresponding to a torque, (5.23), is purely azimuthal; similarly the azimuthal modes C_n cannot drive axisymmetric translation. The dependence of the motion on the swimmer's orientation α is a purely geometric factor for each order of squirming mode, and at large separations where higher-order modes may be neglected the orientation dependence is simply $P_2(\cos\alpha)$, in agreement with point-singularity models of swimmer interactions with walls [65, 66].

The contributions from the tangential modes, B_n, C_n, are evaluated straightforwardly (albeit tediously) using orthogonality of Legendre polynomials. The radial modes, A_n, pick up a contribution from the pressure, which may be rewritten in terms of the flow by integrating by parts using the identity

$$h^2 \sin(\eta) P_n(\cos\beta) \equiv -\frac{R^2}{n(n+1)} \partial_\eta \left[\frac{\sin\eta}{\sinh^2\xi} \partial_\eta P_n(\cos\beta)\right]. \tag{5.95}$$

This is a generalisation of the calculation of the pressure contribution to the drag (5.85), which corresponds to the particular case $n = 1$.

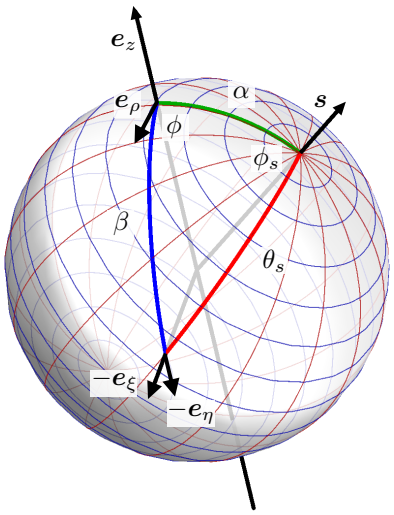

Figure 5.5: If the swimmer's head-tail axis $\boldsymbol{s}$ makes an angle α (green arc) to the global z axis, the point (θ_s, ϕ_s) may be expressed in bispherical coordinates using standard results in spherical trigonometry. The angle β (blue arc) is the rotation mapping the orthogonal unit vectors $(\boldsymbol{e}_z, \boldsymbol{e}_\rho)$ to $(-\boldsymbol{e}_\xi, -\boldsymbol{e}_\eta)$.

5.4.2 Rotation

In this section we calculate explicitly the rotational motion of a squirmer close to a surface. Combined with self-propulsion parallel to the surface this rotation results in circling behaviour, which has been observed experimentally for flagellated bacteria such as *E. coli* and *Vibrio alginolyticus* in close proximity to a planar boundary [40, 43]. The effect is highly local, with the gap between the bacterium and the wall typically much smaller than the size of the bacterium itself. While point-singularity methods predict such behaviour just as a result of the C_2 mode and indeed agree that it should be strongly localised close to the surface, with an inverse-fourth dependence on the separation [66], higher order modes can be expected to play an important role at such small gap widths.

The induced rotation is calculated by performing the integral (5.89) using the slip velocity (5.94) and stress corresponding to rotation, (5.23)

$$\tilde{\Omega}_1 T_1 + \tilde{\Omega}_2 T_2 = -2\pi\mu \sum_{l\geq 2} \sum_{i=1}^{\infty} r_1 C_l P_l(\cos\alpha) \int_0^\pi \sin\eta \,\mathrm{d}\eta \, P_i^1(\cos\eta) V_l(\cos\beta)$$
$$\times \left(h^{\frac{1}{2}}(i+\tfrac{1}{2}) \left(c_i \, \mathrm{e}^{(i+\frac{1}{2})(\xi_1-\xi_2)} - d_i \right) + h^{\frac{3}{2}} \frac{3\sinh\xi}{2R} \left(c_i \, \mathrm{e}^{(i+\frac{1}{2})(\xi_1-\xi_2)} + d_i \right) \right) \Big|_{\xi=\xi_1} . \quad (5.96)$$

The factor of $V_l(\cos\beta)$ may be written as a polynomial of order $l-1$ in the conformal

factor h,

$$V_l(\cos\beta) = \frac{2\sinh\xi\sin\eta}{l(l+1)}\frac{h}{R}P_l'\Big(\cosh\xi - \sinh^2\xi\frac{h}{R}\Big)$$
$$\equiv \frac{2\sin\eta}{l(l+1)}\frac{h}{r_1}\sum_{n=0}^{l-1} w_n(\xi)\Big(\frac{h}{R}\Big)^n, \tag{5.97}$$

where the coefficients $w_n(\xi)$ are calculated using any of the various series representations of Legendre polynomials [154], so that (5.96) becomes

$$\tilde\Omega_1 T_1 + \tilde\Omega_2 T_2 = -2\pi\mu\sum_{l\geq 2}\sum_{n=0}^{l-1}\frac{2R^{\frac{3}{2}}}{l(l+1)}w_n(\xi)\sum_{i=1}^{\infty} C_l P_l(\cos\alpha)$$
$$\times\Bigg((i+\tfrac{1}{2})\Big(c_i\,\mathrm{e}^{(i+\frac{1}{2})(\xi_1-\xi_2)} - d_i\Big)\int_0^\pi \sin\eta\,\mathrm{d}\eta\,P_i^1(\cos\eta)\Big(\frac{h}{R}\Big)^{n+\frac{3}{2}}\sin\eta$$
$$+\frac{3\sinh\xi}{2}\Big(c_i\,\mathrm{e}^{(i+\frac{1}{2})(\xi_1-\xi_2)} + d_i\Big)\int_0^\pi \sin\eta\,\mathrm{d}\eta\,P_i^1(\cos\eta)\Big(\frac{h}{R}\Big)^{n+\frac{5}{2}}\sin\eta\Bigg)\Big|_{\xi=\xi_1}. \tag{5.98}$$

Finally, successive differentiations of the generating function (5.26) give the identity

$$\Big(\frac{h}{R}\Big)^{n+\frac{3}{2}}\sin\eta = \sqrt{2}\frac{(-2)^{n+1}}{(2n+1)!!}\sum_{m=1}^{\infty} P_m^1(\cos\eta)\Big[\frac{1}{\sinh\xi}\partial_\xi\Big]^n \mathrm{e}^{-(m+\frac{1}{2})|\xi|}, \tag{5.99}$$

which reduces (5.96) to a pair of integrals over orthogonal Legendre polynomials. Performing these integrals and resumming the results we find that near a concave shell or wall the motion is

$$(\tilde\Omega_1 - \tilde\Omega_2)T_1 = -8\pi\mu\omega_1 r_1^3\sum_{l\geq 2} C_l P_l(\cos\alpha)\sum_{n=0}^{\infty}\frac{\sinh^3\xi_1\sinh^{l-1}n(\xi_1-\xi_2)}{\sinh^{l+2}(n(\xi_1-\xi_2)+\xi_1)}, \tag{5.100}$$

while for interaction with a tracer it is

$$\tilde\Omega_1 T_1 + \tilde\Omega_2 T_2 = 8\pi\mu r_1^3\sum_{l\geq 2} C_l P_l(\cos\alpha)$$
$$\times\sum_{n=0}^{\infty}\Big[\omega_2\frac{\sinh^3\xi_1\sinh^{l-1}(n(\xi_1-\xi_2)-\xi_2)}{\sinh^{l+2}(n+1)(\xi_1-\xi_2)} - \omega_1\frac{\sinh^3\xi_1\sinh^{l-1}n(\xi_1-\xi_2)}{\sinh^{l+2}(n(\xi_1-\xi_2)+\xi_1)}\Big], \tag{5.101}$$

where the torques are given by (5.40) and (5.41). These expressions are exact, for any separation and any axisymmetric slip velocity. Perhaps the most experimentally relevant limit is that of small separation, approaching contact, which we describe

first.

To find $\tilde{\Omega}_1$, ω_2 must be chosen so that $T_2 = 0$. Conversely, choosing ω_2 such that $T_1 = 0$ allows the tracer motion $\tilde{\Omega}_2$ to be found. With these expressions it is then straightforward to find the limiting rotational speed when the swimmer is in contact with the surface, again using (5.63). For a shell

$$\tilde{\Omega}_1 - \tilde{\Omega}_2 \to -\sum_{l\geq 2} C_l P_l(\cos\alpha) \sum_{k=0}^{l-1} (-1)^k \binom{l-1}{k} \Big(1 - \frac{r_1}{r_2}\Big)^{-k} \frac{\zeta\Big(3+k, \big(1-\frac{r_1}{r_2}\big)^{-1}\Big)}{\zeta\Big(3, \big(1-\frac{r_1}{r_2}\big)^{-1}\Big)} \tag{5.102}$$

and for a tracer

$$\begin{aligned}\tilde{\Omega}_1 \to &-\sum_{l\geq 2} C_l P_l(\cos\alpha) \sum_{k=0}^{l-1} (-1)^k \binom{l-1}{k} \Big(1 + \frac{r_1}{r_2}\Big)^{-k} \\ &\times \left[\frac{\zeta\Big(3, \big(1+\frac{r_2}{r_1}\big)^{-1}\Big)\zeta\Big(3+k, \big(1+\frac{r_1}{r_2}\big)^{-1}\Big) - \zeta(3)\zeta(3+k)}{\zeta\Big(3, \big(1+\frac{r_2}{r_1}\big)^{-1}\Big)\zeta\Big(3, \big(1+\frac{r_1}{r_2}\big)^{-1}\Big) - \zeta(3)^2}\right].\end{aligned} \tag{5.103}$$

It can be readily verified that these coincide for $r_1/r_2 \to 0$ with the value

$$\tilde{\Omega}_1 \to -\sum_{l\geq 2} C_l P_l(\cos\alpha) \sum_{k=0}^{l-1} (-1)^k \binom{l-1}{k} \frac{\zeta(3+k)}{\zeta(3)}, \tag{5.104}$$

representing the rotation of a squirmer touching a no-slip wall.

To illustrate the near-field behaviour that can be found exactly using the reciprocal theorem, we give a specific example of a swimmer whose slip velocity is an azimuthal circulation within a polar cap region of opening angle θ_0. Although crude, this provides a squirmer representation of a rotating flagellar bundle, and counter-rotating cell body. Explicitly, we take the slip velocity to be

$$\boldsymbol{u}^s = \begin{cases} \Omega_c r_1 \sin\theta_s \boldsymbol{s}_\phi, & 0 < \theta_s < \theta_0, \\ -\Omega_b r_1 \sin\theta_s \boldsymbol{s}_\phi, & \theta_0 < \theta_s < \pi, \end{cases} \tag{5.105}$$

as depicted schematically in figure 5.7(a). The slip velocity within the cap region is Ω_c, which is balanced by a counter-rotation of the body, Ω_b, such that the net torque on the swimmer is zero. The squirming coefficients are given by

$$C_l = -\frac{(2l+1)}{4}\left[\Omega_c \int_0^{\theta_0} \mathrm{d}\theta \sin^2\theta P_l^1(\cos\theta) - \Omega_b \int_{\theta_0}^{\pi} \mathrm{d}\theta \sin^2\theta P_l^1(\cos\theta)\right], \tag{5.106}$$

and insisting that the coefficient $C_1 = 0$ we find that the counter-rotation required

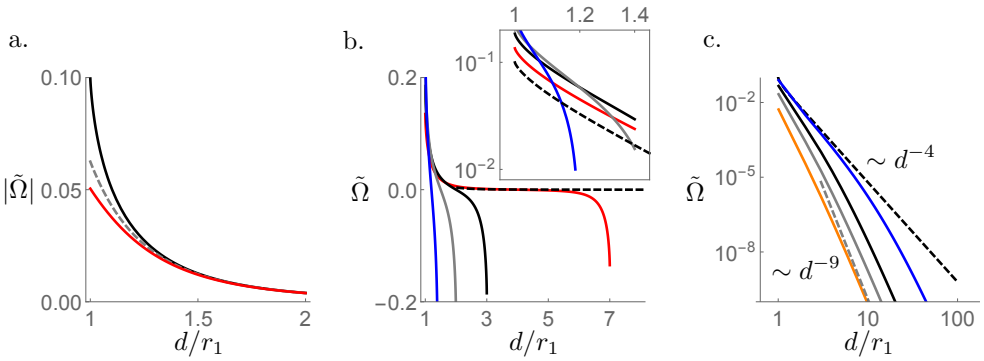

Figure 5.6: The rotational speed, $\tilde{\Omega}$, due to the C_2 squirming mode, in units of $C_2/P_2(\cos\alpha)$, as a function of d. (a) Near a no-slip (black) and free (red) planar boundary, compared to the d^{-4} decay predicted by approximate models (grey dashed). The rotation near a free surface has the opposite sense to that near a solid boundary. (b) Inside a shell of radius 1.2 (blue), 1.5 (grey), 2 (black) and 4 (red), and the wall limit (dashed). Inset: behaviour at small separation. (c) Near a tracer of radius 0.5 (orange), 1 (grey), 2 (black) and 10 (blue), and the wall limit (black dashed).

to cancel out any net torque is

$$\Omega_b = \Omega_c \frac{(2+\cos\theta_0)}{(2-\cos\theta_0)} \tan^4\Big(\frac{\theta_0}{2}\Big). \tag{5.107}$$

When $\theta_0 = \pi/2$ we have that $\Omega_b = \Omega_c$, as expected on symmetry grounds. *E. coli* has a body counter-rotation measured to be on the order of one-tenth the rotation of its flagellar bundle, with large variation between specimens [203], and inversion of (5.107) gives an appropriate value of approximately 0.28π for θ_0, which we idealise as $\pi/4$.

The dependence of the swimmer's rotation on its orientation at large distances is given by the slowest-decaying squirming mode, C_2, and hence by $P_2(\cos\alpha)$, which is head-tail symmetric. However in the near-field there may be significant asymmetry in the orientation-dependence which could persist for relatively large separations. Figure 5.7(b) shows how the orientation-dependence changes for distances up to 100 times the swimmer radius, for a model *E. coli* interacting with a no-slip wall. A comparison between the interaction with a no-slip wall of a spherical-cap swimmer calculated using all modes up to C_{100}, and an equivalent squirming sphere with only the dominant far-field C_2 mode, is shown in figure 5.7(c) and further illustrates the importance of including higher-order modes in calculating near-field interactions: at separations of the order of the swimmer's size the effect

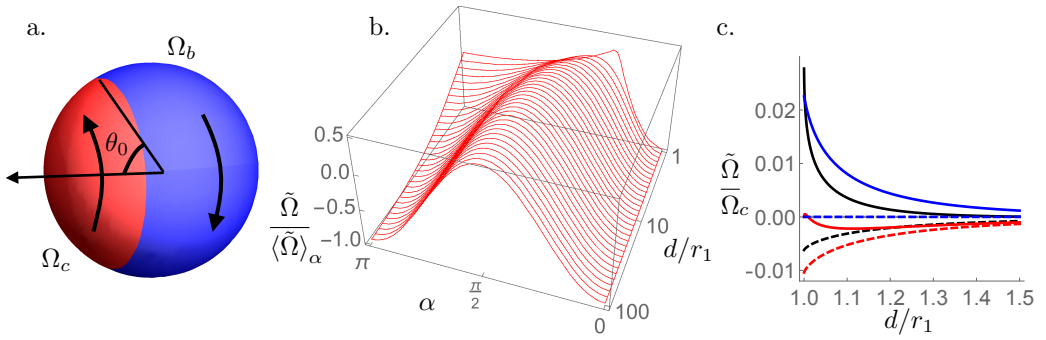

Figure 5.7: The behaviour of a 'spherical cap' type swimmer near a wall, calculated using squirming modes up to C_{100}. (a) Schematic of the swimmer. (b) Orientation-dependence of rotation as a function of distance for $\theta_0 = \pi/4$. Rotation is normalised by the α-average, $\langle\tilde{\Omega}\rangle_\alpha = \sum_l (l+\frac{1}{2})^{-1} \int_0^\pi \mathrm{d}\alpha \, \sin\alpha \, P_l(\cos\alpha)\tilde{\Omega}$. (c) Near-field discrepancy between exact solution (solid) and asymptotic C_2 mode behaviour (dashed) for swimmer with $\theta_0 = \pi/4$ and $\alpha = \pi/4$ (black), $\cos\alpha = 3^{-1/2}$ (blue) and $\cos\alpha = 0.783$ (red).

of including the higher order modes can be dramatic. In the case of $\alpha = \pi/4$ the swimmer's rotation changes sense as it approaches the wall. When $\cos\alpha = 3^{-1/2}$ the contribution of the C_2 mode is identically zero since $P_2(3^{-1/2}) = 0$; however there is still motion driven by higher-order modes of non-negligible magnitude.

5.4.3 Asymptotics at large separation

The flow field generated by the C_l contribution to the slip velocity has an asymptotic decay of $d^{-(l+2)}$ [77], so asymptotically the slowest-decaying contribution to the axisymmetric rotation of a squirmer is from C_2, representing a rotlet dipole. Here we discuss the interaction of this squirming mode with a passive sphere as a leading-order behaviour which is generic for all swimmers.

In Chapter 3 it was found that a squirmer circling parallel to a wall has an asymptotic angular frequency proportional to $C_2 d^{-4}$; figure 5.6(a) shows that this behaviour agrees with our exact solution (5.100) up to a separation of about a squirmer diameter. The behaviour in a shell, shown in figure 5.6(b), also has this form since the separation is always smaller than the redius of curvature of the shell. Note that the rotation of the swimmer when it is precisely in the centre is zero by symmetry and changes sense as the swimmer crosses between hemispheres.

The asymptotic rotation of a swimmer in the presence of a tracer may be calculated using the leading-order forms $\xi_1 \sim \log(r_1/d)$ and $\xi_2 \sim \log(r_2/d)$, giving

a decay of

$$\tilde{\Omega}_1 \sim C_2 P_2(\cos\alpha)\frac{r_1^4 r_2^5}{d^9}. \tag{5.108}$$

Figure 5.6(c) shows a crossover to this behaviour when the separation exceeds the radius of the tracer. In the near-field the passive sphere resembles as a wall and we see a d^{-4} dependence of the swimmer's rotational speed. For the passive sphere (not shown) the crossover is not seen, and the asymptotic interaction is d^{-4}, equal to the asymptotic vorticity generated by a rotlet dipole; thus, the dominant effect of the C_2 squirming mode is the motion of the tracer, and by superposition two squirmers with this slip velocity would tend to move each other more than themselves.

5.4.4 Asymptotic normal rotation using a multipole reflection scheme

The fact that the asymptotic rotation goes as d^{-9} and not d^{-7} can be understood in terms of multipole reflections [92]. At large separation the swimmer's motion is driven by the flow reflected in the tracer, which has the leading behaviour of a stresslet since the tracer must remain force- and torque-free. Dimensional analysis suggests that the reflected flow at the swimmer should have a strength going as d^{-6}, and therefore a vorticity of d^{-7}, but for this case of an axisymmetric, azimuthal flow the leading reflected flow is identically zero, so the rotation is driven by a vorticity of d^{-9}.

In an unbounded fluid, the flow field due to the azimuthal squirming modes is

$$\boldsymbol{e}_\phi \cdot \boldsymbol{u} = \sum_{l=1} r_1 C_l \left(\frac{r_1}{r}\right)^{l+1} V_l(\cos\theta), \tag{5.109}$$

where r is the spherical radius and $\boldsymbol{e}_\phi$ is defined relative to the swimmer's head-tail axis [77]. The slowest-decaying mode is the C_2 mode, so we shall look at this contribution. The swirling flow is

$$\boldsymbol{u}^{(0)} = r_1 C_2 \left(\frac{r_1}{r}\right)^3 \sin(\theta)\cos(\theta)\hat{\boldsymbol{\phi}}, \tag{5.110}$$

where the superscript denotes the order of the reflection.

Particle 1, of radius r_1 and position $\boldsymbol{x}_1$, gives a flow field as described above. By Fáxen's second law the rotation of particle 2, with radius r_2 and position $\boldsymbol{x}_2$ with $|\boldsymbol{x}_2 - \boldsymbol{x}_1| \sim d$, is

$$\Omega_2 = \frac{1}{2}\boldsymbol{\nabla} \times \boldsymbol{u}^{(0)}\Big|_{\boldsymbol{x}=\boldsymbol{x}_2} \sim d^{-4}, \tag{5.111}$$

while its stresslet, which drives the disturbance flow since all the motion must be

force- and torque-free, is

$$\mathsf{S}_2^{(1)} = \frac{20}{3}\pi\mu r_2^3(\boldsymbol{I} + \frac{r_2^2}{10}\nabla^2)\boldsymbol{e}^{(0)}\Big|_{\boldsymbol{x}=\boldsymbol{x}_2} \sim d^{-4} \tag{5.112}$$

where $\boldsymbol{e}^{(0)}$ is the rate-of-strain associated with $\boldsymbol{u}^{(0)}$. The disturbance flow produced by the rotation of the tracer is

$$\boldsymbol{u}^{(1)} = (\mathsf{S}_2^{(1)} \cdot \nabla) \cdot \frac{\mathcal{G}(\boldsymbol{x} - \boldsymbol{x}_2)}{8\pi\mu} \sim d^{-6} \tag{5.113}$$

where

$$\mathcal{G}_{ij}(\mathbf{r}) = \frac{1}{r}\delta_{ij} + \frac{r_i r_j}{r^3}. \tag{5.114}$$

is the Oseen tensor for a point force. In cylindrical coordinates this has the form

$$\mathcal{G} = \frac{(\boldsymbol{e}_\rho\boldsymbol{e}_\rho + \boldsymbol{e}_\phi\boldsymbol{e}_\phi + \boldsymbol{e}_z\boldsymbol{e}_z)}{(\rho^2+z^2)^{1/2}} + \frac{(\rho^2\boldsymbol{e}_\rho\boldsymbol{e}_\rho + \rho z(\boldsymbol{e}_\rho\boldsymbol{e}_z + \boldsymbol{e}_z\boldsymbol{e}_\rho) + z^2\boldsymbol{e}_z\boldsymbol{e}_z)}{(\rho^2+z^2)^{3/2}}. \tag{5.115}$$

The rotation of the tracer is, again using Faxén's second law, asymptotically equal to the vorticity associated with the reflected flow $\boldsymbol{u}^{(1)}$,

$$\boldsymbol{\Omega}_1 \sim \omega^{(1)} \sim \boldsymbol{\nabla} \times \boldsymbol{u}^{(1)}, \tag{5.116}$$

which by naïve dimensional analysis we would expect to decay as d^{-7}.

The leading contribution to $\boldsymbol{u}^{(1)}$ is proportional to

$$[\boldsymbol{e}^{(0)} \cdot \boldsymbol{\nabla}] \cdot \mathcal{G} = \frac{1}{2}\left[\left(\partial_\rho u - \frac{u}{\rho}\right)\left(\boldsymbol{e}_\rho \cdot \frac{1}{\rho}\partial_\phi\mathcal{G} + \boldsymbol{e}_\phi \cdot \partial_\rho\mathcal{G}\right) + \partial_z u\left(\boldsymbol{e}_z \cdot \frac{1}{\rho}\partial_\phi\mathcal{G} + \boldsymbol{e}_\phi \cdot \partial_z\mathcal{G}\right)\right]. \tag{5.117}$$

Using that $\partial_\phi\boldsymbol{e}_\rho = \boldsymbol{e}_\phi$ and $\partial_\phi\boldsymbol{e}_\phi = -\boldsymbol{e}_\rho$, the gradients of the Oseen tensor are

$$\begin{aligned}
\partial_\rho\mathcal{G} &= -\frac{\rho(\boldsymbol{e}_\rho\boldsymbol{e}_\rho + \boldsymbol{e}_\phi\boldsymbol{e}_\phi + \boldsymbol{e}_z\boldsymbol{e}_z)}{(\rho^2+z^2)^{3/2}} + \frac{(2\rho\boldsymbol{e}_\rho\boldsymbol{e}_\rho + z(\boldsymbol{e}_\rho\boldsymbol{e}_z + \boldsymbol{e}_z\boldsymbol{e}_\rho))}{(\rho^2+z^2)^{3/2}} \\
&\quad -\frac{3\rho(\rho^2\boldsymbol{e}_\rho\boldsymbol{e}_\rho + \rho z(\boldsymbol{e}_\rho\boldsymbol{e}_z + \boldsymbol{e}_z\boldsymbol{e}_\rho) + z^2\boldsymbol{e}_z\boldsymbol{e}_z)}{(\rho^2+z^2)^{5/2}}, \\
\frac{1}{\rho}\partial_\phi\mathcal{G} &= \frac{(\rho(\boldsymbol{e}_\phi\boldsymbol{e}_\rho + \boldsymbol{e}_\rho\boldsymbol{e}_\phi) + z(\boldsymbol{e}_\phi\boldsymbol{e}_z + \boldsymbol{e}_z\boldsymbol{e}_\phi))}{(\rho^2+z^2)^{3/2}}, \\
\partial_z\mathcal{G} &= -\frac{z(\boldsymbol{e}_\rho\boldsymbol{e}_\rho + \boldsymbol{e}_\phi\boldsymbol{e}_\phi + \boldsymbol{e}_z\boldsymbol{e}_z)}{(\rho^2+z^2)^{3/2}} + \frac{(\rho(\boldsymbol{e}_\rho\boldsymbol{e}_z + \boldsymbol{e}_z\boldsymbol{e}_\rho) + 2z\boldsymbol{e}_z\boldsymbol{e}_z)}{(\rho^2+z^2)^{3/2}} \\
&\quad -3\frac{z(\rho^2\boldsymbol{e}_\rho\boldsymbol{e}_\rho + \rho z(\boldsymbol{e}_\rho\boldsymbol{e}_z + \boldsymbol{e}_z\boldsymbol{e}_\rho) + z^2\boldsymbol{e}_z\boldsymbol{e}_z)}{(\rho^2+z^2)^{5/2}},
\end{aligned} \tag{5.118}$$

and substitution into (5.117) shows that this contribution is identically zero for any axisymmetric, azimuthal flow. The next highest order contribution to the rotation is proportional to

$$[[\nabla^2 \boldsymbol{e}^{(0)}] \cdot \nabla] \cdot \mathcal{G} \tag{5.119}$$

and goes as d^{-9}, as observed. Note that this is a peculiarity of an axisymmetric motion due to an azimuthal flow; while in principle we have a tilt α breaking the axisymmetry, in using the reciprocal theorem the axisymmetry of the stress tensor means the slip velocity is azimuthally averaged when the integral over the swimmer's surface is carried out.

5.4.5 Rotation near a free surface

An interesting application of the exact solution presented above is to find the rotation of a squirmer close to a free surface. It has been hypothesised [43] and subsequently observed experimentally [44] that the circular trajectories of *E. coli* near a free surface have the opposite sense to those near a no-slip wall. Using the known hydrodynamic solution for the rotation of a sphere beneath the interface between two fluid phases we find that both cases of rotation near a wall and a free surface may be described as image systems, using the two-sphere solution presented previously. This allows the swimming close to such boundaries to be found and compared without further calculation, and we find that the change of direction depending on the type of boundary is generic and explained by these image systems.

If a sphere rotates beneath the flat interface between the fluid that contains it, and another fluid of viscosity $\tilde{\mu}$ [115], the flow may be found explicitly by supposing an ansatz of the form (5.22) in each phase and matching flow and stress across the boundary. Then the torque on the sphere is

$$T_1 = 8\pi\mu\omega_1 r_1^3 \sum_{n=0}^{\infty} (-\Lambda)^n \frac{\sinh^3 \xi_1}{\sinh^3 (n+1)\xi_1}, \tag{5.120}$$

where $\Lambda = (\mu - \tilde{\mu})/(\mu + \tilde{\mu})$. When $\Lambda = -1$ the empty phase is infinitely viscous and corresponds a no-slip wall; instead, when $\Lambda = +1$ the boundary is a free surface. Since the torque (5.40) corresponding to the two-sphere solution when $r_1 = r_2 = r$ is

$$T_1 = 8\pi\mu r^3 \sum_{n=0}^{\infty} \left[\omega_1 \frac{\sinh^3 \xi_1}{\sinh^3 (n+1)\xi_1} - (\omega_1 + \omega_2) \frac{\sinh^3 \xi_1}{\sinh^3 (2n+2)\xi_1} \right], \tag{5.121}$$

it can be seen that the result for a free surface is recovered when $\omega_2 = \omega_1$ [187], while the result for a no-slip wall is given by $\omega_2 = -\omega_1$. Hence a rotating sphere

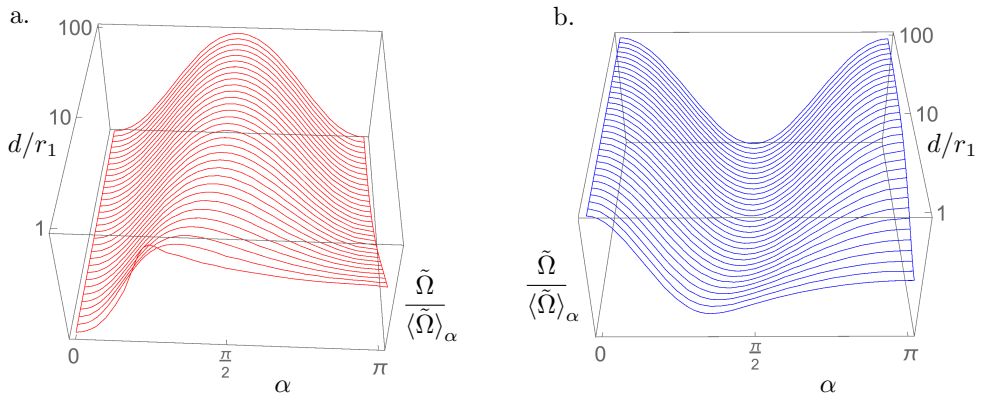

Figure 5.8: The behaviour of a 'spherical cap' type swimmer near (a) a wall and (b) a free surface, calculated using squirming modes up to C_{100}. The spatial decay of the rotation has been removed by dividing by an α-average of the rotation, to isolate the orientation dependence. The sense of the rotation is opposite, and the dependence of the rotation on orientation α is smoother at a free surface than at a wall, since higher-order modes give weaker interactions.

near a free surface has as its image system a corotating sphere which decreases the torque compared to the free-space value, while near a wall the image system is an antirotating sphere which increases the torque.

The rotation near a free surface may then be calculated exactly using the reciprocal theorem and compared to our expressions for squirming near a wall, (5.100). Although the activity of the squirmer generates tangential flows on the interface, since the stress in the conjugate problem is zero there is no contribution to the reciprocal theorem from an integral over the free surface and an expression for the rotation is obtained immediately from (5.101) by substituting $\xi_2 = -\xi_1$ and $\omega_2 = \omega_1$, giving

$$\tilde{\Omega}_1 T_1 = -8\pi\mu r_1^3 \omega_1 \sum_{l=2}^{\infty} \frac{C_l}{r_1} P_l(\cos\alpha) \sum_{n=0}^{\infty} (-1)^n \frac{\sinh^3\xi_1 \sinh^{l-1} n\xi_1}{\sinh^{l+2}(n+1)\xi_1}. \tag{5.122}$$

In both cases of a wall and a free surface the leading far-field contribution from the l-th squirming mode is equal and opposite, with a strength $\tilde{\Omega}_1 \propto (2h)^{-(l+2)}$. Hence the nature of the boundary determines the sense of rotation generically in the asymptotic limit. In the contact limit, which for a wall is given by (5.104) and for a free surface

$$\tilde{\Omega}_1 \to -\frac{4}{3} \sum_{l=2}^{\infty} \frac{C_l}{r_1} P_l(\cos\alpha) \sum_{k=0}^{l-1} (-1)^k \binom{l-1}{k} (1 - 2^{-(k+2)}) \frac{\zeta(3+k)}{\zeta(3)}, \tag{5.123}$$

we find that the contribution to the rotation from each squirming mode is smaller at a free surface than at a wall, and the ratio of these contributions has a faster-than-exponential decay with increasing l, indicating that higher-order effects due to microscopic details of a swimmer are less important at a free surface than at a wall. Fig. 5.6(a) compares the behaviour of the C_2 mode at a free surface with that at a wall, while fig. 5.8 gives a comparison of the behaviour of the spherical-cap swimmer defined in § 5.4.2 at a solid wall and a free surface. It can be seen that the direction of the rotation is opposite, as seen experimentally [44]. Furthermore the dependence of the rotation on orientation α is influenced more by the lower modes at a free surface than at a wall, as evidenced by the smoother profile. In both cases the asymptotic behaviour is proportional to $C_2 P_2(\cos\alpha) d^{-4}$.

The reciprocal theorem relies on the swimmer problem and the conjugate Stokes drag being defined in the same region. Here we have assumed that the free surface does not deform in either solution, so that this region is the half-space with an embedded sphere in both cases; however, there is no reason not to expect deformation, particularly in the close proximity regime and furthermore, it cannot be assumed that this deformation of the surface will be the same for a swimmer and a dragged sphere.

Nevertheless, if the deformation of the surface is small enough that it may be treated in a linear fashion by projecting onto the plane and expressing as a slip velocity (much as Lighthill's deforming squirmer has its activity projected onto the surface of a sphere for determination of the swimming speed [75]), this is not a problem. The swimmer's motion is the sum of an integral of the slip velocity over the swimmer's boundary and an integral of this deformation flow over the free surface, with the stress from the Stokes drag under the free surface as the conjugate solution. As the free surface is, by definition, stress-free, the latter integral does not contribute to the motion. Then, once the swimmer's motion is determined the deformation of the surface may be estimated by some other method. For instance, Crowdy et al. [83] give a detailed two-dimensional treatment of swimming under a free surface using conformal mapping techniques, while Aderogba [122] and Aderogba and Blake [123] find the three-dimensional flow due to a Stokeslet near a fluid interface, calculating the first-order deformation; their approach may be adapted here to an approximate solution of the deformation due to higher-order singularities that correspond to swimming, in particular the stresslet and the source dipole.

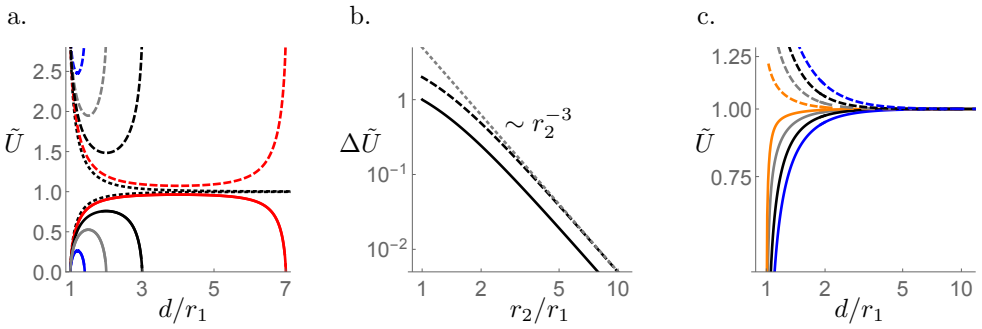

Figure 5.9: The interactions of the A_1 (dashed) and B_1 (solid) modes. (a) The speed $\tilde{U}$ of a squirmer, in units of the free swimming speed U_{free}, as a function of d inside a shell of radius 1.2 (blue), 1.5 (grey), 2 (black), 4 (red). The wall limits are shown as dotted lines. (b) The speed difference $\Delta\tilde{U} = |U_c - U_{\text{free}}|$ at the centre a shell as a function of shell radius r_2, showing an excluded volume dependence. (c) $\tilde{U}$ as a function of d near a tracer of radius 0.5 (orange), 1 (grey), 2 (black) and 10 (blue).

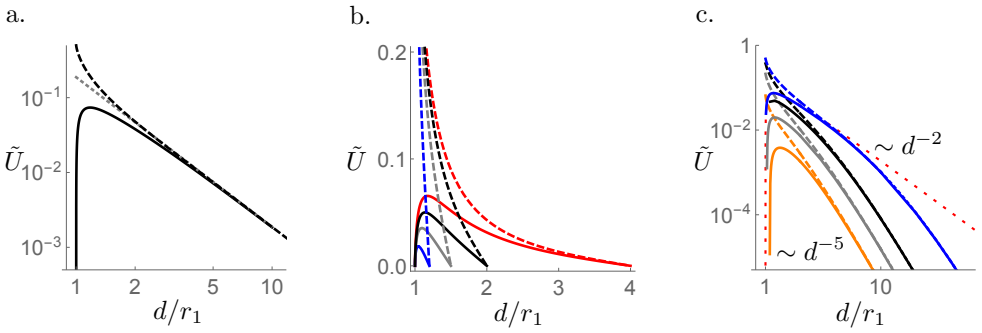

Figure 5.10: The speed $\tilde{U}$ of a squirmer due to modes A_2 and B_2, normalised so that $A_2P_l(\cos\alpha) = B_2P_l(\cos\alpha) = 1$, as a function of d. Dashed line is A_2, solid line is B_2. (a) Interaction with a no-slip wall. Dotted grey line is point-singularity approximation. (b) Interaction with a shell of radius 1.2 (blue), 1.5 (grey), 2 (black) and 4 (red). $\tilde{U} = 0$ in the centre of the shell and the motion is equal and opposite in the other hemisphere. (c) Interaction with a tracer of radius 0.5 (orange), 1 (grey), 2 (black) and 10 (blue), with the red dotted line demonstrating the wall limit.

5.4.6 Translation

The calculation for the translational motion is analogous to the calculation for rotation, but is rather more involved and will not be shown explicitly. The general result for an arbitrary squirming mode has not yet been found and each contribution must be calculated separately. For this reason we consider only the few most important translational squirming modes, A_1, B_1, A_2 and B_2. The first two of these set the self-propulsive speed in free space and asymptotically resemble source dipoles. A_2 and B_2 give the asymptotic stresslet of the swimmer [67] and while they generate no motion in an unbounded domain they are of fundamental importance in the interactions of the swimmer with boundaries, since both the swimmer and the boundaries must remain force-free and the lowest-order image singularity will be a stresslet. In the far-field these point-singularity descriptions are sufficient to fully characterise the generic behaviour [65, 66]. Figures 5.9 and 5.10 show, respectively, the interactions of the A_1 and B_1, and the A_2 and B_2 modes, with a passive sphere.

The flow due to the A_l and B_l modes of a swimmer has the same asymptotic decay in an unbounded fluid, meaning that in a leading-order point-singularity description the radial and polar modes are indistinguishable. The availability of exact solutions means we can estimate the separation beyond which these asymptotic approximations hold. It can be seen from figure 5.9 that beyond a distance of around five swimmer radii the interaction due to A_1 and B_1 coincides, and similarly for A_2 and B_2 in figure 5.10. However the near-field behaviour is dramatically different for the radial and polar modes. The latter have an interaction which goes to zero at the limit of contact, as a result of the divergent drag in this limit. The former have a divergent interaction, resulting from the incompatibility of the boundary conditions of no-slip and radial flow on two touching surfaces.

An interesting consequence of this effect is the behaviour of a swimmer inside a small shell, with a radius smaller than the threshold for crossover to asymptotic behaviour. When a B_1 swimmer is inside such a shell the swimming speed is attenuated by the presence of the boundaries, and by symmetry attains a maximum value, U_c, in the centre of the shell. Conversely, a swimmer with A_1 activity has an increased speed due to the interactions, as a result of the divergent interaction of the radial modes near boundaries. A comparison is shown for a variety of shell sizes in figure 5.9(a). The speed at the centre of the shell, U_c, may be calculated analytically and depends on the relative sizes as

$$U_\mathrm{c} = U_\mathrm{free} - \frac{5}{3}(A_1 + B_1)\Big(\frac{r_1}{r_2}\Big)^3 \left(\frac{1 - \big(\frac{r_1}{r_2}\big)^2}{1 - \big(\frac{r_1}{r_2}\big)^5}\right). \tag{5.124}$$

Thus as the shell becomes large, U_c approaches the free swimming speed in proportion to the volume of fluid displaced by the swimmer, see figure 5.9(b). The same occurs in two dimensions where an exact result is available for the swimming of an active disc inside a circular boundary [66], and where the maximum speed of a self-propulsive swimmer approaches its free-space value in proportion to the excluded area.

The A_2 and B_2 squirming modes generate an asymptotic flow field of d^{-2}, while the propulsive modes A_1 and B_1 give a flow field decaying as d^{-3}. Hence mixing is dominated by the swimmers' dipoles, and the speed of a passive tracer has a dependence of d^{-2}, by Fáxen's law, until the separation becomes small and higher-order effects become important. Since A_2 and B_2 do not drive self-propulsion, the motion of the swimmer resulting from these modes is due to reflected flow in the boundary of the passive sphere. At separations smaller than the tracer's radius of curvature the leading order of the reflected flow is equal to that of the flow itself, and gives rise to a local d^{-2} behaviour. As the separation increases the finite size of the tracer becomes important. Higdon [70] gives the image system for a force dipole in a fixed, finite-sized sphere as the sum of a Stokeslet with leading-order strength proportional to d^{-2} and a dipole with strength $\sim d^{-3}$. Thus, if the passive sphere were fixed the leading order reflection would go as d^{-3}, but as it is free to move in such a way as to cancel any force acting on it, we see d^{-5}. This dependence may also be calculated using a second-order multipole expansion, in which case the leading-order motion of the swimmer is driven by the reflected stresslet inside the tracer [92]. The crossover between the two types of behaviour is shown in figure 5.10(c).

5.5 Discussion

We have found exact expressions for the axisymmetric translation and rotation of a spherical squirmer close to convex, planar or concave no-slip boundary, as well as the axisymmetric rotation beneath a free surface, by making use of the Lorentz reciprocal theorem and the known Stokes drag solutions in these geometries. This covers the hydrodynamics at all separations, including at contact in the case of rotation, and for arbitrary squirming motion. The near-field regime where separations are comparable to the swimmer size or smaller is the regime of greatest relevance to many experimental settings and our exact solution provides rigorous, generic insight. In particular, while the radial and meridional squirming modes show the same asymptotic behaviour, in the near field, at separations smaller than a couple of swimmer diameters, they are markedly different, with the former giving a divergent

interaction strength and the latter a hard repulsion. Azimuthal squirming results in the circling behaviour near boundaries seen in flagellated bacteria and our results describe this situation in some detail. The experimentally reported reversal of orbit direction at a free surface is found to be a generic effect. At large separations, the exact solution reproduces results found previously from asymptotic calculations using point singularity approximations of swimmers and also generalises these to interactions of squirmers with spherical boundaries and tracer particles.

Our solution is founded upon the reciprocal theorem for swimmer problems [89] and appears to be the first application of this method to deduce exact solutions that are not currently available by any other method. Given the widespread significance of hydrodynamic interactions, with confining surfaces and with other organisms, to swimmer motion, there are obvious merits to developing applications of this technique in other settings. For instance, we have only been able to provide a partial solution to the interaction of two swimmers, as the non-axisymmetric components of the motion have not been determined. This is because the solution is founded upon the reciprocal theorem and requires the corresponding Stokes drag problem to be solved. For the non-axisymmetric Stokes drag of two spheres, there is, at present, no exact closed-form solution, although there is a scheme in terms of a set of difference equations that could be solved numerically to any desired degree of accuracy. Such an approach would allow the full hydrodynamic interaction of an arbitrary pair of squirmers to be computed, although not in closed form. Furthermore the large range of validity of the approximate far-field solutions here compared with our exact results indicates that asymptotic estimates are valuable and there is merit to pursuing an approximate approach to find the non-axisymmetric behaviour. This may be done, for instance, by constructing an approximate stress tensor using the solution for a Stokeslet outside a sphere [70], by analogy to the examples given in Chapter 3. The solution presented here may also be supplemented by the axisymmetric translation under a free surface, for which the Stokes drag solution was given by Brenner [189]; while approximate solutions for swimming under a free surface are available [4], since bacteria are known to aggregate at free surfaces [49] an understanding of the contact regime is desirable.

Σε σκέφτομαι κι οι σκέψεις μου, σε σκέψεις μ'έχουν βάλει.
Σε σκέψεις που οι σκέψεις τους, σκέφτονται εσένα πάλι.

Cretan

6

Conclusions and outlook

The reciprocal theorem in principle allows any aspect of swimmer hydrodynamics to be solved, provided an appropriate conjugate solution to the Stokes equations is known. This solution should be for a no-slip object of the same shape in the same domain as the desired swimmer problem; thus, to calculate the motion of a swimming sphere close to a wall using the reciprocal theorem one must use the solution for the Stokes drag on a sphere close to a wall, and so on. By setting the swimmer's surface activity to zero we find the motion of a passive, neutrally buoyant tracer particle, and by taking its size to zero it becomes clear that the reciprocal theorem allows flows to be found. Furthermore, as the leading-order flow in the Stokes drag of any object is a Stokeslet, Stokeslet solutions may be used to find approximate solutions, valid asymptotically, for the motion of swimmers of any shape. This was demonstrated in Chapter 3 to find the flow fields for two types of ciliated walls, corresponding to symplectic and antiplectic metachronal waves, and to study the case of a swimmer near a plane boundary, which has attracted significant experimental and theoretical attention [47, 65]; we then demonstrated a result for the leading-order swimming motion in the fluid between two parallel plates, which despite its heavy level of approximation gives the same qualitative behaviour as the much more detailed numerical model of [163], and illustrates the versatility of the reciprocal theorem. This relied upon having a solution for a point

torque in this geometry, which is a new result.

An advantage of using the reciprocal theorem for calculating motion or interactions is that the swimming stroke, encoded in a slip velocity, may be kept fully arbitrary through the calculation. Thus we were able to find the general solution for the motion of a two-dimensional squirming disc near a wall or inside a circular tank in Chapter 4, based on Crowdy's calculation of the motion of a treadmilling disc near a wall [81]. The only requirement was that the slip velocity be axisymmetric (although the extension to non-axisymmetric slip velocities would be straightforward). This allowed, for instance, calculation of the exact trajectories of a swimmer propelling itself by a short-wavelength surface metachronal wave. Chapter 5 then showed how we can calculate the axisymmetric components of motion for a three dimensional spherical swimmer near a curved boundary or free surface. This confirms that the approximate results of Chapter 3 are valid up to surprisingly small separations, of just a few swimmer radii. The experimentally observed reversal of circling direction of flagellated bacteria at a free surface compared to a solid boundary was found to be a generic effect of axisymmetric azimuthal slip velocity, and not just the rotlet dipole term considered elsewhere in the literature [4, 65].

As with any large investigative work this thesis raises more questions than it answers, and there are many possible avenues that this work could be, and indeed would benefit from being, extended along. The calculation in the second half of Chapter 3 for the interaction of a swimmer with two plates is preliminary and needs more careful treatment from a mathematical point of view to ensure that the various approximations made to the integrals are valid; nevertheless, the excellent correspondence to the results for interaction with a single plate is encouraging, as is the reproduction of behaviour found by much more detailed models [163]. Also, the calculation of the exact solutions for three-dimensional motion in Chapter 5 is missing the non-axisymmetric components. This could be addressed either by adapting the known solutions for parallel translating spheres, despite their issues as discussed previously [116, 197], or by combining the exact solutions for the axisymmetric components with approximate solutions for the non-axisymmetric components, with some confidence that beyond a few swimmer radii of separation this is reasonable, as is demonstrably the case for the axisymmetric components of motion.

The two-dimensional solution presented in Chapter 4 has its utility hampered by Jeffery's paradox, meaning that it cannot be used to find the interactions of two discs. However, there is a literature outlining the procedure to overcome this problem [118, 180, 181] which could be utilised. A further method to regularise two-dimensional problems is to embed the plane of motion in a three-dimensional

fluid [167]; this would be a particularly interesting extension of this work as a description of surface processes on cell membranes.

A more fundamental issue is that the assumption of a slip velocity is itself an approximation, and Lighthill [75] and Blake [151] certainly never intended their squirmer model to be taken as an exact description of any microorganism. More correctly we have some distribution of flagellae on the surface of an organism which exert stress on the fluid. Then the lack of inertia means the reaction force from the fluid results in motion. This formulation is the basis of the boundary-element method, which is analogous to the reciprocal theorem (and in fact is derived using the reciprocal theorem). The slip velocity approximation is a coarse-graining of this surface actuation, and is valid when the swimmer is in an unbounded domain or far from other obstacles. There is no doubt that the slip-velocity description is of great value; however an important question is on the relation between surface stress and slip velocity in a variety of geometries, and in particular in the close-to-contact regime. Liron's model of a carpet of cilia between two plates [152] could be used for this, with the plate separation taken to be small (in the extreme case, similar to the length of the cilia); this work would necessarily be numerical but could inform analytical and approximate models.

Bibliography

[1] M. C. Marchetti, J. F. Joanny, S. Ramaswamy, T. B. Liverpool, J. Prost, M. Rao, and R. A. Simha. Hydrodynamics of soft active matter. *Rev. Mod. Phys.*, 85(3):1143, 2013.

[2] J. Elgeti, Roland G. Winkler, and G. Gompper. Physics of microswimmers—single particle motion and collective behavior: a review. *Rep. Prog. Phys.*, 78(5):056601, 2015.

[3] E. M. Purcell. Life at low Reynolds number. *Am. J. Phys*, 45(1):3–11, 1977.

[4] D. Lopez and E. Lauga. Dynamics of swimming bacteria at complex interfaces. *Phys. Fluids*, 26(7):071902, 2014.

[5] G. I. Taylor. Low-Reynolds-number flows, 1967. no. 21617, The National Committe for Fluid Mechanics Films.

[6] C. M. Pooley, G. P. Alexander, and J. M. Yeomans. Hydrodynamic interaction between two swimmers at low Reynolds number. *Phys. Rev. Lett.*, 99(22): 228103, 2007.

[7] E. Lauga and D. Bartolo. No many-scallop theorem: Collective locomotion of reciprocal swimmers. *Phys. Rev. E*, 78(3):030901, 2008.

[8] G. P. Alexander, C. M. Pooley, and J. M. Yeomans. Scattering of low-Reynolds-number swimmers. *Phys. Rev. E*, 78:045302, 2008.

[9] A. Shapere and F. Wilczek. Geometry of self-propulsion at low Reynolds number. *J. Fluid Mech.*, 198:557–585, 1989.

[10] A. Shapere and F. Wilczek. Efficiencies of self-propulsion at low Reynolds number. *J. Fluid Mech.*, 198:587–599, 1989.

[11] A. M. Leshansky, O. Kenneth, O. Gat, and J. E. Avron. A frictionless microswimmer. *New J. Phys.*, 9(5):145, 2007.

[12] A. M. Leshansky and O. Kenneth. Surface tank treading: Propulsion of Purcell's toroidal swimmer. *Phys. Fluids*, 20(6):063104, 2008.

[13] S. Michelin and E. Lauga. Unsteady feeding and optimal strokes of model ciliates. *J. Fluid Mech.*, 715:1–31, 2013.

[14] J. E. Avron, O. Kenneth, and D. H. Oaknin. Pushmepullyou: an efficient micro-swimmer. *New J. Phys.*, 7(1):234, 2005.

[15] Z. Jia, L. Barbier, H. Stuart, M. Amraei, S. Pelech, J. W. Dennis, P. Metalnikov, P. O'Donnell, and I. R. Nabi. Tumor cell pseudopodial protrusions. localized signaling domains coordinating cytoskeleton remodeling, cell adhesion, glycolysis, rna translocation, and protein translation. *J. Biol. Chem.*, 280(34):30564–30573, 2005.

[16] J. F. De Jonckheere. Molecular definition and the ubiquity of species in the genus naegleria. *Protist*, 155(1):89–103, 2004.

[17] H. C. Berg and R. A. Anderson. Bacteria swim by rotating their flagellar filaments. *Nature*, 245:380–382, 1973.

[18] E. Lauga and C. Eloy. Shape of optimal active flagella. *J. Fluid Mech.*, 730: R1, 2013.

[19] D. R. Brumley, K. Y. Wan, M. Polin, and R. E. Goldstein. Flagellar synchronization through direct hydrodynamic interactions. *eLife*, 3:e02750, 2014.

[20] N. Osterman and A. Vilfan. Finding the ciliary beating pattern with optimal efficiency. *Proc. Natl. Acad. Sci.*, 108(38):15727–15732, 2011.

[21] G. I. Taylor. Analysis of the swimming of microscopic organisms. *Proc. R. Soc. Lond. A*, 209(1099):447–461, 1951.

[22] G. I. Taylor. The action of waving cylindrical tails in propelling microscopic organisms. *Proc. R. Soc. Lond. A*, pages 225–239, 1952.

[23] G. J. Hancock. The self-propulsion of microscopic organisms through liquids. *Proc. R. Soc. Lond. A*, 217(1128):96–121, 1953.

[24] J. R. Blake and M. A. Sleigh. Mechanics of ciliary locomotion. *Biol. Rev.*, 49 (1):85–125, 1974.

[25] M. J. Lighthill. Flagellar hydrodynamics. *SIAM Rev.*, 18(2):161–230, 1976.

[26] C. Brennen and H. Winet. Fluid mechanics of propulsion by cilia and flagella. *Annu. Rev. Fluid Mech.*, 9(1):339–398, 1977.

[27] E. Lauga. Bacterial locomotion. *Annu. Rev. Fluid Mech.*, 48:105—-130, 2016.

[28] Y. Or and R. M. Murray. Dynamics and stability of a class of low Reynolds number swimmers near a wall. *Phys. Rev. E*, 79(4):045302, 2009.

[29] R. Dreyfus, J. Baudry, M. L. Roper, M. Fermigier, H. A. Stone, and J. Bibette. Microscopic artificial swimmers. *Nature*, 437(7060):862–865, 2005.

[30] J. L. Anderson. Colloid transport by interfacial forces. *Ann. Rev. Fluid Mech.*, 21:61–99, 1989.

[31] R. Golestanian, T. B. Liverpool, and A. Adjari. Propulsion of a molecular machine by asymmetric distribution of reaction products. *Phys. Rev. Lett.*, 94:220801, 2005.

[32] S. Ebbens, M. H. Tu, J. R. Howse, and R. Golestanian. Size dependence of the propulsion veocity for catalytic Janus-sphere swimmers. *Phys. Rev. E*, 85 (020401), 2012.

[33] W. F. Paxton, A. Sen, and T. E. Mallouk. Motility of catalytic nanoparticles through self-generated forces. *Chem. Eur. J.*, 11(22):6462–6470, 2005.

[34] J. L. Moran and J. D. Posner. Electrokinetic locomotion due to reaction-induced charge auto-electrophoresis. *J Fluid Mech.*, 680:31–66, 2011.

[35] H.-R. Jiang, N. Yoshinaga, and M. Sano. Active motion of a Janus particle by self-thermophoresis in a defocused laser beam. *Phys. Rev. Lett.*, 105(26): 268302, 2010.

[36] I. Theurkauff, C. Cottin-Bizonne, J. Palacci, C. Ybert, and L. Bocquet. Dynamic clustering in active colloidal suspensions with chemical signalling. *Phys. Rev. Lett.*, 108(268303), 2012.

[37] I. Buttinoni, J. Bialké, F. Kümmel, H. Löwen, C. Bechinger, and T. Speck. Dynamical clustering and phase separation in suspensions of self-propelled colloidal particles. *Phys. Rev. Lett.*, 110:238301, 2013.

[38] E. Lauga and T. R. Powers. The hydrodynamics of swimming microorganisms. *Rep. Prog. Phys.*, 72(9):096601, 2009.

[39] K. Drescher, K. C. Leptos, I. Tuval, T. Ishikawa, T. J. Pedley, and R. E. Goldstein. Dancing *Volvox*: Hydrodynamic bound states of swimming algae. *Phys. Rev. Lett.*, 102(16):168101, 2009.

[40] H. C. Berg. Motile behavior of bacteria. *Phys. Today*, 53(1):24–30, 2000.

[41] Y. Magariyama, M. Ichiba, K. Nakata, K. Baba, T. Ohtani, S. Kudo, and T. Goto. Difference in bacterial motion between forward and backward swimming caused by the wall effect. *Biophys. J*, 88(5):3648–3658, 2005.

[42] W. R. DiLuzio, L. Turner, M. Mayer, P. Garstecki, D. B. Weibel, H. C. Berg, and G. M. Whitesides. *Escherichia coli* swim on the right-hand side. *Nature*, 435(7046):1271–1274, 2005.

[43] E. Lauga, W. R. DiLuzio, G. M. Whitesides, and H. A. Stone. Swimming in circles: motion of bacteria near solid boundaries. *Biophys. J.*, 90(2):400–412, 2006.

[44] R. Di Leonardo, D. Dell'Arciprete, L. Angelani, and V. Iebba. Swimming with an image. *Phys. Rev. Lett.*, 106(3):038101, 2011.

[45] L. Rothschild. Non-random distribution of bull spermatozoa in a drop of sperm suspension. *Nature*, 198(488):1221, 1963.

[46] P. D. Frymier, R. M. Ford, H. C. Berg, and P. T. Cummings. Three-dimensional tracking of motile bacteria near a solid planar surface. *Proc. Natl. Acad. Sci.*, 92(13):6195–6199, 1995.

[47] A. P. Berke, L. Turner, H. C. Berg, and E. Lauga. Hydrodynamic attraction of swimming microorganisms by surfaces. *Phys. Rev. Lett.*, 101:038102, 2008.

[48] P. Denissenko, V. Kantsler, D. J. Smith, and J. Kirkman-Brown. Human spermatozoa migration in microchannels reveals boundary-following navigation. *Proc. Natl. Acad. Sci. U.S.A.*, 109(21):8007–8010, 2012.

[49] G. O'Toole, H. B. Kaplan, and R. Kolter. Biofilm formation as microbial development. *Ann. Rev. Microbiol.*, 54(1):49–79, 2000.

[50] D. Takagi, J. Palacci, A. B. Braunschweig, M. J. Shelley, and J. Zhang. Hydrodynamic capture of microswimmers into sphere-bound orbits. *Soft Matter*, 10:1784, 2014.

[51] M. Contino, E. Lushi, I. Tuval, V. Kantsler, and M. Polin. Microalgae scatter off solid surfaces by hydrodynamic and contact forces. *Phys. Rev. Lett.*, 115 (25):258102, 2015.

[52] L. H. Cisneros, J. O. Kessler, S. Ganguly, and R. E. Goldstein. Dynamics of swimming bacteria: Transition to directional order at high concentration. *Phys. Rev. E*, 83(6):061907, 2011.

[53] C. Dombrowski, L. Cisneros, S. Chatkaew, R. E. Goldstein, and J. O. Kessler. Self-concentration and large-scale coherence in bacterial dynamics. *Phys. Rev. Lett.*, 93(9):098103, 2004.

[54] J. Dunkel, S. Heidenreich, K. Drescher, H. H. Wensink, M. Bär, and R. E. Goldstein. Fluid dynamics of bacterial turbulence. *Phys. Rev. Lett.*, 110(22): 228102, 2013.

[55] H. Wioland, F. G. Woodhouse, J. Dunkel, J. O. Kessler, and R. E. Goldstein. Confinement stabilizes a bacterial suspension into a spiral vortex. *Phys. Rev. Lett.*, 110(26):268102, 2013.

[56] M. B. Wan, C. J. O. Reichhardt, Z. Nussinov, and C. Reichhardt. Rectification of swimming bacteria and self-driven particle systems by arrays of asymmetric barriers. *Phys. Rev. Lett.*, 101(1):018102, 2008.

[57] D. B. Weibel, P. Garstecki, D. Ryan, W. R. DiLuzio, M. Mayer, J. E. Seto, and G. M. Whitesides. Microoxen: Microorganisms to move microscale loads. *Proc. Natl. Acad. Sci.*, 102(34):11963–11967, 2005.

[58] N. Koumakis, A. Lepore, C. Maggi, and R. Di Leonardo. Targeted delivery of colloids by swimming bacteria. *Nat. Commun.*, 4:2588, 2013.

[59] R. Di Leonardo, L. Angelani, D. Dell'Arciprete, G. Ruocco, V. Iebba, S. Schippa, M. P. Conte, F. Mecarini, F. De Angelis, and E. Di Fabrizio. Bacterial ratchet motors. *Proc. Natl. Acad. Sci. U.S.A.*, 107(21):9541–9545, 2010.

[60] T. J. Pedley and J. O. Kessler. Hydrodynamic phenomena in suspensions of swimming microorganisms. *Annu. Rev. Fluid Mech.*, 24:313–358, 1992.

[61] M. E. Cates, D. Marenduzzo, I. Pagonabarraga, and J. Tailleur. Arrested phase separation in reproducing bacteria creates a generic route to pattern formation. *Proc. Natl. Acad. Sci. U.S.A.*, 107(26):11715–11720, 2010.

[62] V. Kantsler, J. Dunkel, M. Polin, and R. E. Goldstein. Ciliary contact interactions dominate surface scattering of swimming eukaryotes. *Proc. Natl. Acad. Sci. U.S.A.*, 110(4):1187–1192, 2013.

[63] G. Li and J. X. Tang. Accumulation of microswimmers near a surface mediated by collision and rotational brownian motion. *Phys. Rev. Lett.*, 103(7):078101, 2009.

[64] R. Zargar, A. Najafi, and M. Miri. Three-sphere low-Reynolds-number swimmer near a wall. *Phys. Rev. E*, 80(2):026308, 2009.

[65] S. E. Spagnolie and E. Lauga. Hydrodynamics of self-propulsion near a boundary: predictions and accuracy of far-field approximations. *J. Fluid Mech.*, 700: 105–147, 2012.

[66] D. Papavassiliou and G. P. Alexander. The many-body reciprocal theorem and swimmer hydrodynamics. *Europhys. Lett.*, 110(4):44001, 2015.

[67] T. Ishikawa, M. P. Simmonds, and T. J. Pedley. Hydrodynamic interaction of two swimming model micro-organisms. *J. Fluid Mech.*, 568:119–160, 2006.

[68] GK Batchelor. Slender-body theory for particles of arbitrary cross-section in stokes flow. *J. Fluid Mech.*, 44(03):419–440, 1970.

[69] R. G. Cox. The motion of long slender bodies in a viscous fluid. Part 1: General theory. *J. Fluid Mech.*, 44(04):791–810, 1970.

[70] J. J. L. Higdon. The generation of feeding currents by flagellar motions. *J. Fluid Mech.*, 94(02):305–330, 1979.

[71] P. G. de Gennes and J. Prost. *The physics of liquid crystals*. Oxford University Press, USA, 1993.

[72] T. Vicsek, A. Czirók, E. Ben-Jacob, I. Cohen, and O. Shochet. Novel type of phase transition in a system of self-driven particles. *Phys. Rev. Lett.*, 75(6): 1226, 1995.

[73] R. Aditi Simha and S. Ramaswamy. Hydrodynamic fluctuations and instabilities in ordered suspensions of self-propelled particles. *Phys. Rev. Lett.*, 89(5): 058101, 2002.

[74] S. Ramaswamy. The mechanics and statistics of active matter. *Annu. Rev. Condens. Matter Phys.*, 1:323–345, 2010.

[75] M. J. Lighthill. On the squirming motion of nearly spherical deformable bodies through liquids at very small Reynolds numbers. *Commun. Pure Appl. Math.*, 5(1052):109–118, 1952.

[76] J. R. Blake. A spherical envelope approach to ciliary propulsion. *J. Fluid Mech.*, 46(1):199–208, 1971.

[77] O. S. Pak and E. Lauga. Generalized squirming motion of a sphere. *J. Eng. Math.*, 88(1):1–28, 2014.

[78] J. R. Blake. Self propulsion due to oscillations on the surface of a cylinder at low Reynolds number. *Bull. Aust. Math. Soc.*, 5(02):255–264, 1971.

[79] D. O. Pushkin, H. Shum, and J. M. Yeomans. Fluid transport by individual microswimmers. *Journal of Fluid Mechanics*, 726:5–25, 2013.

[80] S. E. Spagnolie, G. R. Moreno-Flores, D. Bartolo, and E. Lauga. Geometric capture and escape of a microswimmer colliding with an obstacle. *Soft Matter*, 11(17):3396–3411, 2015.

[81] D. G. Crowdy. Treadmilling swimmers near a no-slip wall at low Reynolds number. *Int. J. Nonlinear Mech.*, 46(4):577–585, 2011.

[82] D. G. Crowdy. Wall effects on self-diffusiophoretic Janus particles: a theoretical study. *J. Fluid Mech.*, 735:473–498, 2013.

[83] D. G. Crowdy, S. Lee, O. Samson, E. Lauga, and A. E. Hosoi. A two-dimensional model of low-Reynolds number swimming beneath a free surface. *J. Fluid Mech.*, 681:24–47, 2011.

[84] M. N. Popescu, S. Dietrich, and G. Oshanin. Confinement effects on diffusiophoretic self-propellers. *J. Chem. Phys.*, 130(19):194702, 2009.

[85] M. N. Popescu, S. Dietrich, M. Tasinkevych, and J. Ralston. Phoretic motion of spheroidal particles due to self-generated solute gradients. *Eur. Phys. J. E*, 31(4):351–367, 2010.

[86] A. Kanevsky, M. J. Shelley, and A.-K. Tornberg. Modeling simple locomotors in Stokes flow. *J. Comput. Phys.*, 229(4):958–977, 2010.

[87] D. Pimponi, M. Chinappi, P. Gualtieri, and C. M. Casciola. Hydrodynamics of flagellated microswimmers near free-slip interfaces. *J. Fluid Mech.*, 789: 514–533, 2016.

[88] J. Happel and H. Brenner. *Low Reynolds number hydrodynamics*. Martinus Nijhoff, 1983.

[89] H. A. Stone and A. D. T. Samuel. Propulsion of microorganisms by surface distortions. *Phys. Rev. Lett.*, 77(19):4102–4104, 1996.

[90] H. A. Lorentz. *Eene algemeene stelling omtrent de beweging eener vloeistof met wrijving en eenige daaruit afgeleide gevolgen*. Koninklijke Akademie van Wetenschappen, 1896.

[91] C. Pozrikidis. *Boundary integral and singularity methods for linearized viscous flow*. Cambridge University Press, 1992.

[92] S. Kim and S. J. Karrila. *Microhydrodynamics: principles and selected applications*. Courier Corporation, 2013.

[93] J. R. Barber. The reciprocal theorem. In *Elasticity*, pages 517–528. Springer, 2010.

[94] T. M. Squires and M. Z. Bazant. Induced-charge electro-osmosis. *J. Fluid Mech.*, 509:217–252, 2004.

[95] R. Golestanian, T. B. Liverpool, and A. Adjari. Designing phoretic micro-and nano-swimmers. *New J. Phys.*, 9(5):126, 2007.

[96] B. U. Felderhof. Instantaneous swimming velocity of a body at low Reynolds number. *Eur. J. Mech. B–Fluid*, 32:88–90, 2012.

[97] H. Lamb. *Hydrodynamics*. Cambridge University Press, 1932.

[98] K. M. Ehlers, A. D. Samuel, H. C. Berg, and R. Montgomery. Do cyanobacteria swim using traveling surface waves? *Proc. Natl. Acad. Sci.*, 93(16):8340–8343, 1996.

[99] T. M. Squires and M. Z. Bazant. Breaking symmetries in induced-charge electro-osmosis and electrophoresis. *J. Fluid Mech.*, 560:65–101, 2006.

[100] I. Proudman and J. R. A. Pearson. Expansions at small Reynolds numbers for the flow past a sphere and a circular cylinder. *J. Fluid Mech.*, 2(03):237–262, 1957.

[101] H. Masoud and H. A. Stone. A reciprocal theorem for Marangoni propulsion. *J. Fluid Mech.*, 741:R4, 2014.

[102] E. Lauga. Locomotion in complex fluids: Integral theorems. *Phys. Fluids*, 26 (8):081902, 2014.

[103] M. N. Popescu, M. Tasinkevych, and S. Dietrich. Pulling and pushing a cargo with a catalytically active carrier. *Europhys. Lett.*, 95(2):28004, 2011.

[104] S. Michelin and E. Lauga. Autophoretic locomotion from geometric asymmetry. *Eur. Phys. J. E*, 38(2):1–16, 2015.

[105] S. Michelin and E. Lauga. A reciprocal theorem for boundary-driven channel flows. *Phys. Fluids*, 27(11):111701, 2015.

[106] G. J. Elfring and E. Lauga. Theory of locomotion through complex fluids. In *Complex Fluids in Biological Systems*, pages 283–317. Springer, 2015.

[107] D. J. Jeffrey and Y. Onishi. The slow motion of a cylinder next to a plane wall. *Q. J. Mech. Appl. Math.*, 34(2):129–137, 1981.

[108] W. H. Pell and L. E. Payne. On Stokes flow about a torus. *Mathematika*, 7 (01):78–92, 1960.

[109] J. M. Dorrepaal, S. R. Majumdar, M. E. O'Neill, and K. B. Ranger. A closed torus in Stokes flow. *Q. J. Mech. Appl. Math.*, 29(4):381–397, 1976.

[110] S. R. Majumdar and M. E. O'Neill. On axisymmetric Stokes flow past a torus. *Z. Angew. Math. Phys.*, 28(4):541–550, 1977.

[111] L. E. Payne and W. H. Pell. The Stokes flow problem for a class of axially symmetric bodies. *J. Fluid Mech.*, 7(04):529–549, 1960.

[112] R. P. Kanwal. Slow steady rotation of axially symmetric bodies in a viscous fluid. *Journal of Fluid Mechanics*, 10(01):17–24, 1961.

[113] M. Stimson and G. B. Jeffery. The motion of two spheres in a viscous fluid. *Proc. R. Soc. Lond. A*, 111:110–116, 1926.

[114] G. B. Jeffery. On the steady rotation of a solid of revolution in a viscous fluid. *Proc. London Math. Soc.*, 2(1):327–338, 1915.

[115] M. E. O'Neill and K. B. Ranger. On the rotation of a rotlet or sphere in the presence of an interface. *Int. J. Multiphas. Flow*, 5(2):143–148, 1979.

[116] M. E. O'Neill and R. Majumdar. Asymmetrical slow viscous fluid motions caused by the translation or rotation of two spheres. Part I: The determination of exact solutions for any values of the ratio of radii and separation parameters. *Z. Angew. Math. Phys.*, 21(2):164–179, 1970.

[117] G. B. Jeffery. The rotation of two circular cylinders in a viscous fluid. *Proc. R. Soc. Lond. A*, 101(709):169–174, 1922.

[118] E. J. Watson. The rotation of two circular cylinders in a viscous fluid. *Mathematika*, 42:105–105, 1995.

[119] G. T. Symm. Conformal mapping of doubly connected domains. *Numer. Math.*, 13:448–457, 1969.

[120] J. R. Blake. A note on the image system for a stokeslet in a no-slip boundary. *Math. Proc. Cambridge*, 70(02):303–310, 1971.

[121] N. Liron and S. Mochon. Stokes flow for a Stokeslet between two parallel flat plates. *J. Eng. Math.*, 10(4):287–303, 1976.

[122] K. Aderogba. On stokeslets in a two-fluid space. *J. Eng. Math.*, 10(2):143–151, 1976.

[123] K. Aderogba and J. R. Blake. Action of a force near the planar surface between two semi-infinite immiscible liquids at very low Reynolds numbers. *Bull. Aust. Math. Soc.*, 18(03):345–356, 1978.

[124] N. Liron and R. Shahar. Stokes flow due to a Stokeslet in a pipe. *J. Fluid Mech.*, 86(04):727–744, 1978.

[125] N. Liron. Stokeslet arrays in a pipe and their application to ciliary transport. *J. Fluid Mech.*, 143:173–195, 1984.

[126] L. J. Fauci and R. Dillon. Biofluidmechanics of reproduction. *Annu. Rev. Fluid Mech.*, 38:371–394, 2006.

[127] D. G. Crowdy and Y. Or. Two-dimensional point singularity model of a low-Reynolds-number swimmer near a wall. *Phys. Rev. E*, 81:036313, 2010.

[128] A. M. J. Davis and D. G. Crowdy. Stresslet asymptotics for a treadmilling swimmer near a two-dimensional corner: hydrodynamic bound states. *Proc. R. Soc. A*, 468(2148):3765–3783, 2012.

[129] A. M. J. Davis and D. G. Crowdy. Matched asymptotics for a spherical low-Reynolds-number treadmilling swimmer near a rigid wall. *IMA J. Appl. Math.*, 80(3):634–650, 2015.

[130] K. Drescher, R. E. Goldstein, N. Michel, M. Polin, and I. Tuval. Direct measurement of the flow field around swimming microorganisms. *Phys. Rev. Lett.*, 105:168101, 2010.

[131] A. T. Chwang and T. Y. T. Wu. Hydromechanics of low-Reynolds-number flow. Part 2. Singularity method for Stokes flows. *J. Fluid Mech.*, 67(04): 787–815, 1975.

[132] G. K. Batchelor. The stress system in a suspension of force-free particles. *J. Fluid Mech.*, 41(03):545–570, 1970.

[133] T. Pedley, D. Brumley, and T. Ishikawa. Squirmers with swirl: a model for *Volvox* swimming. *Bull. Am. Phys. Soc.*, 59, 2014.

[134] N. G. Chisholm, D. Legendre, E. Lauga, and A. S. Khair. A squirmer across Reynolds numbers. *J. Fluid Mech. (to appear)*, 2016.

[135] D. R. Brumley, M. Polin, T. J. Pedley, and R. E. Goldstein. Hydrodynamic synchronization and metachronal waves on the surface of the colonial alga Volvox carteri. *Phys. Rev. Lett.*, 109(26):268102, 2012.

[136] D. R. Brumley, M. Polin, T. J. Pedley, and R. E. Goldstein. Metachronal waves in the flagellar beating of Volvox and their hydrodynamic origin. *J. Roy. Soc. Interface*, 12(108):20141358, 2015.

[137] G. Li and A. M. Ardekani. Hydrodynamic interaction of microswimmers near a wall. *Phys. Rev. E*, 90(1):013010, 2014.

[138] D. G. Crowdy and O. Samson. "stokes flows past gaps in a wall". *Proc. R. Soc. Lond. A*, 466:2727–2746, 2010.

[139] D. G. Crowdy and A. M. J. Davis. Stokes flow singularities in a two-dimensional channel: a novel transform approach with application to microswimming. *Proc. R. Soc. Lond. A*, 469(2157):20130198, 2013.

[140] A. M. J. Davis and D. G. Crowdy. Matched asymptotics for a treadmilling low-reynolds-number swimmer near a wall. *Q. J. Mech. Appl. Math.*, 66(1): 53–73, 2013.

[141] W. M. Hicks. On the motion of two spheres in a fluid. *Phil. Trans. R. Soc. A*, 171:455–492, 1880.

[142] A. B. Basset. On the motion of two spheres in a liquid, and allied problems. *Proc. London Math. Soc.*, 1(1):369–377, 1886.

[143] M. A. Sleigh, J. R. Blake, and N. Liron. The propulsion of mucus by cilia. *Am. Rev. Respir. Dis.*, 137(3):726–741, 1988.

[144] J. Branscomb and A. Alexeev. Designing ciliated surfaces that regulate deposition of solid particles. *Soft Matter*, 6(17):4066–4069, 2010.

[145] A. Alexeev, J. M. Yeomans, and A. C. Balazs. Designing synthetic, pumping cilia that switch the flow direction in microchannels. *Langmuir*, 24(21):12102–12106, 2008.

[146] M. E. O'Neill and S. R. Majumdar. Asymmetrical slow viscous fluid motions caused by the translation or rotation of two spheres. Part II: Asymptotic forms of the solutions when the minimum clearance between the spheres approaches zero. *Z. Angew. Math. Phys.*, 21(2):180–187, 1970.

[147] J. R. Blake and A. T. Chwang. Fundamental singularities of viscous flow. *J. Eng. Math.*, 8(1):23–29, 1974.

[148] P. M. Morse and H. Feshbach. *Methods of theoretical physics*. McGraw-Hill, 1953.

[149] K. Ishimoto and E. A. Gaffney. Squirmer dynamics near a boundary. *Phys. Rev. E*, 88(6):062702, 2013.

[150] S. Gueron, K. Levit-Gurevich, N. Liron, and J. J. Blum. Cilia internal mechanism and metachronal coordination as the result of hydrodynamical coupling. *Proc. Natl. Acad. Sci.*, 94(12):6001–6006, 1997.

[151] J. R. Blake. A model for the micro-structure in ciliated organisms. *J. Fluid Mech.*, 55(01):1–23, 1972.

[152] N. Liron. Fluid transport by cilia between parallel plates. *J. Fluid Mech.*, 86 (04):705–726, 1978.

[153] N. Liron and S. Mochon. The discrete-cilia approach to propulsion of ciliated micro-organisms. *J. Fluid Mech.*, 75(03):593–607, 1976.

[154] E. T. Whittaker and G. N. Watson. *A course of modern analysis*. Cambridge University Press, 1996.

[155] I. N. Sneddon. *Special functions of mathematical physics and chemistry*. Oliver and Boyd, 1956.

[156] X.-L. Wu and A. Libchaber. Particle diffusion in a quasi-two-dimensional bacterial bath. *Phys. Rev. Lett.*, 84(13):3017, 2000.

[157] I. S. Aranson, A. Sokolov, J. O. Kessler, and R. E. Goldstein. Model for dynamical coherence in thin films of self-propelled microorganisms. *Phys. Rev. E*, 75(4):040901, 2007.

[158] M. Leoni and T. B. Liverpool. Swimmers in thin films: from swarming to hydrodynamic instabilities. *Phys. Rev. Lett.*, 105(23):238102, 2010.

[159] J. Liu, R. M. Ford, and J. A. Smith. Idling time of motile bacteria contributes to retardation and dispersion in sand porous medium. *Environ. Sci. Technol.*, 45(9):3945–3951, 2011.

[160] Francisco Guarner and Juan-R Malagelada. Gut flora in health and disease. *Lancet*, 361(9356):512–519, 2003.

[161] S. Jana, S. H. Um, and S. Jung. Paramecium swimming in capillary tube. *Phys. Fluids*, 24(4):041901, 2012.

[162] H. Shum and E. A. Gaffney. Hydrodynamic analysis of flagellated bacteria swimming near one and between two no-slip plane boundaries. *Phys. Rev. E*, 91(3):033012, 2015.

[163] J. de Graaf, A. J. T. M. Mathijssen, M. Fabritius, H. Menke, C. Holm, and T. N. Shendruk. Understanding the onset of oscillatory swimming in microchannels. *Soft Matter*, 2016.

[164] G. N. Watson. *A treatise on the theory of Bessel Functions*. Cambridge University Press, 1948.

[165] L. Zhu, E. Lauga, and L. Brandt. Low-reynolds-number swimming in a capillary tube. *J. Fluid Mech.*, 726:285–311, 2013.

[166] A. A. Tchieu, D. G. Crowdy, and A. Leonard. Fluid-structure interaction of two bodies in an inviscid fluid. *Phys. Fluids*, 22(10):107101, 2010.

[167] P. G. Saffman. Brownian motion in thin sheets of viscous fluid. *Journal of Fluid Mechanics*, 73(04):593–602, 1976.

[168] Y. Or, S. Zhang, and R. M. Murray. Dynamics and stability of low-Reynolds-number swimming near a wall. *SIAM J. Appl. Dyn. Syst.*, 10(3):1013–1041, 2011.

[169] D. G. Crowdy and O. Samson. "hydrodynamic bound states of a low-reynolds-number swimmer near a gap in a wall". *J. Fluid Mech.*, 667:309–335, 2010.

[170] D. G. Crowdy. Exact solutions for cylindrical 'slip–stick' Janus swimmers in Stokes flow. *J. Fluid Mech.*, 719:R2, 2013.

[171] S. Tanveer and G. L. Vasconcelos. Time-evolving bubbles in two-dimensional Stokes flow. *J. Fluid Mech.*, 301:325–344, 1995.

[172] M. Siegel. Influence of surfactant on rounded and pointed bubble in two-dimensional Stokes flow. *SIAM J. Appl. Math.*, 59(6):1998–2027, 1999.

[173] R. Bouffanais and D. K. P. Yue. Hydrodynamics of cell-cell mechanical signaling in the initial stages of aggregation. *Phys. Rev. E*, 81(4):041920, 2010.

[174] G. K. Batchelor. *An introduction to fluid dynamics*. Cambridge University Press, 2000.

[175] W. E. Langlois. *Slow viscous flow*. Macmillan, 1964.

[176] J. R. Philip. Flows satisfying mixed no-slip and no-shear conditions. *Z. Angew. Math. Phys.*, 23(3):353–372, 1972.

[177] DW Bechert and M Bartenwerfer. The viscous flow on surfaces with longitudinal ribs. *J. Fluid Mech.*, 206:105–129, 1989.

[178] D. G. Crowdy and J. Marshall. "analytical formulae for the kirchhoff-routh path function in multiply connected domains". *Proc. R. Soc. A*, 461:2477–2501, 2005.

[179] D. G. Crowdy and J. Marshall. Conformal mappings between canonical multiply connected domains. *Comput. Meth. Funct. Th.*, 6(1):59–76, 2006.

[180] Y. Ueda, A. Sellier, T. Kida, and M. Nakanishi. On the low-Reynolds-number flow about two rotating circular cylinders. *J. Fluid Mech.*, 495:255–281, 2003.

[181] A. Umemura. Matched-asymptotic analysis of low-Reynolds-number flow past two equal circular cylinders. *J. Fluid Mech.*, 121:345–363, 1982.

[182] S. H. Smith. The Jeffery paradox as the limit of a three-dimensional Stokes flow. *Phys. Fluids A*, 2(5):661–665, 1990.

[183] K. Ishimoto and E. A. Gaffney. Swimming efficiency of spherical squirmers: Beyond the Lighthill theory. *Phys. Rev. E*, 90(1):012704, 2014.

[184] S. H. Smith. The rotation of two circular cylinders in a viscous fluid. *Mathematika*, 38(01):63–66, 1991.

[185] S. H. Smith. A note on the Jeffery paradox. *Mathematika*, 34(02):178–186, 1987.

[186] G. B. Jeffery. Plane stress and plane strain in bipolar co-ordinates. *Phil. Trans. R. Soc. A*, 221:265–293, 1921.

[187] H. Brenner. Slow viscous rotation of an axisymmetric body within a circular cylinder of finite length. *Appl. Sci. Res.*, 13(1):81–120, 1964.

[188] J. Happel and R. Pfeffer. The motion of two spheres following each other in a viscous fluid. *AIChE J.*, 6:129–133, 1960.

[189] H. Brenner. The slow motion of a sphere through a viscous fluid towards a plane surface. *Chem. Eng. Sci.*, 16(3):242–251, 1961.

[190] R . G. Cox and H. Brenner. The slow motion of a sphere through a viscous fluid towards a plane surface - II. Small gap widths, including inertial effects. *Chem. Eng. Sci.*, 22(12):1753–1777, 1967.

[191] M. B. A. Cooley and M. E. O'Neill. On the slow motion of two spheres in contact along their line of centres through a viscous fluid. *Math. Proc. Cambridge*, 66(02):407–415, 1969.

[192] W. R. Dean and M. E. O'Neill. A slow motion of viscous liquid caused by the rotation of a solid sphere. *Mathematika*, 10(01):13–24, 1963.

[193] M. E. O'Neill. A slow motion of viscous liquid caused by a slowly moving solid sphere. *Mathematika*, 11(01):67–74, 1964.

[194] A. J. Goldman, R. G. Cox, and H. Brenner. The slow motion of two identical arbitrarily oriented spheres through a viscous fluid. *Chem. Eng. Sci.*, 21: 1151–1170, 1966.

[195] A. J. Goldman, Raymond G. Cox, and H. Brenner. Slow viscous motion of a sphere parallel to a plane wall - I. Motion through a quiescent fluid. *Chem. Eng. Sci.*, 22(4):637–651, 1967.

[196] A. J. Goldman, R. G. Cox, and H. Brenner. Slow viscous motion of a sphere parallel to a plane wall - II. Couette flow. *Chem. Eng. Sci.*, 22(4):653–660, 1967.

[197] M. E. O'Neill and K. Stewartson. On the slow motion of a sphere parallel to a nearby plane wall. *J. Fluid Mech.*, 27(04):705–724, 1967.

[198] G. B. Jeffery. On a form of the solution of Laplace's equation suitable for problems relating to two spheres. *Proc. R. Soc. Lond. A*, pages 109–120, 1912.

[199] G. Rückner and R. Kapral. Chemically powered nanodimers. *Phys. Rev. Lett.*, 98(15):150603, 2007.

[200] L. F. Valadares, Y.-G. Tao, N. S. Zacharia, V. Kitaev, F. Galembeck, R. Kapral, and G. A. Ozin. Catalytic Nanomotors: Self-Propelled Sphere Dimers. *Small*, 6(4):565–572, 2010.

[201] R. S. Ward and R. O. Wells Jr. *Twistor geometry and field theory.* Cambridge University Press, 1991.

[202] K. Maleček and Z. Nádeník. On the inductive proof of Legendre addition theorem. *Stud. Geophys. Geod.*, 45(1):1–11, 2001.

[203] Y. Magariyama, S. Sugiyama, and S. Kudo. Bacterial swimming speed and rotation rate of bundled flagella. *FEMS Microbiol. Lett.*, 199(1):125–129, 2001.